Quantifying Mechanical Heterogeneity in 3D Biological Systems with the Atomic Force Microscope

by

Bryant Lee Doss

A Dissertation Presented in Partial Fulfillment
of the Requirements for the Degree
Doctor of Philosophy

Approved April 2015 by the
Graduate Supervisory Committee:

Dr. Robert Ros, Chair
Dr. Stuart Lindsay
Dr. Mehdi Nikkhah
Dr. Oliver Beckstein

ARIZONA STATE UNIVERSITY

May 2015

ABSTRACT

The atomic force microscope (AFM) is capable of directly probing the mechanics of samples with length scales from single molecules to tissues and force scales from pico to micronewtons. In particular, AFM is widely used as a tool to measure the elastic modulus of soft biological samples by collecting force-indentation relationships and fitting these to classic elastic contact models. However, the analysis of raw force-indentation data may be complicated by mechanical heterogeneity present in biological systems. An analytical model of an elastic indentation on a bonded two-layer sample was solved. This may be used to account for substrate effects and more generally address experimental design for samples with varying elasticity. This model was applied to two mechanobiology systems of interest. First, AFM was combined with confocal laser scanning fluorescence microscopy and finite element analysis to examine stiffness changes during the initial stages of invasion of MDA-MB-231 metastatic breast cells into bovine collagen I matrices. It was determined that the cells stiffen significantly as they invade, the amount of stiffening is correlated with the elastic modulus of the collagen gel, and inhibition of Rho-associated protein kinase reduces the elastic modulus of the invading cells. Second, the elastic modulus of cancer cell nuclei was investigated *ex situ* and *in situ*. It was observed that inhibition of histone deacetylation to facilitate chromatin decondenstation result in significantly more morphological and stiffness changes in cancerous cells compared to normal cells. The methods and results presented here offer novel strategies for approaching biological systems with AFM and demonstrate its applicability and necessity in studying cellular function in physiologically relevant environments.

Dedicated to my family and my fiancé Kathy,

for their unconditional support

and teaching me the value of hard work.

ACKNOWLEDGEMENTS

This dissertation would not be possible without the support received from colleagues, fellow students, and faculty at Arizona State University and beyond. I thank my advisor, Robert Ros, for mentoring me, allowing me to make mistakes, fostering my ideas, providing a rich graduate experience, and always keeping an open door. I thank my fellow labmates in the Ros lab, past and present – Olaf Schulz (who taught me how to work in the lab), Jack Rory Staunton (with whom I worked with closely for much of this dissertation), Patrick Bookjans, Ivan Yermolenko, Wayne Christensen, Charles Michael Gilbert (who was instrumental in establishing finite element analysis), Birgit Plochberger, Melanie Dannemeyer, Nethmi Ariyasinghe (who was instrumental in maintaining cell culture capabilities), Alex Ward, Sebastian Sandersius, Kiarash Rahmani Eliato, Nathan Banyai, Mark Linhart (who was instrumental in establishing mammalian cell culture), Nikita Satapathy.

I thank Keng-hui Lin for providing the opportunity to work closely with her in the lab at Academia Sinica, and the members of her lab (in particular, Li-fan Wu, Sriram Muthu Irulappan, Yi-hsuan Lee, Jau-Yi Wu) for their kind and generous assistance during a summer internship. Bulk rheometry data was collected in Keng-hui Lin's lab, JPK AFM data was collected in Chi Chen's lab (Academia Sinica).

I thank the Physical Sciences-Oncology Center at Arizona State University and Paul Davies for providing the opportunity to work in a very inclusive and interdisciplinary environment. I thank Stuart Lindsay, Tim Newman, and Otto Sankey for allowing me to work closely with and learn from them. I thank my graduate supervisory

committee – Robert Ros, Stuart Lindsay, Mehdi Nikkhah, and Oliver Beckstein – for their assistance and time commitment towards the preparation of this dissertation.

I graciously acknowledge funding support from the National Science Foundation East Asia-Pacific Summer Institute (IIA-14115018, PI: Bryant Doss, collaboration with Keng-hui Lin), Department of Education Graduate Assistance in Areas of National Need Fellowship (P200A090123, PI: Otto Sankey), National Cancer Institute Physical-Sciences Oncology Centers (U54CA143862, PI: Paul Davies), and Arizona State University.

Lastly, I acknowledge transparent and open-source contributions made to science. In particular, the MATLAB programs designed for the analysis of the raw data include contributions made to the MATLAB Central File Exchange by other users – IBWread.m for importing Igor Pro files (covered by the BSD license), and Fie.m for solving Fredholm Integral Equations of the Second Kind (cited in this dissertation).

TABLE OF CONTENTS

Page

CHAPTER Page

LIST OF TABLES

Table Page

LIST OF FIGURES

Figure Page

LIST OF ABBREVIATIONS

ADP ..... adenosine diphosphate

AFM ..... atomic force microscope

ATP ..... adenosine triphosphate

CLSM ..... confocal laser scanning microscope

DMEM ..... Dulbecco's Modified Eagle's Medium

DMSO ..... dimethyl sulfoxide

DNA ..... deoxyribonucleic acid

DMEM ..... Dulbecco's Modified Eagle's Medium

DoI ..... degree of invasion

DPBS ..... Dulbecco's Phosphate-Buffered Saline

ECM ..... extracellular matrix

EDTA ..... ethylenediaminetetraacetic acid

FBS ..... Fetal Bovine Serum

FEA ..... finite element analysis

GDP ..... guanosine diphosphate

GTP ..... guanosine triphosphate

HDAC ..... histone deacetylase

HBSS ..... Hank's Balanced Salt Solution

m.a.d. ..... median absolute deviation

MMP ..... matrix metalloproteinase

OLS ..... optical lever sensitivity

PA ..... polyacrylamide

PBS ..... phosphate-buffered saline

PDMS..... polydimethylsiloxane

ROCK ..... Rho-associated protein kinase

SEM ..... scanning electron microscope

s.e.m. ..... standard error (mean)

STM ..... scanning tunneling microscope

TS-A..... Trichostatin-A

a..... contact radius

E ..... Young's modulus

F ..... force

h..... sample height

k..... spring constant

R ..... probe radius

δ..... indentation depth

v..... Poisson's ratio

θ..... probe half-angle

1 INTRODUCTION

In studying classical physics, it is extremely common to reduce complex problems to a very simple analytical case. This presents a challenge for studying biological systems, which are heterogeneous by nature, contain intricate machinery, fall in a mesoscopic length scale which is too small for classical mechanics or ensemble averages, too large for quantum mechanics, and are not time-independent. Recent breakthrough discoveries such as the elasticity of the cell's environment affecting stem cell differentiation[1] and promoting the malignant phenotype of cancer cells[2] warrant a quantitative, physical sciences-based approach to emergent biological phenomena. Atomic force microscopy (AFM) has emerged as a critical technique in the quantitative study of cell mechanics, as the cells' response to external forces and deformations may be directly measured and correlated to biological processes. This dissertation is an extension of existing AFM methods for studying the mechanical properties of cells to include a first-order correction for biphasic mechanical heterogeneity and is used to measure elastic moduli of cells and nuclei embedded in some environment.

In §2, I introduce known key concepts in physical biology and mechanobiology which serve as motivation for the dissertation and provide background for some of the measurements performed in the lab. For example, the key components inside and outside of the cell which govern the mechanics, such as the cytoskeleton, extracellular matrix (ECM) and environment, nucleus, and how these contribute to key processes associated with cancer development. §3 discusses AFM and how it is used to collect microrheological data on soft matter, including the basic instrumentation, calibration, and

data analysis methods. Here, the AFM is also compared with other techniques commonly used to study cell mechanics under a variety of conditions.

As previously mentioned, mechanical heterogeneity is a challenging aspect of physical biology, and most existing models for interpreting raw AFM data do not account for this. §4 demonstrates a first principles solution to a bonded two-layer elastic indentation problem and how it may be applied to the analysis of AFM data and also the design of AFM experiments to minimize or maximize the effects of subsurface mechanical heterogeneities. The knowledge gained in §4 lead to the studies on biological systems of interest in §5 and §6.

§5 correlates AFM, confocal laser scanning microscopy (CLSM), and finite element analysis (FEA) to demonstrate how the mechanical properties of metastatic MDA-MB-231 breast carcinoma cells are altered when they are invading into a bovine collagen I matrix. The field standard is to use AFM to measure the mechanics of cells that are adhered to some 2D substrate such as glass, however this limitation is broken by the novel analytical tools developed in §4 and §5. The results presented here serve as a potentially key piece of information regarding the mechanisms for cancer cell invasion *in vivo*, and serve as a foundation for similar indentation-based rheometry studies of cells embedded in some complex environment.

§6 employs the qualitative model from §4 to study the mechanics of the cell nucleus *in situ*. As described in §2 and §5, the phenotype of the cell will vary depending on the substrate it is cultured in, the mechanical properties of the nucleus depend heavily on its environment as well, for example buffer conditions and physical anchoring, and thus should be studied in a physiologically relevant context to obtain meaningful results.

The nuclear elasticities of normal and cancerous cells are compared and the effects of pharmacological inhibitors to relax the structure of chromatin are measured with AFM and fluorescence microscopy.

2 PHYSICAL BIOLOGY AND CELL MECHANICS

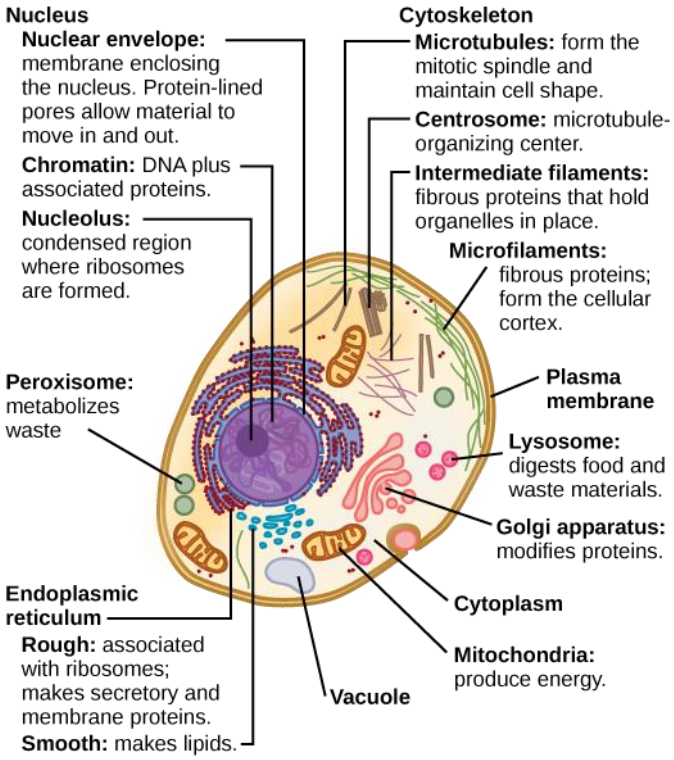

Figure 2-1: Eukaryotic cell. This image was obtained from *OpenStax College, Biology*[3] textbook and is licensed under Creative Commons 3.0.

The eukaryotic cell is the fundamental building block for animal life and is the link between understanding molecular machinery at the nanoscale and the emergent biological properties at the tissue scale. Cells have the capability to produce and expend energy, metabolize smaller organic molecules, produce their own proteins and small molecules to perform various functions, proliferate, and communicate with others to collectively form multicellular organisms. A simplified illustration of a eukaryote is shown in Figure 2-1, although not illustrated (and impossible to illustrate) are the countless number of smaller molecules that perform the required signaling within and

outside of the cell, expression of single genes, locomotion, replication of genes, synthesis of ATP, and other functions of the cell. This chapter will discuss the relevant biology needed to understand how cells resist and undergo stresses and strains, migrate on 2D surfaces and in 3D environments, sense and transduce mechanical cues from their environments, and how the mechanics of the cells is related to cancer metastasis.

Cytoskeleton

The dominant cellular component to resisting deformation and performing mechanical work is the cytoskeleton, of which there are three types: actin filaments, intermediate filaments, and microtubules. These are similar in several aspects: each are composed of smaller subunits which nucleate to form long polymer chains, they may dissemble and reassemble at very fast rates, and they provide physical stability for the cell[4].

Actin is localized throughout the cell, but the actin cortex is the prominent structure for cell migration and establishing cell shape as well as serving an integral role in forming adhesions, motility, exerting cellular traction forces, and receiving extracellular signals[4–6]. Filamentous f-actin is self-assembled in a cell by monomeric, globular g-actin subunits into a double-helical structure; both the atomic structures of g-actin momomers[7] and f-actin filaments[8] were discovered in 1990 using X-ray crystallography. The diameter of an actin filament is 6-8 nm and the Young's modulus is 1.3-2.5 GPa[9]. The filament formation process is highly dependent on ATP – (globular) g-actin with ATP is hydrolyzed into ADP shortly (but not immediately) after the g-actin subunit binds to an (filamentous) f-actin filament[10]. Actin filament formation is a

concentration-dependent nucleation process[4] and the critical concentration for actin polymerization is roughly ten times higher at the "pointed" end where actin (with monomers bound to ADP) is being depolymerized compared to the "barbed" end where the actin fiber is being elongated by more monomers of actin (bound to ATP)[6], providing the basic mechanism for cell "treadmilling" where a cell moves by simply depolymerizing actin at one and end polymerizing actin at the other.

Myosin II is a motor protein from the myosin superfamily which enables cells to generate force via binding to and pulling on actin filaments. The myosin II protein consists of a 150nm linear double strand of α-helices at the C-terminus (the "heavy chain") and two smaller unwrapped head groups at the N-terminus (the "light chain")[4]. Like actin, myosin can form thick filaments called myofibrils with many heads by additional wrapping of the heavy chain with other myosin molecules[4]. The myosin II light chain binds with the actin filament and contains a binding site for ATP. Once ATP is bound, myosin II will hydrolyze the ATP into ADP and produce a "power stroke" by which the myosin II head will bind to another region of the actin filament and release ADP, thus changing the relative position of the myosin II chain and actin filament and generating a contractile force[4]. This single-molecule process may be multiplied between large numbers of actin and myosin filaments into tissue-scale muscle contraction in structures called sarcomeres[4] or stress fibers in non-muscle cells, which is the focus of this work.

Actin is involved in many complex cellular processes, for example the initial polarization of the cell for directionality to exerting the final traction forces to propel motion, and there is a large (>100) amount of genes which regulate actin filament

assembly and disassembly and actin binding proteins to perform this (for example, see[4]). Actin filaments may be crosslinked together by various actin binding proteins. Some examples of this include the Arp2/3 complex which binds to the side of an existing actin filament and serves as a starting point for a new actin filament, thus creating a "branching" effect[5]. Two other examples (there are many more) are α-actinin and filamin, which bind to actin filaments on the sides on both ends thus crosslinking two strands (α-actinin for parallel strands, filamin for angled strands)[4,5]. The actin cytoskeleton and cortex play a role in cell elasticity – treating cells with drugs targeting actin filament formation and stability will result in decreased cellular stiffness[11,12].

Several actin binding proteins which connect the actin cytoskeleton with extracellular space through integrins and are thus heavily implicated in cell migration and adhesion have been reviewed by Le Clainche and Carlier[6]. Integrins are a family of heterodimer (consisting of various α and β subunits to bind different proteins) transmembrane proteins which link the intracellular cytoskeleton and extracellular matrix, and when they are clustered together produce so-called focal adhesion sites[4]. As integrins connect the cell with its extracellular space, it is widely used in a number signaling cascades. Vinculin and talin are two large proteins (116 kDa and 270 kDa, respectively) which connect the actin cytoskeleton with β-integrins (as well as bind with each other) and thus play a role in forming adhesions with a substrate. Vinculin has been identified as a key component for cell mechanosensing with both the extracellular matrix via integrins[13] as well as to other cells in cadherin complexes[14].

Microtubules are another cytoskeletal component that are analogous to actin in several ways: tubulin subunits are composed of heterodimers (α tubulin and β tubulin)

which polymerize to form microtubule filaments in a rate-limiting fashion, α tubulin contains GTP or GDP and is capable of hydrolysis affecting polymerization rates, there are plus and minus ends indicating the direction of polymerization, there are many microtubule associate proteins for crosslinking multiple strands and for facilitating assembly and disassembly, and microtubule structure adds mechanical stability to a cell[4]. The inner diameter of a microtubule is 14 nm, the outer diameter is 25 nm, and the Young's modulus is 1.9 GPa[9]. In mammalian cells, microtubules originate from the centrosome located near the nucleus and play key roles for subcellular organelle organization, intracellular trafficking, and formation of the mitotic spindle during cell division[4]. Of the cytoskeletal filaments, microtubules have the highest persistence length and thus have the highest stiffness[15], however they do not form crosslinked structures as actin filaments do. When microtubule structure is disrupted with drugs such as nocodazole, it has been demonstrated that the stiffness of cells will decrease[16].

Intermediate filaments are a class of cytoskeletal polymers which form bundles by twisting (more similar to myosin bundle formatting as opposed to actin or microtubules) and include nuclear lamins located inside the nuclear envelope, vimentin, keratins which contribute to cell mechanical strength, as well as many others[4].

Extracellular Matrices

Cells do not exist in a vacuum, and petri dishes and culture flasks do not exist *in vivo*. The extracellular matrix refers to the environment of the cell which contains a diverse cocktail of crosslinked proteins in a scaffold (or gel) as well as other secreted molecules which forms connective tissue *in vivo*. Extracellular matrices are produced and

aligned by fibroblasts (or chondroblasts for cartilage, and osteoblasts for bone). One family of ECM components are glycosaminoglycan molecules, which have long sugar chains and occupy a large amount of volume relative to the mass and are hydrophilic, thus producing a hydrogel like structure when they are covalently linked together into proteoglycan structures[4]. These proteoglycans interact with both the cell and molecules secreted into the ECM, thus are very important in cell signaling pathways[4]. Another prominent component is fibronectin, which is a large dimer glycoprotein which binds to integrins making it critical for cell adhesion, and also can crosslink to form fibrils which can produce tension-mediated adhesions with the cell (more binding sites are uncovered when the fibrils are stretched)[4].

Collagen is the most abundant protein family (and accounts for ~25% protein mass in humans) in the ECM and are composed of long, stiff triple-helical structure composed of three collagen α chains[4]. Collagen molecules are secreted by the cell and may crosslink and assemble into fibrils which have a diameter on the order of 10-100 nm, and these fibrils may assemble into fibers which have diameters on the order of 1 μm[4]. There are many types of collagen, some of which do not form fibrils, however the most abundant is collage I which is ~90% of collagen in humans and is fibril forming[4]. There is a high degree of interplay between the cell and collagen matrices (as discussed in the next section, and a simple illustration is given in Figure 2-2) as the cells may degrade, produce, and realign collagen and thus cell functions such as motility are mediated by the surrounding collagen matrix.

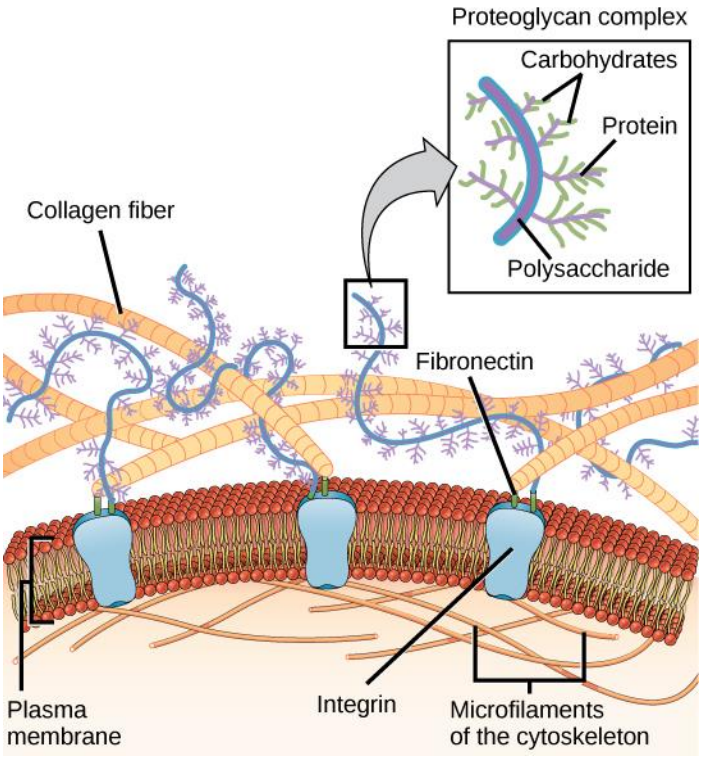

Figure 2-2: Cell-ECM junctions. This image was obtained from *OpenStax College, Biology*[3] textbook and is licensed under Creative Commons 3.0.

The mechanical properties of biological polymer gels such as ECM and cytoskeleton networks are currently an active area of research. On the single molecule level, the mechanics and elasticity are governed by polymer physics. Many bulk polymer gels (for example actin, collagen, fibrin, as well as others) have been shown to experimentally exhibit non-linear elasticity for large deformations such that their shear modulus begins to rapidly increase for high values of strain[17]. Several explanations for this phenomenon have been proposed, for example the strain stiffening is caused when the force regime switches from entropic (low strain) to enthalpic (high strain)[17], also randomly oriented polymer networks may transition from a bending-dominated response at low strain to a nonaffine stretching-dominated response at high strain[18]. These models

have been compared and reviewed by van der Giessen *et. al.*[19]. Biopolymer gels also behave differently from classical elastic materials in that they exhibit a "negative normal stress" when undergoing parallel shear, meaning as a deformation is applied in one direction, there will be a surface stress pulling the gel closer together[20]. Brown *et. al.* demonstrate that fibrin exhibits similar properties from length scales ranging from single molecules to tissues and propose that the cause is a combination of the protein unfolding regime (as opposed to the thermal fluctuation small strain regime) and a loss of water in the gel due to the new accessibility of hydrophobic protein domains as determined by examining the volume changes during strain[21]. Collagen and fibrin matrices may also undergo plastic deformations under large amount of strains whereby the length of fibrils in the matrix are permanently extended, thus delaying the onset of strain-stiffening to higher values of strain when the fibrils begin to stretch[22]. At the tissue scale (consisting of many cells and ECM at different densities), there are large deviations in the measured elastic moduli spanning 10^1-10^5 Pa for human fat tissue to spinal cord tissue, respectively[23].

Reconstituted collagen I gels are often used as a model system to investigate cell motility in 3D and the stiffness is tunable by adjusting protein concentration. Collagen I gels form a scaffold-like structure of fibrils with pore size negatively correlating with the relative concentration of collagen I protein in the gelling solution[24]. The properties of the gels depend on the species origin of the collagen – bovine collagen I forms more fibrils with a diameter of approximately 60 nm, whereas rat tail collagen I form fibrils with a diameter of about 20 nm[24]. Therefore, when the same weight concentration of collagen is used, the rat tail collagen I gels will have a larger number of more crosslinked fibrils and

is stiffer than bovine collagen I gels at the same concentration[24]. Additionally, the temperature at which the collagen gels form fibrils have an influence – rat tail collagen I gels at higher temperatures (up to 37°C) contain thinner, more sparse and crosslinked fibrils compared to gels formed at lower temperatures (down to 4°C) where the fibril numbers are fewer but thicker[24]. Another model system that is widely used to examine cell behavior is Matrigel, which is essentially a basement membrane explant (containing mostly laminin, collagen IV, as wells as additional proteases, growth factors, and other proteins) on which cells grow into structures that resemble the structures in which they grow *in vivo*[25]. Matrigel has been shown to have an elastic modulus between 0.1-0.5 kPa[26,27].

Cell behavior on substrates with elasticity on the same magnitude as *in vivo* may be studied on materials other than reconstituted ECM. Polyacrylamide (PA) gels are frequently used as an inexpensive, tunable elastic substrate on which ECM proteins may be bound such that cells may naturally adhere to the soft gel[28]. Monodisperse foam gels of gelatin or PA with spherical pores may be produced by a microfluidic device to engineer a periodic, structured cell growth substrate with the added benefit of 3D dimensionality[29,30]. There are also many other schemes to produce substrates for cell mechanobiology studies using microfabricated topographies (for example by silicon etching, soft lithography, etc) and these have been recently reviewed[31].

Mechanobiology

Mechanobiology is a relatively new subfield at the interface of biology and physical sciences. From a fundamental physics standpoint, there are limited ways in

which cells may communicate information, for example via diffusion, electrical signals, or mechanical signals, which is the primary focus of this field and this dissertation. One physical concept related to this is tensegrity, which considers the cell's cytoskeleton a collection of mechanical elements (springs, supports) that transmit information immediately when a force or deformation is applied to the cell surface or an interior element (for example, via an integrin or cadherin molecule which is bound to the cytoskeleton), thus activating a cascade of biochemical reactions.[32]

Transmembrane integrin proteins and focal adhesions play a heavy role in communication between the cell and its environment. For example, focal adhesion kinase is a widely studied protein that exists at focal adhesion sites (binding with talin and paxillin, which in turn bind to the integrins) and can relay signals to other proteins by phosphorylating (or activating) them[4]. One family of proteins which can be activated at focal adhesion sites is the Rho GTPase family (GTPase proteins are typically referred to as inactive when bound to GDP and active when bound to GTP and able to transfer a phosphate group, thus can act as switches), which has been linked to cell division, morphology, polarity, motility, adhesion, and gene expression[4,33,34]. Members of this family include (but are not limited to) Rho, Rac, and Cdc42 (as well as numerous isoforms, for example RhoA), and these have been strongly implicated in actin regulation in the cell; for example, Rac may induce actin polymerization and lamellipodia formation, Cdc42 can provide directionality for cell migration, and Rho can control assembly and contraction of actomyosin[34] and recruits actin and integrins to an adhesion site[4]. RhoA activates ROCK, which in turn can lead to stress fiber contraction via myosin light chain phosphorylation[33].

The mechanisms allowing cell motility on rigid 2D surfaces (e.g. a petri dish) has been thoroughly studied in the past century. Cells may form either lamellipodia (sheet-like protrusions) or filopodia (spike-like protrusions) in the direction of migration by assembling actin filament networks and are connected to the substrate[4,5]. This allows the cells to generate traction on the new adhesion for forward motion as it depolymerizes the cytoskeleton at the trailing edge[4,5], known as treadmilling. Myosin plays a large role in allowing cells to generate traction forces in the leading edge, as well as applying a contractional force in the rear of the cell to help generate forward motion[4].

The mechanisms for cell motility in a physiological 3D environment contain a higher amount of complexity compared to migration in 2D, and while the process is similar in some ways, the cells must behave differently as there is no rigid surface on which to generate traction forces and there is an extracellular matrix that requires navigating through.

For single cell motility in 3D, there are two modes of motility that have been proposed in literature: mesenchymal motility, where the cell is elongated, and amoeboidal motility, where the cell adopts a more rounded shape (these are also sometimes referred to as lamellipodial and lobopodial motility, respectively). Friedl and Wolf have reviewed the physical characteristics of cancer cells undergoing both modes of motility[35,36]. Mesenchymal motility is similar to the mechanism for 2D migration above – the cells form strong adhesions with the ECM and can generate traction forces for forward motion while remodeling the ECM either by contractile forces or proteolytic digestion of the ECM with matrix metalloproteinases (MMP)[35]. Amoebodial motility occurs when the cells cannot form tight adhesions with the ECM and are thus unable to

generate tractional forces for forward motion, therefore the cells rely on actomyosin contraction for propulsion through the ECM either by exerting large forces to remodel the ECM for migration or exerting large forces on the cell body to deform to "squeeze" through ECM[35]. Intracellular pressure is significantly higher in cells undergoing lobopodial motility than lammelipodial motility and is significantly higher in the anterior (front) direction of motility compared with the posterior (rear)[37]. This observed intracellular pressure gradient is nullified when cells are treated with inhibitors targeting myosin contractility[37].

Rho and Rac GTPases have been shown to play a crucial role in the differentiation of mesenchymal versus amoeboidal mode for motility in 3D. Yamazaki *et. al.* demonstrated that knocking down Rac1 in HT1080 fibrosarcoma cells results in more of the cell population undergoing Rho/ROCK based amoebodial mode and fewer focal adhesions in 2D, whereas knocking down RhoA results in a larger population in mesenchymal mode[38]. Yamada *et. al.* observed similar results for cells in lamellipodial (polarized Rac) versus lobopodial (non-polarized Rac, high RhoA) migration in 3D and suggest the cells will switch between the modes depending on the elastic behavior of the ECM[39].

The elasticity of the biological microenvironment plays a crucial role in cell mechanics. Janmey *et. al.* demonstrated that the spreading area, Young's modulus as measured with AFM, and amount of total f-actin sedimentation will increase with the stiffness of fibronectin-coated PA surfaces with a substrate saturation value of approximately 20 kPa[40]. It should be noted that the fibroblasts are very thin (maximum height ~1.5 μm, protrusion heights on the order of 100 nm) and sharp AFM probes were

used in this study with maximum indentation depth of 400 nm[40], therefore the measurements were most likely most sensitive to the cell cytoskeleton at relatively small distances from the basal surface. When MDCK cells and fibroblasts are seeded on fibronectin coated PDMS micropillar arrays with varying spring constants, the cell projected area and total traction force exerted by the cells will scale linearly with the pillar spring constant until a saturation value of ~150 nN/μm is achieved (equivalent Young's modulus of ~90 kPa)[41]. Additionally, when PDMS pillars with anisotropic stiffness are used, cells will prefer to align along the axis of higher stiffness whereas cells will have a more random orientation on an isotropic surface[41,42].

Higher levels of cellular function (i.e. gene expression and regulation) may be dramatically altered by simply varying the elasticity of the microenvironment. In a seminal work, Engler *et. al.* demonstrated that mesenchymal stem cells differentiate differently when seeded onto PA gels of varying stiffness and myosin II inhibition removed the dependence of the microenvironment stiffness on the stem cell fate[1]. Recently Swift *et. al.* demonstrated that lamin A, an intermediate filament inside the nuclear envelope which stabilizes the nucleus and controls gene expression, of mesenchymal stem cells is expressed higher when on surfaces with higher elastic modulus and that stem cell fate may be altered by adjusting lamin A levels, indicating that mechanotransduction from ECM stiffness is part of a complicated gene regulatory network involving the mechanical coupling between the microenvironment and lamin-A[43] (for example, via myosin II). It has been demonstrated that stem cell differentiation via substrate elasticity is also regulated by vinculin, a mechanosensing protein localized at adhesion sites, via knock-down experiments[44]. It has been recently

proposed that the porosity of the substrate may contribute to the phenotype of stem cells as transmembrane proteins will tether and transmit signals differently[45], however more recent studies examining this shows that protein tethering may have no contribution[46]. Cell shape has also been demonstrated to have a large role in the differentiation of mesenchymal stem cells – cells that are grown on micropatterened surfaces will differentiate differently depending on the aspect ratio of the pattern, and the effects of the surface patterns may be altered by using drugs that affect actomyosin activity, microtubule stability, and $\alpha_5\beta_1$ integrin blockers[47].

Nuclear Mechanics

The nucleus is the most prominent eukaryotic organelle and the location of DNA and transcription. The nucleus contains a membrane or envelope which is a double phospholipid bilayer with pores allowing for transport, its own cytoskeleton along the nuclear wall composed of intermediate filaments lamin A/B/C (similar to how cells have an actin cortex), and transmembrane proteins such as nesprin which couple the nuclear lamin with the exonuclear cytoskeleton (similar to how integrins connect the cell cytoskeleton to the extracellular matrix)[48]. Each cell contains about two meters of linear DNA which needs to be compressed by histones and DNA binding proteins across several magnitudes in length, first in nucleosomes consisting of several base pairs, then chromatin which are fibers of DNA containing millions of base pairs and interact with distant regions of the genome and also nuclear lamins, and finally into chromosomes containing on the order of one hundred million base pairs[48]. Chromatin structure is fibrous much like the cytoskeleton, and the structure and packing density of the

chromatin alters gene expression – heterochromatin refers to more dense regions of chromatin where transcription does not occur, while euchromatin refers to regions where the DNA is more accessible and transcription occurs[48].

The mechanical properties of extracted nuclei have been closely examined in recent years. Current literature suggests that nuclear mechanics is governed by an interplay of lamins and chromatin. Lamins A/C have been previously shown to contribute positively to the elastic stiffness of nuclei[49,50]. Mutations in lamin A/C has been linked to a large number of diseases, and mutations in some of the genes involved in nuclear mechanotransduction have also been linked to disease[51]. Discher *et. al.* demonstrated that human mesenchymal stem cells which are lamin A/C deficient are much more deformable than fibroblast nuclei and becomes less deformable as the stem cells begin to differentiate[52]. In addition, nuclei are shown to be less deformable when the chromatin structure is condensed and long deformations to nuclei show irreversible disruption in chromatin architecture[52]. The authors conclude that lamin A/C contributes largely to the elastic properties of the nucleus and non-condensed chromatin the viscous component and that chromatin plasticity of the nucleus in non-differentiated stem cells is key for the cell to form their final phenotype. Heterogeneous, or condensed chromatin has been shown to positively correlated with nuclear stiffness and negatively correlated with nuclear diffusion rates when studied with a marker for cellular pluripotency, and the nuclear stiffness is reduced cells are stripped of divalent cations or treated with a histone deacetylase inhibitor[53]. Decondensation of the heterochromatin[54] and the presence of divalent cations will affect the size of extracted nuclei, also affecting the stiffness of extracted nuclei[55]. It has also been recently shown that actin stress fibers will regulate the

size and shape of the nucleus, as well as location of heterochromatin[56], and that embryonic stem cells display negative Poisson's ratios during certain transitional stages where the heterochromatin is decondensed[57].

Nuclear stiffness is also an important feature for cell motility in 3D. The nucleus is reported to be the stiffest organelle present inside of the cell[52,58], therefore either ample space is needed for the nucleus to move throughout an ECM scaffold (the pore size must be large enough), or the nucleus must undergo high deformation in order to move throughout the scaffold. Wolf *et. al.* demonstrate a physical relation between 3D motility arrest as a function of nuclear size, collagen I matrix pore size (but not stiffness), and presence of an MMP inhibitor and identify maximum nuclear deformation relative to the ECM pore size as a limiting factor[24]. It was also shown that cell mechanotransduction pathways involving ROCK and integrins play a key role in nuclear movement during cell migration in 3D to propel the cells forward and that cells expressing lamin A/C require MMP activity to degrade the matrix, whereas lamin A/C deficient cells do not require MMP activity[24]. During lobopodial migration where nuclear deformation is observed, the nucleus may also serve to compartmentalize the cell into low pressure (posterior) and high pressure (anterior) regimes in a nesprin-3 dependent manner such that the nucleus acts as a piston for maintaining the pressure gradient in a moving cell[37].

Cancer Mechanobiology

As cell mechanics plays the prominent role in motility, some anatomical fields where mechanobiology must be strongly considered include embryogenesis, wound healing, and cancer. One of the original six "hallmarks" of cancer as dubbed by Hanahan

and Weinberg in 2000 is metastasis, the process by which cells disseminate from the primary tumor, invade into the surrounding tissue, and form secondary tumors at distant locations in the body[59] (the total amount of hallmarks was revised later in 2011 to ten[60]). However, this is not the only hallmark in which exclusively the mechanical properties of cells play a role in – mechanotransduction induced changes in the stiffness of the nuclear envelope (via lamin A) may lead to genomic instability and enhanced mutation rates[43]. The physical process of metastasis has been recently reviewed by Wirtz *et. al.*[61] and includes the epithelial-to-mesenchymal transition from the primary tumor, tissue invasion and intravasation into the vasculature system, adhesion to blood vessel wall and extravasation out of the vasculature, and finally growth of a secondary tumor.

Focal adhesion kinase has been shown to be upregulated in some cancers and its downstream effects include the epithelial-to-mesenchymal transition, as well as Rho GTPase signaling and invasion[62]. The tumor microenvironment is stiffer than healthy tissue (~4.0 kPa compared to ~0.2 kPa for tumour and normal mammary tissue, respectively), in a seminal paper Weaver *et. al.* linked this increase in stiffness to a cell's progression to a malignant phenotype by enhanced extracellular signal-regulated kinases, ROCK activity, certain focal adhesion kinase phosphorylation, and vinculin[2]. Mesenchymal epithelial cells were shown to form normal luminal structures on soft (~0.2 kPa) substrates, however on stiffer substrates would exhibit malignant and mesenchymal features[2]. It has also been demonstrated that cancer cells will stiffen their microenvironment (for example, via lysyl oxidase) to enhance integrin signaling and induce the progression into a malignant phenotype *in vivo* (inhibition of lysyl oxidase results in less malignant tumors)[63]. This presents a conundrum in that metastasis and

malignancy in cells is promoted by stiffer extracellular matrices, however cell motility is often inhibited when the matrix crosslinking density is too high (for example, Wolf *et. al.*[24]).

In addition to lysyl oxidase inhibition, cancerous cells may be reverted to a normal phenotype by functionally blocking β_1 integrins[64] and epidermal growth factor receptor[65], thus altering the chemical and mechanical signaling pathways associated with the extracellular environment. When these are blocked and the phenotype is reversed, cancer cells undergo similar coherent angular motion patterns required to form luminal structures in 3D (additionally, E-cadherin inhibition results in loss of normal motion patterns for luminal formation)[66].

3 ATOMIC FORCE MICROSCOPY FOR SOFT MATTER MICRORHEOLOGY

Scanning probe microscopy with atomic resolution was first developed in the early 1980s by Binnig *et. al.* with the development of the scanning tunneling microscope (STM)[67], a machine capable of producing topographic images with atomic resolution by employing knowledge of a controlled tunneling current in vacuum and accurate piezoelectrics for positioning. Gerd Binnig and Heinrich Rohrer were awarded half of the Nobel Prize in Physics in 1986 for the development of the STM. The atomic force microscope was first proposed along with a prototype demonstration by Binnig *et. al.* in 1986[68]. The purpose of the original AFM was to provide high resolution topographical of insulator samples, as the already existing STM was only capable of imaging conductive surfaces. Since then, the AFM has undergone several instrumental improvements, such as the addition of an optical lever to detect cantilever deflection distances[69] (the original AFM used an STM probe to detect cantilever deflections). In 1992, Tao *et. al.* used the AFM as a nanoindenter to determine the elastic properties of cow tibia, the first biological sample, and observed stiffness variations at high resolution[70].

The AFM is capable of performing indentation-based rheology across many different time (ms-s), length (nm-μm), and force scales (pN-μN). In order to extract material properties of the sample, some the force-indentation data from the AFM must be fit to some contact model. There are many different strategies for fitting AFM force-indentation data depending on assumptions made regarding the sample. This chapter will provide the relevant background for collecting and analyzing raw AFM data

to extract quantitative mechanical properties, including calibration and elastic contact theory, and will also discuss how the AFM compared with similar experimental microrheology techniques often used in cell mechanics, and also simulations. In this dissertation, the Asylum MFP-3D is used for the vast majority of measurements, therefore description of the theory will be biased towards that specific instrument.

Instrumentation

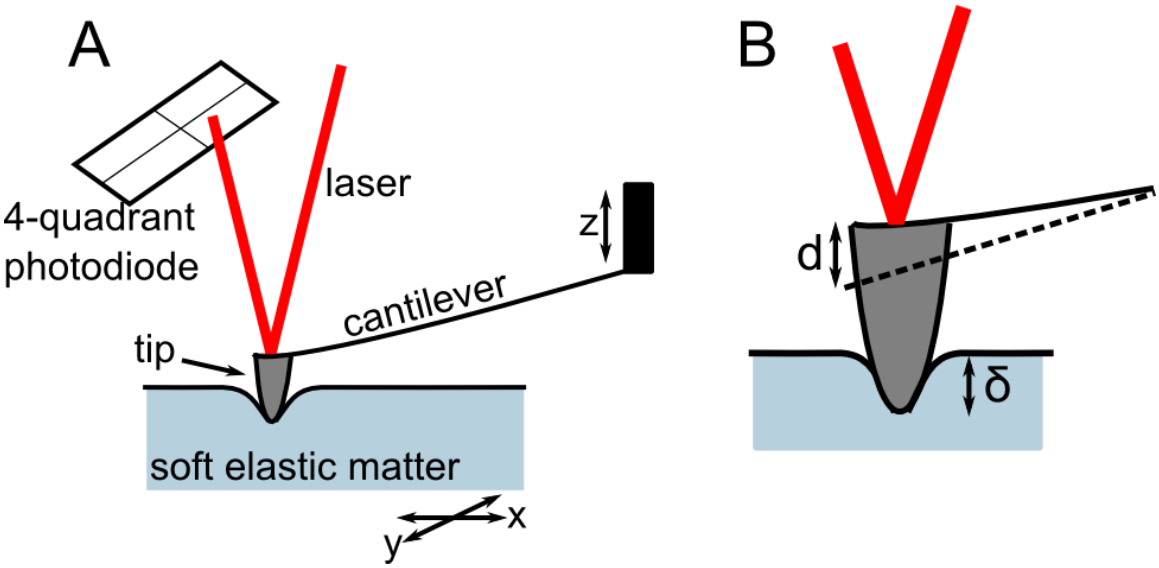

Figure 3-1: Schematic of AFM instrumentation. (A) Zoom out, showing the photodiode for detecting deflection signals and the full cantilever which is moved in the z-direction at the base. (B) Zoom in, showing the magnitude of deflection and indentation as detected by the optical lever.

Figure 3-1 shows a basic schematic of the AFM instrumentation. For indentations into soft matter, it is assumed that the tip is much stiffer than the sample and therefore all deformations are constrained to the sample. The indentation depth, δ, is given by

$$\delta = z - d \tag{3-1}$$

where *z* is the relative distance of the cantilever base reported by the piezoelectric and d is the cantilever deflection distance

$$d = S_{OL}\Delta V \tag{3-2}$$

With S_{OL} being the inverse optical lever sensitivity (OLS) and ΔV being the change in voltage as reported by the photodiode. The force experienced by the cantilever *F* is given by

$$F = kd \tag{3-3}$$

where *k* is the spring constant of the cantilever. Calibration of the OLS and spring constant is further discussed below.

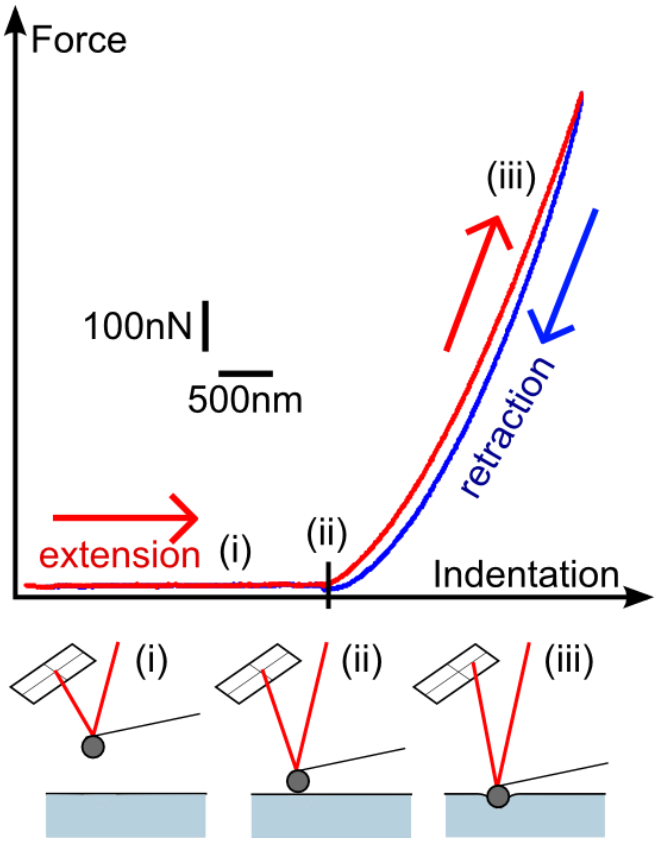

Figure 3-2: Schematic of an AFM force-indentation curve on a PDMS gel. The base:crosslinker ratio is 45:1, resulting in a gel that is approximately 60 kPa and the tip has a sphere glued on with diameter ~10µm. The PDMS was plasma cleaned to make the surface hydrophilic and the measurement was performed in buffer to minimize adhesion. (i) non-contact region, (ii) contact point, (iii) contact region. Red is the extension (loading) curve, moving from left to right, and blue is the retraction (unloading) curve, moving from right to left. The black line in (ii) represents the contact point.

Figure 3-2 demonstrates an example force-indentation curve generated by AFM. The cantilever is lowered to the sample using piezoelectrics in the AFM head in an open-loop or closed-loop mode. In the case of the Asylum MFP-3D, there is a capacitive sensor inside the AFM head that reports the z-position of the cantilever. In closed-loop mode, there are feedback electronics which will adjust the piezo speed using the capacitive sensors, however in open-loop mode the speed is not adjusted using electronic feedback, resulting in potentially faster but less accurate speeds. When the probe comes

into contact with the sample, the cantilever will begin to bend and the deflection signal will increase as the laser position on the photodiode moves. When the probe is moved away from the sample, the deflection signal will drop back to the baseline level. If there is adhesion between the tip and the sample, the deflection signal may dip below the baseline level on both the extension and retraction segments of the curve. In an ideally elastic sample, the extension and retraction curves will perfectly overlay, however if there is some plastic deformation, creep, or viscoelastic contribution from the sample, then the segments will not overlay.

Calibration

As mentioned previously, the raw data which the AFM collects is a voltage from the photodiode and this voltage must be translated into a usable quantity, such as force. In order to collect accurate force data from the AFM, it is imperative that the cantilever spring constant *k* assumed in the experiment is as close to the actual value as possible, and the OLS is well calibrated such that the actual deflection of the cantilever is properly calculated.

The simplest method for calibration the OLS is to indent a rigid surface to receive a z-piezo versus photodiode voltage curve, assume $\Delta z = \Delta d$, and then calculate the inverse OLS as the cantilever bending distance divided by the photodiode voltage. This procedure is highly dependent on the intensity of the laser and positioning on the cantilever, thus must be recalculated each time the laser moves or the media of cantilever changes (such as moving from air to liquid due to the refractive index change).

Determining the spring constant of a cantilever mounted in the AFM is not a trivial process and is a currently active area of research. The most widely used method for spring constant calibration is the thermal tuning method[71]. The cantilever is assumed to be a 1D simple harmonic oscillator under weak thermal fluctuations and under the equipartition theorem, the vibrational energy of each degree of freedom is given by[71]:

$$\frac{1}{2}k_B T = \frac{1}{2}k\langle q^2 \rangle \tag{3-4}$$

where k_B is the Boltzmann constant, T is the temperature, k is the cantilever spring constant, and q is the oscillator displacement. In practice, the mean square oscillator displacement $\langle q^2 \rangle$ is determined by performing a frequency sweep and calculating the integral of the power spectrum of the first vibrational mode in the frequency domain[71]. The cantilever displacement is related to the voltage from the photodiode by

$$\langle q^2 \rangle = \langle V^2 \rangle {S_{OL}}^2 \chi^2 \tag{3-5}$$

Where S_{OL} is the inverse OLS (units of distance divided by voltage) and χ is the "kappa factor" (despite having a different symbol) which compensates for dynamic oscillations versus static bending and the positioning of the laser on the cantilever and is further discussed later in this section. The power spectrum is fit to a Lorentzian[72]

$$P(f) = B + \frac{A_1 f_1}{\left(f^2 - {f_1}^2\right)^2 + \left(\frac{f f_1}{Q_1}\right)^2} \tag{3-6}$$

to compute the background amplitude B, first mode amplitude peak A_1 in units of voltage, resonance frequency f_1, and quality factor Q_1 (related to the width of the resonance), thus the area is

$$\langle V^2 \rangle = \int_0^\infty P(f)df = \frac{\pi A_1 f_1 Q_1}{2} \tag{3-7}$$

As alluded to previously, there must be some correction factors included into the calculation. Butt and Jaschke discussed discrepancies in using the OLS as computed in the supported regime (cantilever in contact with a hard surface as in standard OLS calibration) versus the freely oscillating regime (cantilever is not in contact with a surface as in a thermal noise calculation) and calculated correction factors for the oscillation amplitude of freely oscillating cantilevers versus supported cantilevers for each vibrational mode[73]. In the case of the Asylum MFP-3D, the optical lever for detecting cantilever deflection uses a very relatively large light source (as opposed to a focused laser beam), thus some errors need to be considered when the light spot size has similar length scale to the cantilever. Walters *et. al.* introduced a scaling term to the inverse OLS of 1.09 to account for this in the calibration of short cantilevers using the first vibrational mode[74]. Proksch *et. al.* formalized the definition of the kappa factor χ as the ratio of the sensitivities of the freely oscillating cantilever and supported cantilever and calculated the values of χ for different rectangular cantilever lengths and spot sizes[75]. When χ=1.09 (the case of an infinitely small spot size at the end of a long cantilever), the effective correction factor (0.842) is very similar to that given by Butt and Jaschke[73] (0.817) for the first vibrational mode of rectangular cantilevers. χ will decrease as the cantilever becomes shorter relative to the size of the laser spot and will increase as the laser spot is moved off the end of the cantilever and is typically greater than 1.00 for common cantilever and laser dimensions[75].

Thus, the final form of the spring constant from the thermal noise method is given by

$$k = \frac{2k_B T}{\pi A_1 f_1 Q_1 {S_{OL}}^2 \chi^2} \tag{3-8}$$

Other comparable methods for the calibration of rectangular cantilevers are the Sader method[76] which relies on knowledge of the cantilever dimensions, resonance frequency, and quality factor, and the Cleveland method[77] which relies on adding a mass to the end of the cantilever and observing changes in resonance. The thermal noise method gives very similar (within 10%) results to the Sader and Cleveland method for rectangular cantilevers[72,75]. For the calibration of triangular cantilevers, different correction factors are required[78]. A 15% systematic error in spring constant calibration using the thermal method has been recently obtained across multiple instruments[79] and is generally regarded as the normal error in spring constant determination.

Analyzing Force-Indentation Data

Once the AFM force-indentation data is collected, one common analysis technique is to fit the curve with some kind of model to determine mechanical properties of the sample. The simplest parameter to determine is the Young's modulus *E*, which is a single parameter describing the elasticity, or resistance to deformation, of the sample. This also requires some prior knowledge of the compressibility of the sample, or the Poisson ratio *v*. Sneddon presents a simple method for determining the force-indentation response for a generic indenter described by some function *f*(*r*), and also presented solutions for some common indenter shapes[80].

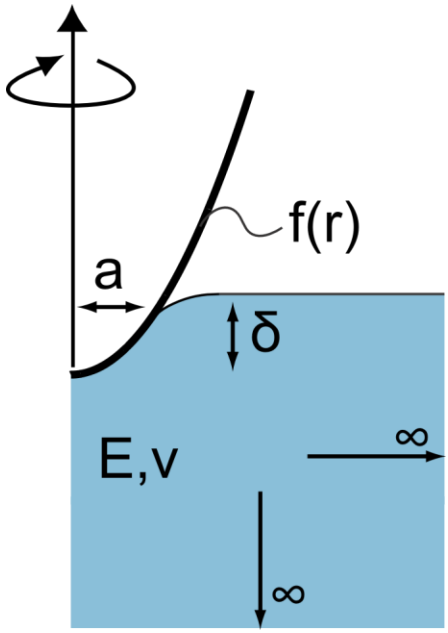

Figure 3-3: Axisymmetric elastic indentation problem.

The force-indentation response on an elastic material has the form

$$F(\delta) = \frac{E}{(1-\upsilon^2)}\lambda(\delta) \tag{3-9}$$

Where F is the force, δ is the indentation depth, and λ is some function describing the shape of the indenter and has the units of distance squared in this context. For parabolic (Hertz) and conical (Sneddon) indenters, λ is a power-law function with base δ and exponents 3/2 and 2, respectively[81]. For each tip shape $f(r)$, the function $\lambda(\delta)$ may be derived, as well as the relationship between δ and a, the contact radius between the probe and the sample using Sneddon's procedure in Appendix 1. The various quantities are displayed in Figure 3-3.

Some tip shapes that are commonly used to analyze AFM force-indentation data are a parabolic tip shape (Hertz model), conical tip shape (Sneddon model), hyperbolic

tip shape, and a blunted cone. For a parabolic indenter, Sneddon's procedure provides the same result as the Hertz model[80,82]:

$$f_H(r) = \frac{r^2}{2R} \tag{3-10}$$

$$a_H = \sqrt{R\delta} \tag{3-11}$$

$$\lambda_H = \frac{4}{3}\sqrt{R\delta^3} \tag{3-12}$$

Thus, the Hertz model is

$$F_H = \frac{4}{3}\frac{E}{(1-\upsilon^2)}\sqrt{R\delta^3} \tag{3-13}$$

For a conical indenter, the solution provides the same result as the Sneddon model[80]:

$$f_S(r) = r\cot\theta \tag{3-14}$$

$$\delta = \frac{1}{2}a_S\pi\cot\theta \tag{3-15}$$

$$\lambda_S = \frac{2\delta^2}{\pi\cot\theta} \tag{3-16}$$

Thus, the Sneddon model is

$$F_S = \frac{2\delta^2}{\pi\cot\theta}\frac{E}{(1-\upsilon^2)} \tag{3-17}$$

For a hyperbolic indenter, the solution is as follows[83,84]:

$$b_{Hy} = R\cot\theta \tag{3-18}$$

$$f_{Hy}(r) = b_{Hy}\cot\theta\left[\sqrt{\frac{r^2}{{b_{Hy}}^2}+1}-1\right] \tag{3-19}$$

$$\delta = \frac{a_{Hy}\cot\theta}{2}\left[\frac{\pi}{2}+\tan^{-1}\left(\frac{a_{Hy}}{2b_{Hy}}-\frac{b_{Hy}}{2a_{Hy}}\right)\right] \tag{3-20}$$

$$\lambda_{Hy} = \frac{{a_{Hy}}^3}{R}\left\{\left(\frac{b_{Hy}}{a_{Hy}}\right)^2 + \frac{b_{Hy}}{2a_{Hy}}\left[1 - \left(\frac{b_{Hy}}{a_{Hy}}\right)^2\right]\left[\frac{\pi}{2} + \tan^{-1}\left(\frac{a_{Hy}}{2b_{Hy}} - \frac{b_{Hy}}{2a_{Hy}}\right)\right]\right\} \quad (3\text{-}21)$$

For a blunted cone, Briscoe[85] derived a model for a tip shape which is parabolic at the end and transitions to a cone at a specific distance, the model is given by:

$$b_B = R\cos\theta \quad (3\text{-}22)$$

$$f_B(r < b_B) = \frac{r^2}{2R}$$

$$f_B(r \geq b_B) = (r - b_B)\cot\theta + \frac{{b_B}^2}{2R} \quad (3\text{-}23)$$

$$\delta = \frac{a_B}{\tan\theta}\left[\frac{\pi}{2} - \sin^{-1}\left(\frac{b_B}{a_B}\right)\right] \quad (3\text{-}24)$$

$$\lambda_B = \frac{2}{\tan\theta}\left\{\delta a_B \tan\theta - \frac{{a_B}^2}{2}\left[\frac{\pi}{2} - \sin^{-1}\left(\frac{b_B}{a_B}\right)\right] + \frac{b_B}{2}\sqrt{{a_B}^2 - {b_B}^2}\right\} \quad (3\text{-}25)$$

For the blunted cone and hyperbolic models, the result is not a convenient closed-form equation. Fitting force-indentation curves to these models requires some numeric tools to first determine the indentation depth and contact radii, and then they may be fit to the curves. For a tip which is spherical at the end and transitions to a cone at the point at which the first derivative is smooth (sphero-conical tip), the model is derived in Appendix 1.

There are several different strategies for determing the contact point and fitting the force-indentation curves, as reviewed by Lin and Horkay[81] depending on whether there is *a priori* knowledge of the contact point or if the contact point should be a parameter of the fitting algorithm. The location of the contact point plays a heavy role in

the subsequent elasticity analysis as demonstrated by Crick and Yin where apparent Young's moduli differed significantly with 100 nm errors of the contact point determination[86]. Lin and Horkay classify contact point algorithms depending on whether or not the point (δ=0, F=0) need to lie in the raw dataset as fully constrained for both points, semi-constrained for one variable, or unconstrained for neither[81]. Manually determining the contact point is often very difficult due to various additional long and short-range interaction adhesive or repulsive forces, but is also difficult because the amount of force required for small indentations of soft matter may be on the same order of magnitude of the noise threshold in AFM indentations. Many automated methods exist for contact point determination, but most have some form of limitation depending on the type of data (for example non-linear, adhesive, high noise, etc.)[81].

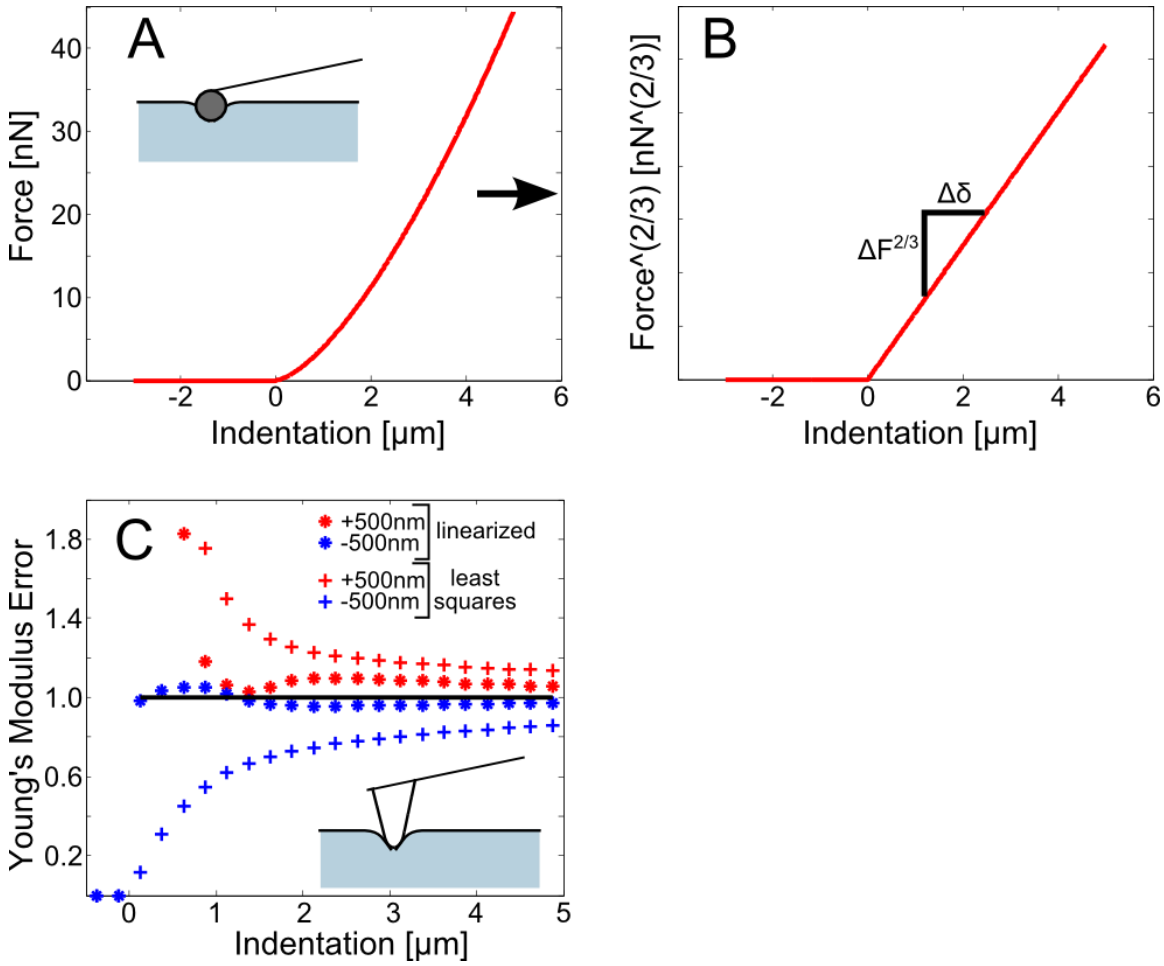

Figure 3-4: Demonstration of the linearized fit method. (A) Simulated force-indentation curve of a sphere indenting into a soft elastic material, following exactly the Hertz model. (B) force$^{2/3}$-indentation curve showing a linear slope, which is directly computed into a Young's modulus for a Hertzian indenter, there is identically no error in the computed Young's modulus if the zero force is correctly identified. (C) Error in the Young's modulus of a sphero-conical indenter if the contact point is chosen incorrectly, stars represent fits from the linearized method and plus signs represent a least squares method. Errors are induced when the contact point (F=0, δ=0) is not chosen properly, but are minimized with the linearized fit method.

Guo and Akhremitchev introduce a method to reduce errors from contact point uncertainty by first linearizing the data and performing a regression for the slope of the force as a function of indentation (in other words, focus only on the relative change of force with respect to indention as opposed to absolute values) as a way to minimize errors

from contact point determination[87]. This method of regression has also been applied to AFM studies on the elasticity of mammalian cells by Ros *et. al.* in a piecewise fashion[88] and by Engler *et. al.* to analyze force-indentation curves of layered PDMS and *Drosophila* myocardial layers[89]. Figure 3-4A and Figure 3-4 B show a simulated Hertzian force-indentation curve and the subsequent linearized curve used to find the Young's modulus. The piecewise depth-dependent linearized regression method may be implemented by considering changes in the force with respect to indentation depth:

$$\Delta F(\delta) = \frac{E}{(1-\nu^2)}\Delta\lambda(\delta) \tag{3-26}$$

λ is a exactly a power law function for parabolic (Hertzian) and conical (Sneddon) indenters and may otherwise be approximated as a power law function for small piecewise segments of the data, thus

$$\Delta\lambda(\delta) \rightarrow A\Delta\delta^B \tag{3-27}$$

Once the exponent in the power law is known, the force may be linearized by

$$\Delta F^{1/B}(\delta) = \left[\frac{EA}{(1-\nu^2)}\right]^{1/B}\Delta\delta \tag{3-28}$$

The slope of F may be taken with respect to δ, which will produce a constant value (the intercept of the linear fit will be discarded as the contact point is semi-constrained)

$$\frac{\Delta F^{1/B}(\delta)}{\Delta\delta} = \left[\frac{EA}{(1-\nu^2)}\right]^{1/B} = C \tag{3-29}$$

Therefore, the Young's modulus for a small piecewise bin of indentation data is approximated as

$$E = \frac{C^B(1-\nu^2)}{A} \tag{3-30}$$

For indenters that follow exact power-law behavior, such as the Hertz and Sneddon models, there will identically be no error in E if the zero force is correctly identified. For indenters that are not true power laws but are approximated as such, for example the sphere-conical or Briscoe models, the zero distance must be approximated due to the point at which the tip transitions into a cone need to be known. Figure 3-4C shows fits for the Young's modulus of a simulated sphero-conical curve when contact point errors (both in F and δ) are introduced. When the contact point is underestimated, the fits have a very small error because the zero force is known in this situation, whereas if the contact points are overestimated the errors increase. When simple least squares are used, errors in the Young's modulus increase harshly with errors in the contact point. This is because the linearized fit is only semi-constrained to the contact point, whereas a least-squares method is fully constrained to the contact point.

The error standard error from the fitting method may also be approximated. To first order this error, S_E, is

$$S_E^2 = \left(\frac{\partial E}{\partial A}\right)^2 S_A^2 + \left(\frac{\partial E}{\partial B}\right)^2 S_B^2 + \left(\frac{\partial E}{\partial C}\right)^2 S_C^2 \tag{3-31}$$

Where S_A, S_B, and S_C are the standard errors from the regression methods used. Solving the partial derivatives from Eq. (3-30) yields

$$S_E^2 = \left(\frac{E}{A}\right)^2 S_A^2 + (E \ln C)^2 S_B^2 + \left(\frac{BE}{C}\right)^2 S_C^2 \tag{3-32}$$

S_A and S_B will be very small for small indentation bins and virtually zero for exact power law relationships, so S_C will be the dominant term when analyzing experimental data unless very large binning intervals for non-power law functions are used.

Special care of the force-indentation data must be taken if there is adhesion between the probe and the sample due to an increased contact radius. There are several models to quantitatively account for adhesion, these have been recently reviewed by Lin *et. al.*[81].

Because the method is compatible for small segments of indentation data, this method may be used to determine the depth-dependence of the elastic force-indentation data to extract information regarding sample heterogeneity. Kasas *et. al.* demonstrated that the technique may be used to produce a "stiffness tomography" of the sample where certain regions have enhanced contrast due to elasticity variations[90]. Sokolov *et. al.* report on cell heterogeneity in the form of a extracellular brush of glycoproteins which may be detected using colloidal AFM probes and fit to entropic polymer models to determine length and grafting density[91].

Corrections to the elastic contact models to account for a rigid substrate have been derived (for example, the case of a thin soft layer resting on a glass coverslip). Dimitriadis *et. al.* solved the elastic contact model on a thin layer for a parabolic indenter by using the method of images for both a thin layer adhered and non-adhered to a rigid substrate[92]. Gavara and Chadwick made similar corrections for a conical indenter on an adherent thin elastic layer with ν=0.5[93]. Both of these solutions have the benefit of being closed-form equations which do not require expensive or tricky numeric techniques.

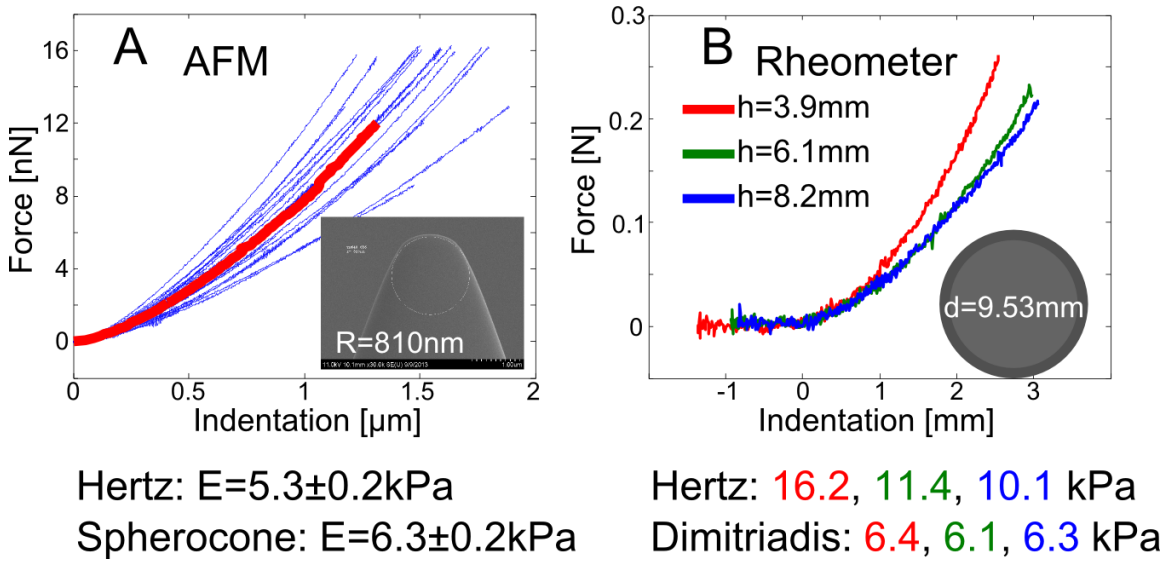

Figure 3-5: Comparison of AFM with bulk indentation rheometry on polyacrylamide gels. The concentration of acrylamide is 5% and bis-acrylamide is 0.2% and Poisson's ratio assumed to be 0.45. (A) Force-indentation curves collected with a LRCH-750 spheroconical tip on a JPK NanoWizard II in closed-loop, red shows an averaged curve while blue is all of the data. (B) Force-indentation curves collected by an Anton-Paar MCR302 rheometer with a 9.53 mm diameter bead glued to the measuring system. Thicknesses of the PA gels are shown. All of the data is fit with the described models, Dimitriadis[92] refers to the non-bonded case as the gel is not bonded with the substrate. The SEM image of the AFM probe is provided by Team Nanotec.

An example of a simple problem is shown in Figure 3-5, where a PA gel is probed by AFM and the same gel is measured in a bulk rheometer. In the case of the AFM, the tip radius is less than the total indentation depth, therefore care must be taken to ensure the correct model is used to fit the data. In the case of the bulk rheometry data, the gels are very thin compared to the size of the bead indenter, therefore care must be taken to ensure the data is fit to the proper model (in this case, the PA is not bound to the substrate so the non-bonded model by Dimitriadis[92] is used). When the proper models are used, the rheometer results are self-consistent and also agrees very closely with the AFM results (however, it should be noted that there is generally a 15% error in AFM force data from calibration).

Another example is shown in Figure 3-6, where a soft (3% acrylamide, 0.1% bis-acrylamide) PA gel is indented with an LRCH-750 AFM probe with sphero-conical geometry. The PA gel is prepared as described in §6 (with water instead of DPBS) and without further addition of fibronectin, and the measurement was performed in DPBS at 25°C. Different values for the Young's modulus are produced when different models are used to analyze the data. When the Hertz (Eq. (3-13) and Sneddon (Eq. (3-17) are used, there is a large dependence on the depth. However, when the model which best represents the shape of the tip is used, in this case the sphero-conical model (as shown in §5, also Appendix A) the depth-dependent apparent Young's modulus gives a more constant value over the entire indentation. When the fits are global and over the entire force-indentation curve (as opposed to binning the force into indentation bins), the resulting values for Young's modulus from the fits are 0.94, 0.72, and 0.94 kPa for the sphero-conical model, Hertz model, and Sneddon models, respectively.

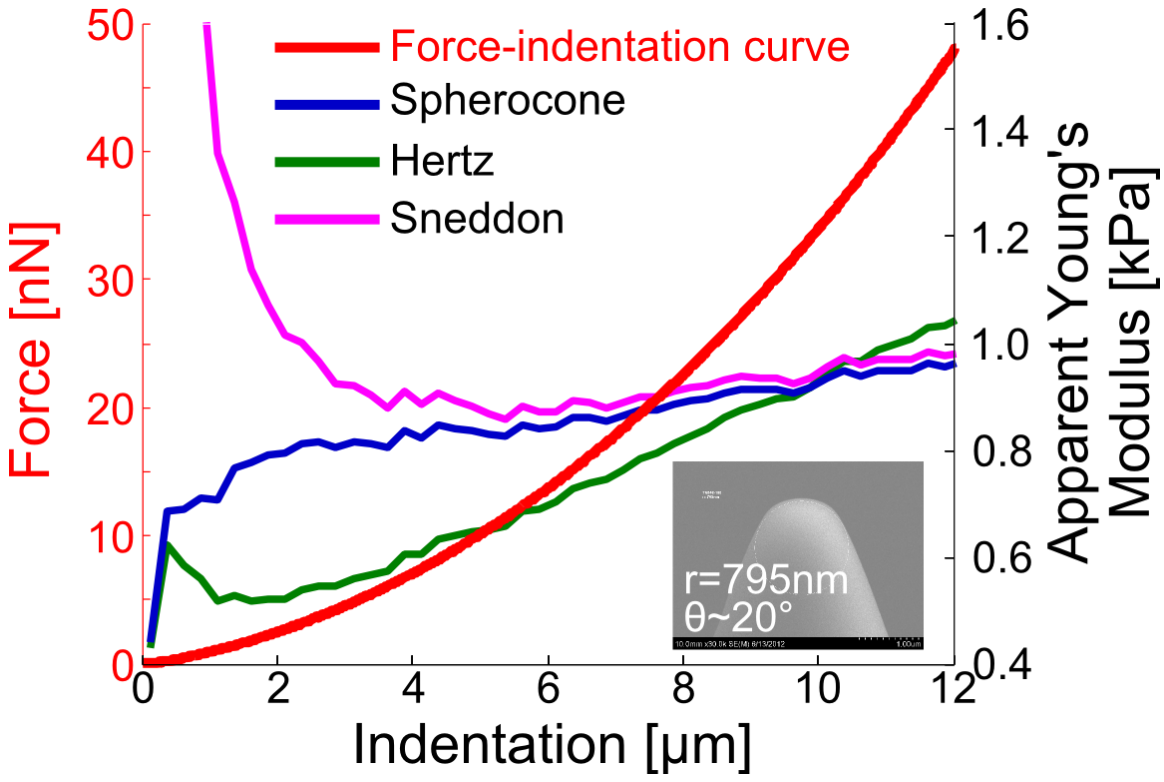

Figure 3-6: Force-indentation curve of a polyacrylamide gel with an LRCH-750 probe. The probe and SEM image are provided by Team Nanotec, the radius is 795 nm, the half-angle is approximately 20°, and spring constant ~0.13 N/m from the thermal tuning method. The fits assume ν=0.5. The AFM is an MFP-3D BIO, the velocity is 2 μm/s (closed loop), trigger force 50 nN, contact point chosen manually, and fit using the linearization method described in this chapter. The force is on the left axis, where the fits are on the right axis.

Atomic Force Microscopy Applications in Cell Mechanics

Quasistatic indentation-based microrheometry with an AFM is a very common established technique to measure elastic moduli for cells that have been adhered to some substrate. For example, Lim *et. al.* observed differences using AFM indentations between cancerous and non-cancerous mammary epithelial cells and also observed apparent stiffening at higher loading rates and correlated this with stress fiber bundling[94]. Ros *et. al.* used AFM indentation to examined mechanical differences of esophageal cell lines as they progressed from healthy to dysplastic phenotypes and observed a correlated

softening[88]. Nikkhah *et. al.* observed that the stiffness of breast epithelial cells has a slight dependence on the composition of the growth medium[95]. Janmey *et. al.* demonstrated with AFM indentation experiments that fibroblasts will adapt their stiffness to match their microenvironment under a certain threshold[40]. Plodinec *et. al.* performed AFM mapping across heterogeneous breast cancerous and healthy tissue regions and deconvoluted mechanical responses from the cells as well as the extracellular matrices[96].

AFM may also be used to create a "force clamp" in which a constant force or deformation is applied by a cantilever and the other is measured as a function of time. For example, Hyman *et. al.* used an AFM force clamp on mitotic HeLa cells to demonstrate a very large increase in intracellular pressure against an AFM cantilever during metaphase, and decrease during anaphase and demonstrated an interplay of osmotic pressure regulated by the actomyosin cortex contributing to the increase in pressure[97]. The spring constant of the cantilever may be used to modulate the local stiffness environment of a live biological sample to observe cellular response, Fletcher *et. al.* demonstrated a method using positional feedback loops to dynamically adjust the apparent spring constant of the cantilever to observe cell response to a changing stiffness[98] and use been used to examine the dependence of strain-rate in cell tensional response[99].

In addition to calculating static elastic moduli of samples, it may also be used to determine the viscoelastic moduli including the storage and loss components. This methodology was introduced by Käs *et. al.* by performing a series expansion on the Hertz model to introduce terms from small fluctuations in the indentation depth[100]. When the cantilever is oscillated, the force response will have some phase lag on a viscoelastic sample and the storage modulus is proportional to the cosine of the phase lag and the loss

modulus is proportional to the sine of the phase lag (a phase lag of zero is an elastic sample, 90° phase lag corresponds to a fluid with no elasticity). The method has been extended to use a conical indenter[101] and the process for determining the drag force of the cantilever (or instrument response function) has been further refined[102]. This method has been employed to observe power-law structural damping behavior of cells[101,102] whereby both the storage and loss moduli increase with increasing frequency and differences in the viscoelastic behavior between healthy and cancerous cells has been recently observed by Janshoff *et. al.* with cells having higher loss tangent at higher frequencies[103].

Related Techniques for Cell Mechanical Measurements

In addition its widespread commercial availability, AFM has the benefit of directly calculating the cells' mechanical response to external pressure, and the indenter geometry and location of indentation may be optimized to increase contrast of the location that is being studied. However, there are many aspects of cell mechanics which the AFM cannot address and experimental and theoretical limitations. As mentioned previously, while AFM can provide some information regarding the viscoelastic properties of cells, there are some instrumentation limits in determining the loss modulus due to varying cantilever spring constants. AFM is an active measurement method which needs to apply pressure directly to the top of the sample, thus cannot be used if the cell is too deeply embedded in some environment or is otherwise inaccessible. Very recently, Yamada *et. al.* demonstrated intracellular pressure measurements of cells in 3D microenvironments by penetrating the cell membrane with a microelectrode and showed an increase in intracellular pressure in the front edge of cells undergoing lobopodial

motility[37]. Passive methods which do not directly apply force to the sample and instead rely on optical microscopy may be used to determine effective material properties. A number of various techniques for examining the mechanical properties of whole cells, as well as single molecules and larger molecule complexes have been reviewed by several groups[104–106].

Another active cell mechanics measurement method is known as magnetic twisting cytometry, whereby magnetic beads are adhered to the outside of a cell, a strong magnetic field is applied to magnetize the ferromagnets, and a perpendicular magnetic field is applied to twist the beads with forces in the nanonewton range[107]. By examining the displacement field around the cell when the calibrated magnetic twisting force is applied, accurate microrheology data may be obtained[108]. Because the twisting force is purely a shear force on the membrane (unlike AFM which can only apply pressure in the normal direction), it may be used to study various mechanotransduction pathways in a cell, for example stretch-activated ion channels[109].

Cell mechanics of cells in suspension or adhered to a substrate may also be measured with micropipette aspiration[110]. A micrometer sized pipette is placed against a cell and a vacuum pressure is applied, forcing the cell to move into the suction volume – the amount the cell is displaced may be correlated with the amount of pressure applied. This method is also very useful for studying the rate dependence of deformation and may be applied to various viscoelastic models to determine the solid-like or liquid-like behavior of the cell[105], and has also been used to study elastic and viscoelastic contributions of cell nuclei[52]. Like AFM, micropipette aspiration requires the probe to form direct contact with the sample, so the applicability in 3D environments is limited.

Particle tracking microrheology is a technique in which sample mechanical properties are extracted by examining the diffusion of a particle within a viscoelastic fluid. The method is based on the time-dependent Einstein-Stokes equation and the relationship between the diffusion rate from thermal noise, the complex modulus of the medium, and the displacement[111]. Once the diffusion displacements and times are known, the storage modulus and loss modulus may be deconvoluted (additionally, model-free results may be generated by simply comparing diffusion displacements versus time). This method has been widely used with both endogeneous probes[112] and probes that are ballistically injected[113] into the cell (for example fluorescent microspheres) and has been recently extensively reviewed by Wirtz[114]. Results from particle tracking rheology and AFM indentation-based rheology have been shown to differ significantly with AFM having elastic moduli orders of magnitude higher, however this may be due to the particle tracking having little to no influence on the cell cortical rigidity, whereas AFM indentations may be directly probing the cortex[115]. Because this is an optical far-field technique and direct physical access to the cell is not needed, this method may be used to study mechanics of cells in a 3D environment[116].

In addition to using optical lasers for viewing of fluorescence molecules, lasers may be used to generate mechanical forces on dielectric particles that are either much larger than the wavelength of light (demonstrated by conservation of momentum of scattering photons) or much smaller than the wavelength of light (demonstrated by dipole scattering and movement along the laser's intensity gradient)[117]. The technique has a rich history; it was first demonstrated in 1970 with multiple beams[118], the single-beam optical trap was demonstrated in 1986[119] and was applied to directly manipulate whole cells and

viruses in 1987[120,121]. Like the AFM, several methods are available for calibrating both the positions and trapping force magnitudes of optical trapping (or tweezing) and several rely simply on understanding the contributions thermal energy fluctuations inside of the optical trap, these methods have been recently reviewed[117]. Single molecules may be attached to beads subject to optical tweezing, producing a form of force spectroscopy which has a resolution on the femtonewton scale[122]. Single cell mechanics may also be studied by using force spectroscopy by attaching a bead to a cell and pulling the cell apart via optical tweezing[123], and this method is capable of reaching very large non-linear cellular deformations[124].

In addition to optical trapping, lasers may be used in another creative way to study cell mechanics via optical stretching. By applying light beams on either side of a soft dielectric sample, the sample will be stretched along the axis of the beams due to light reflection on interfaces of varying refractive index and conservation of momentum of photons[125]. The optical stretcher is capable of forces on the order of hundreds of piconewtons with sufficient laser power, and performing the assay on cells in suspension does not contribute significantly to cell death[126]. The method has been applied to mammalian breast cells of varying stages of metastatic progression and has demonstrated that the more metastatic cells (MDA-MB-231) are more deformable than cells which are not as aggressive (MCF-7, MCF-10A)[127]. One key difference between this method and AFM is that the cells are in suspension, whereas AFM can only measure cells that are adherent – however, cells in suspension have been demonstrated to have an intact actin cytoskeleton, including an actin cortex, but no stress fibers as adherent cells have[126].

Very recently, a technique has been developed by Guck *et. al.* to measure the mechanical deformation resistance of cells in suspension in a microfluidic device with at a very rapid rate (>100 cells/second)[128]. A similar technique has been developed by Di Carlo *et. al.* in 2012[129]. Cells are flowed at a controlled rate into a small microfluidic channel and non-laminar flow causes the cells to compress – the cells are quickly imaged under shear flow, producing high-throughput cell size and deformation data. This technique has been used to differentiate cells in various cell cycle phases, and has the potential to be combined with other high-throughput techniques such as fluorescence-activated cell sorting or other flow cytometry techniques.

As previously discussed, AFM may be used to study a cell's response to changes in environmental stiffness by employing a force clamp. Another platform to study this is a by creating an array of PDMS posts for cells to grown on, whereby the effective stiffness of the post may be tuned by adjusting the physical dimensions (length, diameter) and cell adhesion proteins may be readily attached[130,131]. Additionally, the traction forces generated by cells may be quantitatively measured with this technique by determining the deflection of the pillars with optical microscopy. The actual measurements are made with non-invasive far-field microscopy, however the microenvironment of the cells is physically constrained by pillars.

Computation Techniques for Soft Matter Rheology

Methods of interpreting data from cell mechanics measurements using analytical classical elastostatics has many severe drawbacks. Only relatively simple situations have analytical solutions, for example infinite materials and spherical inclusions, and typically

these must be purely elastic, homogeneous, and isotropic. Even qualitatively simple problems, for example elastic indentation into a layered material[132], do not have simple closed-form equations that may be readily used for data analysis. The equations governing elastic theory to determine stress and strain relationships are differential equations (for example, Appendix 1 for time-independent conditions in cylindrical coordinates) and thus the solution is determined by the boundary conditions. Hence, finite element analysis is used in situations where analytical tools do not work. The finite element method is a very robust tool for solving boundary value problems, and can simulate virtually any imaginable geometry as well as complex load or deformation conditions.

The key assumption of the finite element method is that the continuum problem may be replaced by a discretized version. A mesh for the object is generated containing nodes (points) and elements (connections between the nodes) using a predetermined shape (for example, a triangle for 2D or tetrahegon for 3D) and corresponding shape function. Because the shapes of the mesh elements are well known, the solution to the differential equation becomes straightforward as they are easily differentiable and integrated. Thus the complicated differential equation is reduced to a simple matrix equation $\boldsymbol{F} = \boldsymbol{K}\boldsymbol{x}$ where $\boldsymbol{F}$ and $\boldsymbol{x}$ are one-dimensional arrays of nodal information and $\boldsymbol{K}$ is a two-dimensional matrix which contains all information regarding imposed boundary conditions, solutions to the shape functions, and details of the differential equation (e.g. sample stiffness). Key parameters to control during finite element modeling are the mesh sizes and incremental step sizes, as poor choices in these may lead to numeric instability.

As the problem is reduced to matrix operations, the run-time of the analysis may scale very poorly with the number of nodes (or mesh size) in the system.

One novel technique for modeling dynamic cell rheology is the subcellular element model[133–135]. Here, cells are represented by a cluster of nodes connected by springs resembling a Morse potential containing repulsive short-range forces and weakly attractive long-range forces. The internodal potentials may be adjusted depending on the model, for example intracellular versus intercellular nodes. The node positions are updated throughout time using the Langevin equation with some added damping factor until equilibrium is reached, however it may be generally used to model non-equilibrium processes present in cell biology. Hence, it may be used as a mesh-free viscoelastic solid model and a 3D mesh of Kelvin-Voigt springs with the dissipative elements grounded to the environment. Microrheology simulations may be performed on the subcellular element model and a viscoelastic power-law behavior is observed[133]. Emergent multicellular behavior such as embryonic tissue organization and single cell invasion have also been modeled using the subcellular element model[134].

While the subcellular element model contains a Morse potential to contain weak long-range adhesion, it may also be adjusted to use simple Hookean springs in a lattice spring model[133]. However, one drawback is only 1D normal forces are considered in this framework. The distinct lattice spring model[136] is an extension to this where shear springs may also be considered in addition to normal springs. These shear springs allow a more formal definition of the emergent solid's Poisson's ratio and Young's modulus, which is somewhat difficult to tune in classic lattice spring models by increasing the amount of crosslinking. One drawback of the shear spring is that they contain a negative spring

constant for Poisson ratios higher than 0.25, thus lead to very instable solutions for incompressible solids.

4 ANALYSIS OF AFM FORCE-INDENTATION DATA ON HETEROGENEOUS SAMPLES

This chapter details a study on analyzing force-indentation curves on heterogeneous samples. This is an adaption from a manuscript in preparation by Bryant L. Doss (BLD) and Robert Ros (RR). The theoretical framework, finite element simulations, and experiments were developed and performed by BLD. This work was supported by a grant from the National Cancer Institute (U54CA143862) awarded to RR.

Introduction

AFM is a very commonly used technique to investigate the elasticity of biological and other soft matter samples. Once the raw force-indentation data is obtained, generally the goal is to approximate the sample as being elastic with some Young's modulus. However, as detailed in §3, biological samples fall very short of the assumptions made in classical elasticity theory[80,82]: deformations are often large compared to the size of the sample, the samples are not infinite, homogeneous, isotropic, linearly elastic half-spaces, and temporal effects also play a role. The Poisson ratio of the material is also generally unknown and cannot be determined from AFM alone, but is typically approximated to ~0.5 for biologic materials[137] to represent an incompressible material (although this may not be exactly true).

Previous studies have attempted to address the deviations from these assumptions in soft matter. Dimitriadis *et. al.* demonstrated corrections to the Hertz model for samples with finite thickness both adhered and non-adhered to a stiff substrate using a method of

images approach[92], and later Gavara and Chadwick demonstrated similar finite thickness corrections for the Sneddon model[93]. For heterogeneous samples with non-stiff substrates, much less deterministic work has been published. Kosta *et. al.* developed a finite element analysis method for two-layered samples[138] based on Eshelby's theory, but their presented theory is not generalized for all problems. Vargas-Pinto *et. al.* showed with finite element analysis and experiments on live cells that sharper AFM probes are more sensitive to the top layer of the sample than colloidal beads[11]. Akhremitchev *et. al.* also showed finite thickness corrections for multiple tip shapes for various elastic foundations[83] using the same theory that is employed in this work.

Theory

In 1970, Dhaliwal and Rau[132] developed an extension to Sneddon's 1965 work[80] for a generalized solution to the Boussinesq problem for an elastic layer adhered to another elastic foundation using the elastic equilibrium equations. The end result is a Fredholm Integral Equation of the Second Kind

$$\phi(t) + \frac{a}{h\pi}\int_0^1 K(x,t)\,\phi(x)dx = -\frac{E_1 a}{2(1-{\nu_1}^2)}[\delta - \beta(t)] \tag{4-1}$$

$$F = -4\int_0^1 \phi(t)dt \tag{4-2}$$

$$\phi(1) = 0 \tag{4-3}$$

where a is the contact radius between the probe and the sample, δ is the probe indentation depth, h is the distance from the top of the first layer to the interface with the second layer (height of the first layer), E_1 is the Young's modulus and ν_1 is the Poisson ratio of

the first layer, F is the applied force of the probe, and β is a function describing the axisymmetric shape of the tip defined by f:

$$\beta(t) = t\int_0^t \frac{f'(r)}{\sqrt{t^2 - r^2}}dr \tag{4-4}$$

where $0<r<1$ and the kernel K is smooth across the entire interval and is defined by

$$K(x,t) = 2\int_0^\infty H(2u)\cos\left(\frac{a}{h}tu\right)\cos\left(\frac{a}{h}xu\right)du \tag{4-5}$$

$$H(u) = -\frac{d + g(1+u)^2 + 2dge^{-u}}{e^u + d + g(1+u^2) + dge^{-u}} \tag{4-6}$$

$$d = \frac{(3-4\nu_1) - \mu(3-4\nu_2)}{1 + \mu(3-4\nu_2)} \tag{4-7}$$

$$g = \frac{1-\mu}{\mu + 3 - 4\nu_1} \tag{4-8}$$

$$\mu = \frac{E_1(1+\nu_2)}{E_2(1+\nu_1)} \tag{4-9}$$

with E_2 and ν_2 being the Young's modulus and Poisson ratio for the bottom layer, respectively. The relationship between δ and a will not be the same as it is in the case of indenting a half-space and must be determined numerically using Eq. (4-3). An illustration of the two-layer indentation problem is demonstrated in Figure 4-1A.

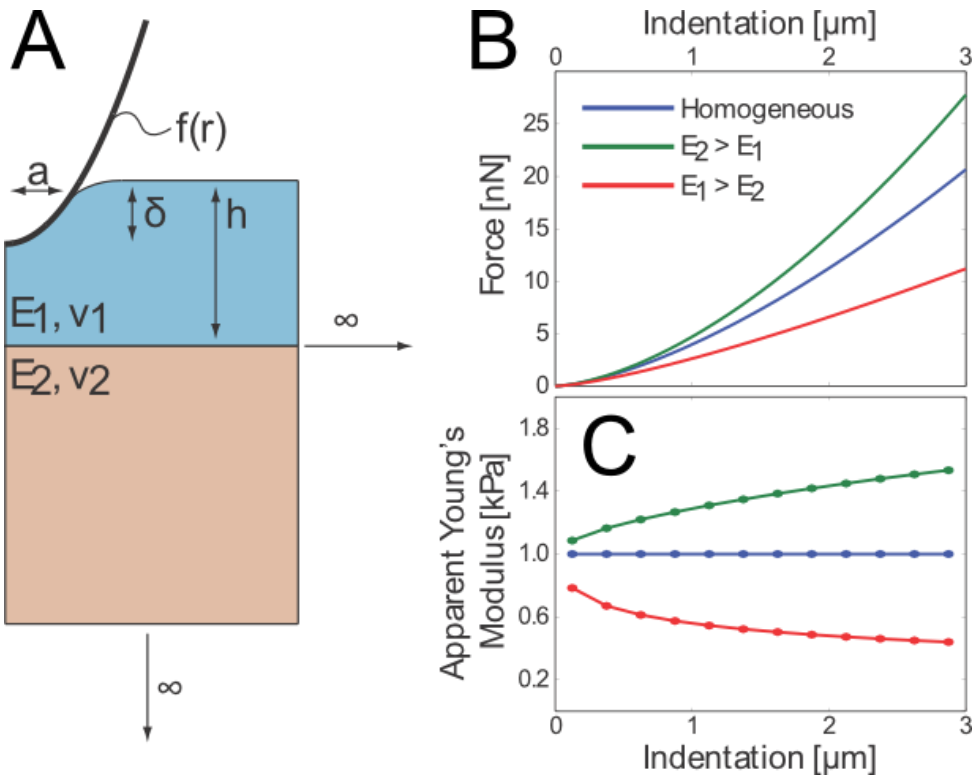

Figure 4-1: Elastic indentation problem on a bonded two-layer material. (A) Cartoon illustrating the physical dimensions of the problem, including the tip shape and substrate properties. (B) Theoretical force-indentation curves generated from Eqs. (4-1)-(4-9) showing how the substrate effects can affect the force response of an AFM probe. In these examples, E_1=1 kPa, E_2=1 kPa, 2.5 kPa, or 0.25 kPa for the case of the homogeneous, $E_2>E_1$, and $E_1>E_2$, respectively, h=9 μm, the tip is parabolic with R=5 μm, and $\nu_1=\nu_2$=0.5. (C) Piecewise depth-dependent fits using the Hertz model of the force-indentation curves. In the homogeneous case, the Hertz model provides a constant Young's modulus for all indentation depths, but the two-layer case is non-uniform over indentation depths and differs from the value E_1=1 kPa.

Eq. (4-1) may be solved using either a series expansion[132] or directly by a numeric algorithm such as the Nyström method[139] as done in the present work. Eq. (4-3) is solved by using the MATLAB built-in function fzero. Example force-indentation curves and their piecewise depth-dependent fit for a parabolic (Hertz model) indenter are shown in Figure 4-1 B, C.

To determine E_1 given h and E_2, the MATLAB built-in function fminsearch is used by minimizing differences in the depth-dependent E between the experimental data and numeric solution until convergence is reached within a specified tolerance. The protocol detailed in Appendix C demonstrates another method for performing the deconvolution.

This approach may also be used in the case of samples with finite thickness and a rigid substrate by setting μ=0. The results are similar to that shown by Dimitriadis *et. al.*[92] but differ from the case given by Gavara and Chadwick[93]. However, due to the formulation, errors arise when $\delta \rightarrow h$.

One drawback from directly solving the above is that it is computationally expensive to simultaneously solve Eqs. (4-1), (4-2), and (4-3), as well as rather cumbersome and complex to employ as a routine algorithm for data analysis. From the above equations, when the Poisson ratios are fixed, the problem may be reduced to two generalized parameters a/h and E_1/E_2 as normally $F \propto E_1$ so the lone E in Eq. (4-1) may be neglected. Hence, it is feasible to rewrite the above equations into simpler, closed-form equations for specified v, v_2, and f. The following dimensionless parameters γ and α are introduced

$$\alpha = a/h \tag{4-10}$$

$$\gamma = log_{10}(E_1/E_2) \tag{4-11}$$

The logarithm and base is chosen out of numeric convenience such that $-1<\gamma<1$ for an order of magnitude elastic mismatch, $\gamma>0$ for all mismatches, and γ is symmetric about E_1 and E_2. We may approximate corrections to the homogeneous force-indentation equations

in a two-dimensional Taylor series approach (for numeric details see Appendix B). For the Hertz model,

$$\alpha_H = \sqrt{R\delta}/h \tag{4-12}$$

$$F_H \approx \frac{16E_1\sqrt{R}\delta^{3/2}}{9}\exp\begin{pmatrix} -2.20\alpha_H\gamma - 0.02{\alpha_H}^2\gamma - 1.90\alpha_H\gamma^2 \\ +1.21{\alpha_H}^3\gamma + 3.19{\alpha_H}^2\gamma^2 - 0.90\alpha_H\gamma^3 \end{pmatrix} \tag{4-13}$$

where R approximates the probe radius and $\nu=\nu_2=0.5$. For the Sneddon model,

$$\alpha_S = 2\delta\tan\theta\,/(\pi h) \tag{4-14}$$

$$F_S \approx \frac{8E_1\delta^2\tan\theta}{3\pi}\exp\begin{pmatrix} -2.20\alpha_S\gamma - 0.02{\alpha_S}^2\gamma - 1.90\alpha_S\gamma^2 \\ +1.13{\alpha_S}^3\gamma + 3.62{\alpha_S}^2\gamma^2 - 0.90\alpha_S\gamma^3 \end{pmatrix} \tag{4-15}$$

where θ approximates the cone half-angle and $\nu_1=\nu_2=0.5$. It should be noted that the contact radius a will not be the same as in the homogeneous case, however it is sufficient for approximating the perturbations to the force-indentation response. For $\alpha=0$ or $\gamma=0$, the equations reduce to the homogeneous case.

Materials and Methods

Sample Preparation

Polydimethylsiloxane (PDMS, Sylgard 184, Dow Corning) gels were vigorously mixed at described ratios and degassed under vacuum. Small droplets of the mixture were added to a 22 mm glass coverslip is spun using a home-built spin-coater to spread the mixture into a thin layer (typically 15-50 μm, depending on rotation speed). The mixture was allowed to cure at 65°C for at least 4 hr. Once polymerized, the PDMS thickness was measured using an inverted confocal laser scanning microscope (MicroTime 200, PicoQuant, Germany) with z-piezo positioning (Physik Instrumente, Germany) to measure the distance between intensity peaks in the reflected laser light due to changes in

refractive index. Prior to indentation experiments, the PDMS is plasma cleaned in O_2 to make the surface hydrophilic.

Atomic force microscopy indentation

Indentation experiments were performed using an MFP-3D (Asylum Research, California) in closed-loop mode. A borosilicate microsphere with diameter 10 μm (Duke Standards) is glued (Norland Optical Adhesive) to a tipless cantilever with high spring constant (ACT-TL, AppNano, k=42.42 N/m from the thermal tuning method[71,75]) and cured with UV light. Measurements were performed at 25°C in phosphate buffered saline and the loading rate was 1 μm/s.

Finite element analysis

Finite element modeling and simulations were performed using ANSYS Workbench 14.0. The models were axially symmetric around the center of the tip and sample to increase computational efficiency. The AFM tip was modeled as with dimensions similar to those used in the experiment and Young's modulus on the order of GPa. The tip had a triangular mesh size of 100 nm and the contact between the tip and sample was assumed to be frictionless. The top layer of the material had a triangular mesh size of 250 nm and tapered to larger values at a distance of 5 μm from the tip. Both layers were modeled as an Ogden 1st order solid (α_1=2, identical to Neo-Hookean solid) with radius 100 μm and Poisson ratio of 0.48. The combined height of the top and bottom layers was 100 μm with a fixed support on the bottom boundary. The top layer and bottom layer were bonded together such that there was no separation between the

elements. All elements had midside nodes. The AFM tip was lowered into the sample in increments of several nanometers and a force-indentation response is computed. A screenshot of an indentation is shown in Figure 4-2A.

Data analysis

Force-indentation data was analyzed using home-built routines in MATLAB. The integral transform equations (4-1)-(4-9) are solved using a combination of the Fredholm Integral Equation of the Second Kind program written by Atkinson and Shampine[139] and the built-in fzero routine in MATLAB, producing a theoretical force-indentation curve given the tip shape, elastic properties of the top and bottom layers, and height of the top layer. The Young's modulus wass computed in a depth-dependent piecewise fashion using the linearization method (explained in §3).

Results

Force-indentation curves generated using finite element modeling, the integral transform method Eqs. (4-1)-(4-9), and the series approximation for a parabolic indenter Eq. (4-13) are shown in Figure 4-2B, along with the homogeneous case calculated from the Hertz model in Eq. (3-13). Each method shows a distinct difference from the homogeneous case, and the three methods for heterogeneous case all show strong agreement in their deviation from the homogeneous case. We next tested the accuracy of how the observed force from the two-layer method differs from the force of the homogeneous case of the integral transform method and the series approximation for both parabolic and conical indenters with finite element analysis for a large amount of elastic

mismatches, which is shown in Figure 4-3. Because the series expansion is centered about the homogeneous case α=0 and γ=0, we expect that the results of the series approximation will be very much in agreement with the integral transform method for small values of α and γ, as the coefficients determined in the series expansion are based on the results of the integral transform method. We observed that the series approximation begins to diverge from the integral transform solution approach around $|\alpha|>0.5$ and $|\gamma|>0.5$, thus the series expansion approach yields good agreement for $\alpha<0.5$ and $|\gamma|<0.5$. We also observe that for the values tested, the integral transform method shows high agreement with the finite element simulations except for small deviations for parabolic indenters and low γ (the case of an elastic material bonded to a rigid substrate).

We next tested the ability of the integral transform and series approximation methods to deconvolute the Young's moduli of the two layers from force-indentation curves generated with finite element analysis. The force-indentation curves from finite element analysis, along with the depth-dependent apparent Young's moduli from Eq. (3-13) and the two-layer theory are shown in Figure 4-4. For the indentation depths and elastic mismatches tested, the minimization method by comparing the apparent Young's modulus in each bin with a generated force-indentation curve from theory was capable of separating the Young's modulus of the top and bottom layer when one is already known along with the height of the first layer. Therefore, only one parameter (E_1, E_2, *or* h) is computed from each force-indentation curve as opposed to fitting a single curve to multiple parameter (E_1, E_2, *and* h). Figure 4-4A and Figure 4-4C perform the deconvolution using the integral transform method, while Figure 4-4B employs the series approximation as the elastic mismatch falls within the acceptable values of α and γ.

We next tested how errors propagate using the fitting procedure, as the method is dependent on knowing the Young's modulus of either layer to determine the modulus of the unknown layer. In Figure 4-5, we generated a collection of force-indentation curves from theory and performed the 1-parameter deconvolution while imposing incorrect values for the known layer and observe how these translate into errors for the layer which we are trying to determine. For determining the top layer in the case of $E_2>E_1$ (Figure 4-4A), errors in E_2 to not become large errors in E_1 for smaller values of α, but become on the same order for deep indentations or shallow layer heights around α=0.5. For determining the top layer in the case of $E_2<E_1$ (Figure 4-4C), errors in the determining the top layer are small for small α, but are approximately on the same order as the error for the known layer around α=0.25 and become much higher for larger α. Errors are extremely large when attempting to determine the Young's modulus of the bottom layer when small errors in the top layer are imposed, as shown in Figure 4-4B and Figure 4-4D, especially in the case of $E_2>E_1$. For deep indentations or shallow layer heights, it is reasonable to determine the bottom layer in the case of $E_2<E_1$. Larger errors in determining the Young's modulus of the bottom layer are not unexpected as the probe is always in contact with the top layer thus the signal from the force-indentation response should generally be dominated by the Young's modulus of the top layer except in the case of $E_1>>E_2$.

To help understand how the bottom layer contributes to the force-indentation signal from the top layer, we wanted to see how the elastic mismatch and contract radii terms contribute to the signal. Figure 4-6 shows the contour lines of the effect on the force for the two-layer model for large values of elastic mismatch and α describing the

contact radius, indentation depth, and layer height. It can be seen that in the regime of a stiff substrate, the signal saturates for $E_2 >> E_1$ and the dominant term is α. In the regime of a softer substrate, the dominant term is the elastic mismatch and the effects are felt for even small values of α.

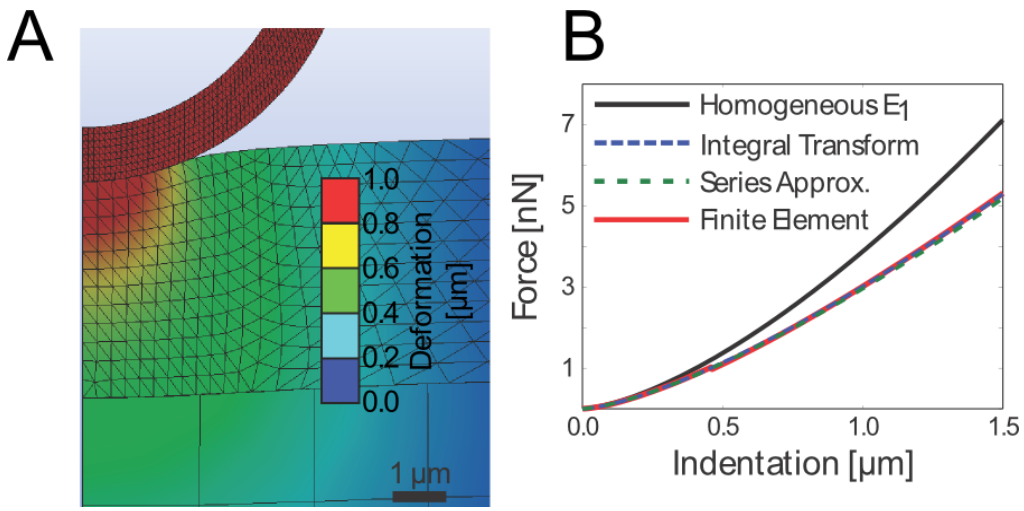

Figure 4-2: Finite element analysis on two-layer bonded samples compared with theory. (A) Screenshot of the axisymmetric elastic indentation using ANSYS Workbench 14.0. The mesh element lengths are ~100 nm for the tip, ~250 nm for the first layer of the elastic substrate which tapers to a larger value at a distance of 5 μm from the bottom of the tip, and ~1.5 μm for the second layer. The colorbar shows the deformation of each node from the initial position and can be used to visualize the "indentation field". (B) Force-indentation curves generated with finite element, the integral transform theory Eqs. (4-1)-(4-9), and the two-layer empirical series approximation Eq. (4-13). E_1=1 kPa, E_2=0.4 kPa, h=9 μm, the tip is spherical with R=5 μm, and ν=ν_2=0.48 for the integral transform and finite element, and 0.5 for the series approximation as required. The black curves shows the case for a homogeneous indentation with E_1=1 kPa.

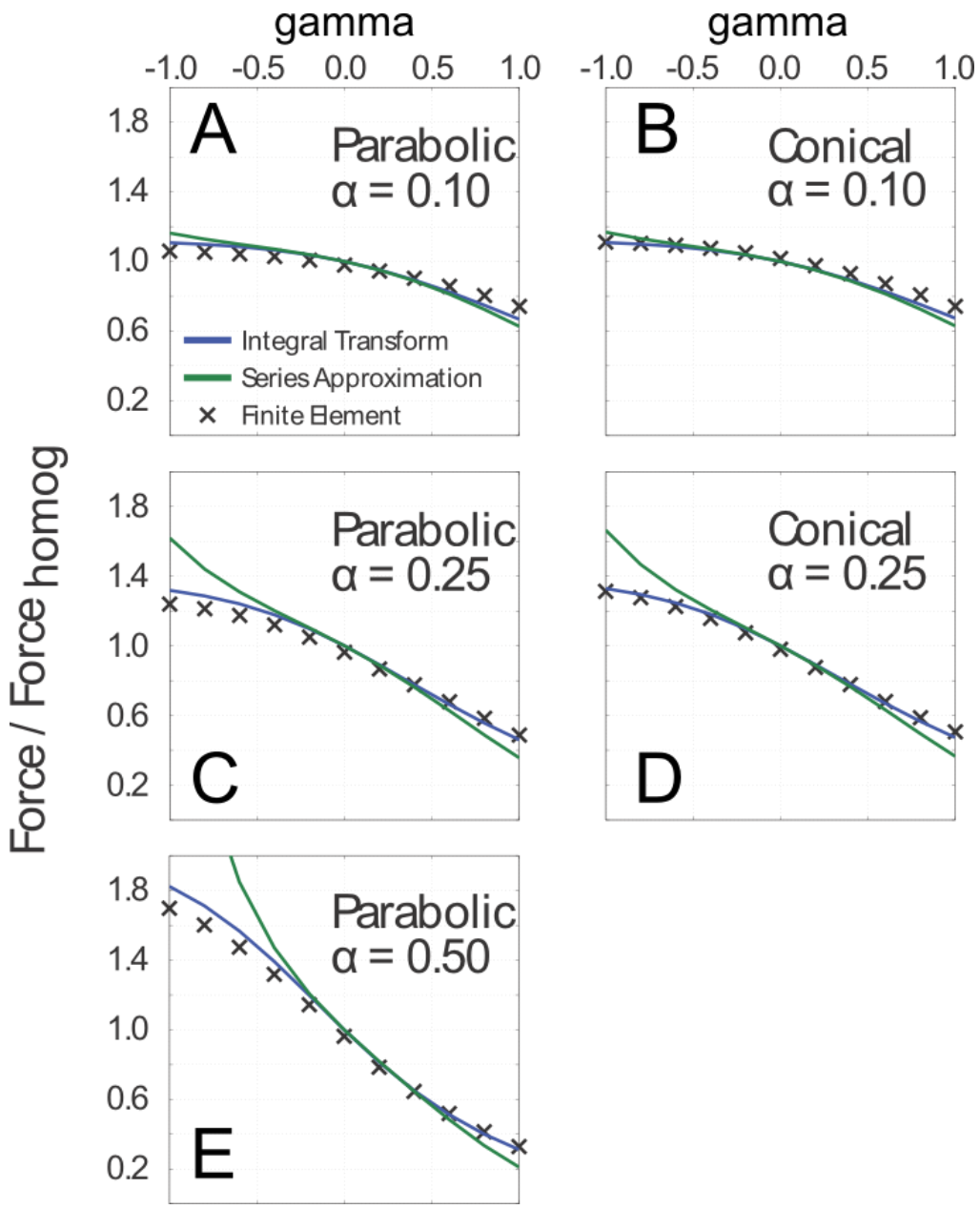

Figure 4-3: Comparison of finite element, integral transform, and series approximation for two-layer samples. (A), (C), and (E) show values for the parabolic (Hertz) indenters, and (B) and (D) show values for conical (Sneddon) indenters, (A) and (B) show values for α=0.1, (C) and (D) show values for α=0.25, and (E) shows values for α=0.5. For high values of α and γ, the series approximation diverges from the integral transform and the finite element results. A conical indenter with α=0.5 is not shown because an extremely deep indentation with $\delta > h$ is required, and the two-layer theory is not valid for these indentation depths.

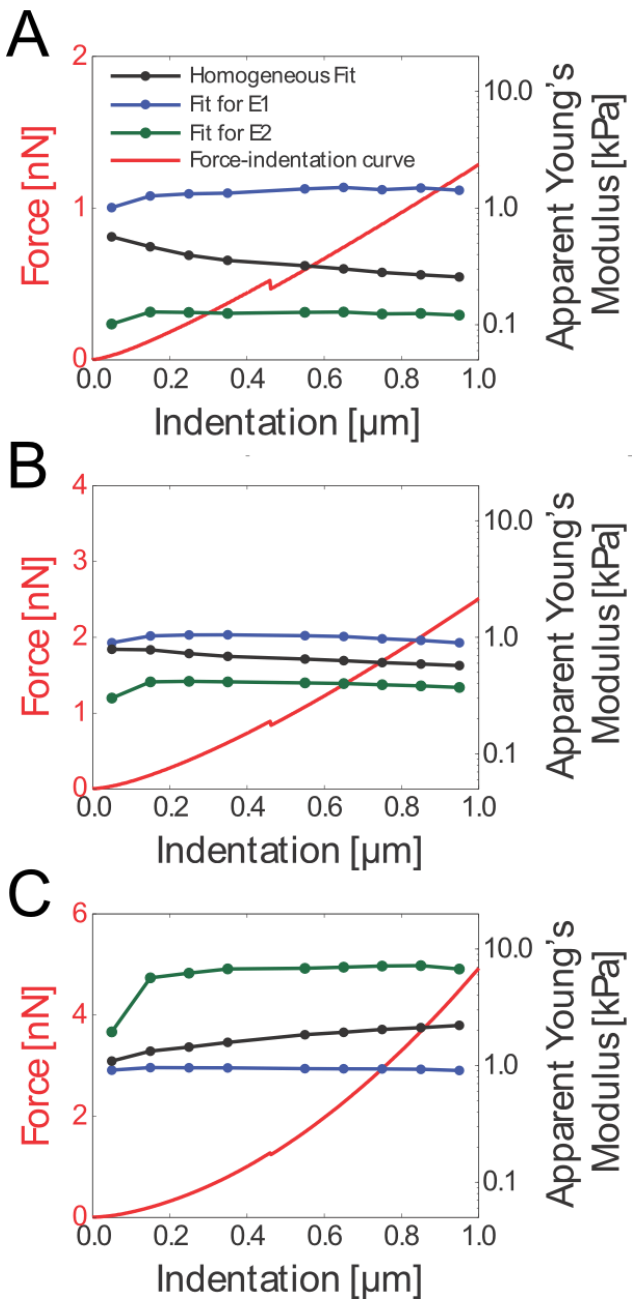

Figure 4-4: Two-layer theory for deconvoluting top and bottom layer elastic moduli. The force-indentation curves that are fit are generated using finite element analysis. For all cases, E_1=1 kPa, h=4.5 μm, the tip is spherical with R=5 μm, and ν_1=ν_2=0.48, and (A) E_2=0.1 kPa, (B) E_2=0.4 kPa, and (C) E_2=10.0 kPa. The fits for the Young's moduli are overlayed with the force-indentation curve in red. Black shows the fit using the standard Hertz model, blue shows the fit for E_1 using the layered theory with known E_2, and green shows the fit for E_2 using the layered theory with known E_1. (A) and (C) are fit using the integral transform Eqs. (4-1)-(4-9), and (B) is fit using the series approximation Eq. (4-13). The bin from 400-500 nm is skipped due to a mesh artefact visible in the force-indentation curve.

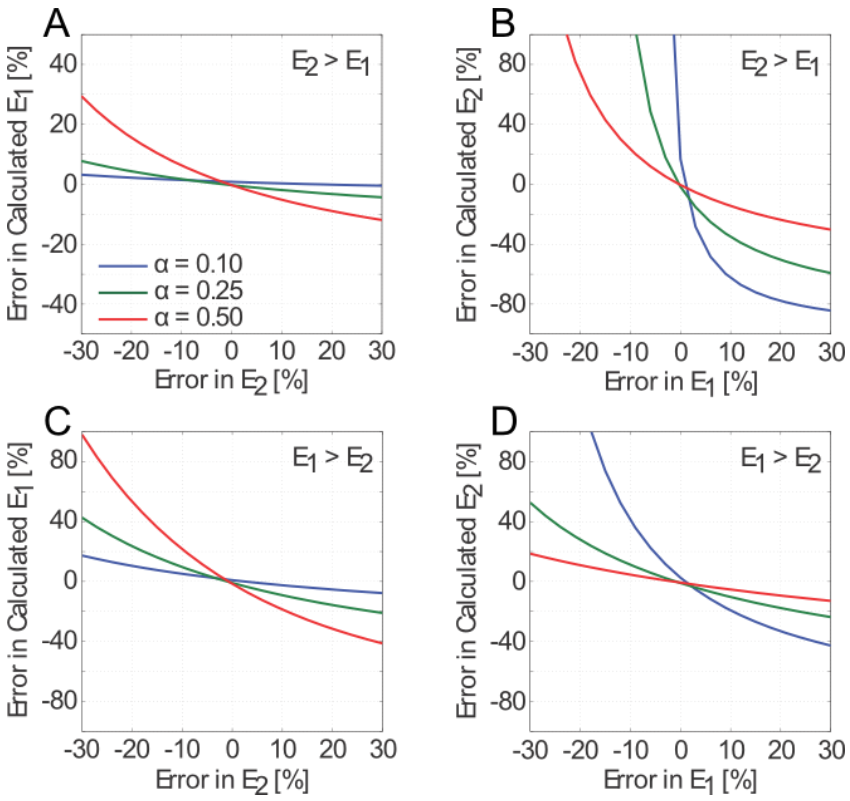

Figure 4-5: Error propagation of the two-layer theory when correcting for the effects elastic mismatch. Deconvoluting the moduli requires knowledge of one layer to determine the other, however if there is an error in the assumed modulus of one layer, the error will propagate to the calculation of the unknown layer. A theoretical force-curve is generated using integral transform method Eqs. (4-1)-(4-9) and it is deconvoluted using different parameters. (A) and (B) show the case of a stiffer bottom layer, and (C) and (D) show the case of a softer bottom layer. (A) and (C) show the case of determining E_1 with an assumed E_2, and (B) and (D) show the case of determining E_2 with an assumed E_1. The x-axis depicts an error in the assumed modulus, and the y-axis is the corresponding error in the calculated modulus. Blue shows α=0.1, green shows α=0.25, and red shows α=0.5. These graphs show under which conditions an error in the assumed modulus can lead to a divergent error in the calculated modulus. For all cases, E_1=1kPa, the tip is spherical with R=5µm, $\nu_1 = \nu_2$=0.48, (A and B) E_2=4.0 kPa, (C and D) E_2=0.25 kPa, (blue) h=24 µm, (green) h=9 µm, (red) h=4.5 µm, the indentation depths are 1 µm, and the fits use a 100 nm bin.

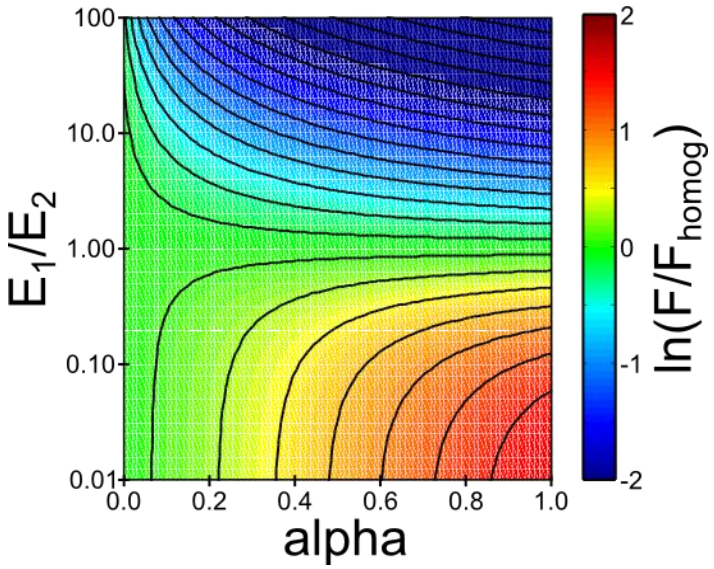

Figure 4-6: Image depicting contour lines of the two-layer model in elastic mismatch and α. For a stiffer substrate ($E_2>E_1$), the signal saturates for defined α. For a softer substrate, the dominant term is ($E_2<E_1$), the dominant term is the elastic mismatch and substrate effects are seen for smaller α. Image was generated using the integral transform two-layer model with a parabolic indenter.

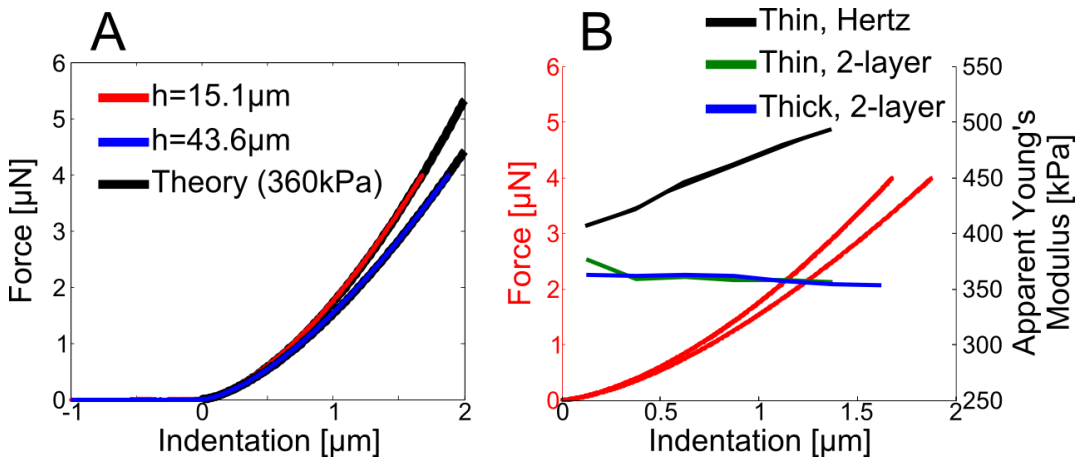

Figure 4-7: Force-indentation curves and 2-layer elasticity fits on thin PDMS gels. The base:crosslinker ratio was 22.5:1, resulting in a ~360 kPa gel, and the probe radius is 5 μm. (A) raw force-indentation data for two gels with different thickness (15.1 μm is red and 43.6 μm is blue) and the corresponding fits using the 2-layer model (black). (B) The force-indentation curves (red, left axis) and corresponding depth-dependent apparent Young's modulus (right axis) using the standard Hertz model (black), and the 2-layer corrected models (15.1 μm is green and 43.6 μm is blue). With the correction, the moduli converge on the same flat line, however up to 35% error is observed without this correction.

AFM force-indentation experiments were conducted on thin PDMS gels a using borosilicate bead with diameter 10 μm which were deposited onto glass coverslips via spincoating, and the thickness was measured using back-reflected laser light from confocal microscopy. The force-indentation curves collected from the thin PDMS gels are shown in Figure 4-7A overlaid with the theoretical force-indentation curves produced using the integral transform equations (this is needed as μ=0 for a stiff substrate so the series expansion is not valid) and shows very strong agreement. Figure 4-7B shows the depth-dependent apparent Young's modulus from the curves on thin PDMS. When the correction derived from the theory is not applied, the apparent Young's modulus increases with indentation depth, however when the correction is applied to both gels, they show agreement in Young's modulus as well as relatively constant apparent Young's modulus with indentation depth. The results here also agree strongly with the bonded thin layer model developed by Dimitriadis *et. al.*[92]. Thus, the two-layer model is capable of explaining results from both finite element simulations as well as experiments on ideal PDMS elastomers.

Discussion

We have extended the work of Dhaliwal and Rau[132] to examine AFM indentations on bonded two-layer materials in length and elasticity scales comparable to those seen in soft matter experiments. In addition to solving the integral transform equations, we have simplified the model to a Taylor series equation and have shown that both the integral transform method and series approximation for small α and γ agree with finite element

analysis (Figure 4-3). These models may be used to deconvolute the Young's modulus from force-indentation curves generated with finite element analysis using a 1-parameter minimization method (Figure 4-4), as well as experimental data on thin layers of PDMS (Figure 4-7).

From these results, the model shows several predictions of how AFM indentations on heterogeneous materials will behave. In the case of $E_1<E_2$ (a soft elastic material bonded to a more rigid substrate), the dominant term affecting how the substrate affects the force-indentation response is α, the dimensionless parameter describing the ratio of the contact radius to the layer height. When the substrate is extremely rigid compared to the top layer ($E_1<<E_2$) the signal saturates and the parameter γ that describes the mismatch in elastic moduli loses significance. The model does not predict asymptotic behavior, thus it is unable to determine the force-indentation response when the probe indents and makes contact with the second layer and does not predict the appropriate response when the indentation depth is very near to the second layer (δ greater than or equivalent to h)

In the case of $E_1>E_2$ (the top layer is more rigid than its substrate), the dominant term in the change to the force-indentation response is the elastic mismatch γ. The effects of the substrate are noticed in the force-indentation response at even small indentation depths relative to the layer height. The physical explanation of this is that when the top layer is more rigid and is indented it will push onto the bottom layer, and the deformation in the bottom layer will be much larger than the case of $E_1<E_2$. As such, the model still holds reasonable accurate for large values of δ with respect to h.

This model may serve as a guideline for how to interpret and design indentation experiments on complex samples. For example, when performing measurements on cells on a glass petri dish, you may minimize the substrate effects by minimizing α, such as by not indenting deep or choosing a tip with a small contact radius. If performing an indentation experiment of cells on a very soft matrix or hydrogel, the substrate effects will need to be taken into account, otherwise the force-indentation response received from indenting on the cell may actually be more representative of the underlying soft substrate. If the parameter of interest in the experiment is the substrate (bottom layer) elasticity, then the probe of choice should depend on the elastic mismatch – for a softer bottom layer, a probe with larger contact radius will give a stronger signal, however for a stiffer bottom layer, the errors propagate very poorly, however a probe with small contact radius could penetrate through to the stiff bottom with very low effects from the two-layer model, which is an approach that will be detailed further in §6.

5 CORRELATING CONFOCAL MICROSCOPY AND AFM INDENTATION REVEALS METASTATIC CANCER CELLS STIFFEN DURING INVASION INTO COLLAGEN I MATRICES

This chapter details experiments regarding AFM indentations on MDA-MB-231 cells as they invade into bovine collagen I matrices. This is an adaptation of a manuscript that has been submitted for publication, "Correlating confocal microscopy and atomic force indentation reveals metastatic cancer cells stiffen during invasion into collagen I matrices" by Jack Rory Staunton (JRS), Bryant L. Doss (BLD), Stuart Lindsay (SL), and Robert Ros (RR). The experiments were conducted by JRS and BLD. Cell culture was performed by BLD, also acknowledging cell culture support from Nethmi Ariyasinghe and Mark Linhart. The lab protocol for producing bovine collagen I gels and seeding cells for invasion was developed by JRS. Finite element modeling was performed by BLD. Development of analytical tools was performed by BLD (as in §4). Data was analyzed by BLD and JRS. The manuscript was written by JRS, BLD, SL, and RR. RR and SL conceived and RR designed the experiments. We acknowledge the LeRoy Eyring Center for Solid State Science at Arizona State University for assistance with electron microscopy. This work was supported by a grant from the National Cancer Institute (U54CA143862).

Introduction

As detailed in §2, cells obtain a drastically different phenotype when cultured in 3D environments compared to 2D substrates. Cell migration is a key function in cancer

metastasis. Cancer cells have been shown to be able to use multiple modes of motility depending on the local properties of the microenvironment.

MDA-MB-231 metastatic breast cancer cells are widely studied as a model system for cancer cell invasion into ECM-like materials. Chavrier *et. al.* observe MDA-MB-231 cells invade into Matrigel in a rounded morphology relying on actin contractility to deform the matrix, and actomyosin or β_1 integrin inhibitors will reduce invasion[140]. Using 3D traction force microscopy, Koch *et. al.* observed that MDA-MB-231 exhibit larger contractility and higher local strain energy in a collagen matrix than their healthy counterparts, develop a more spindle-like morphology, and invade more efficiently than MCF-7 cells[141]. Kamm *et. al.* demonstrated with mitochondria-tracking microrheology that MDA-MB-231 cells exhibit more solid-like behavior in 3D compared to 2D[116]. Reinhart-King *et. al.* show that MDA-MB-231 cells form "tracks" in a collagen gel that will allow for migration of non-invasive MCF-10A cells and that its motility is dependent on a combination of ROCK activity, MMP activity, and collagen concentration[142]. These cells have also been shown to have a higher invasion speed in collagen networks that have been isotropically prealigned[143]. As such, actomyosin activity via Rho/ROCK pathways have been closely linked to MDA-MB-231 motility and inhibition of these pathways lead to suppressed invasion in randomly aligned collagen gels but not prealigned gels[144] and *in vivo*[145].

Despite these advances in imaging cells in 3D environments, direct mechanical measurements of cells in a 3D environment are rare (there are several techniques for this discussed in §3). Petrie *et. al.* recently demonstrated that invasive cells have distinct intracellular pressure differences in the leading and retracting edges of cells undergoing

lobopodial migration in 3D and showed that these are much higher than the 2D case[37]. To our knowledge, AFM has not been used to study the local mechanical properties and response to external deformation of cells in 3D environments. Here, we present a framework for quantitatively determining the apparent Young's modulus of cells invading into bovine collagen I matrices. Included in this framework are analytical tools such as an updated tip geometry models and solutions to the 2-layer problem (discussed in §4). Finite element simulations and confocal laser scanning microscopy are used to aid in the quantitative analysis and deconvolution of the collagen response from the cell response. Using these, we perform AFM force-indentation experiments to demonstrate a significant stiffening of cells as they begin to invade into 3D collagen matrices, and also study the effects of environments with different stiffnesses as well as inhibition of ROCK on the force response.

Materials and Methods

Collagen preparation

Thin (~100 μm) layers of bovine collagen I (Nutragen, Advanced Biomatrix) were polymerized on functionalized glass bottom petri dishes (World Precision Instruments). Glass was activated using a procedure similar to that shown by Pelham and Wang[146]. First, glass was ultrasonicated in ethanol and Millipore water for 10 minutes each, then dried with N_2. Following this, the glass was plasma cleaned (Harrick Plasma) using O_2 gas for 5 minutes. Surfaces were then incubated in room temperature in 1% (3-Aminopropyl)triethoxysilane in ethanol for 30 minutes, washed with ethanol and Millipore water, incubated in room temperature in 0.5% glutaraldehyde in 1x DPBS for

60 minutes, washed several times with Millipore water, then dried vertically in a laminar flow cabinet. Collagen I stock solutions (6.1 $mg \cdot ml^{-1}$) were mixed on ice with 10x DPBS, 0.1 M NaOH, and Millipore water at a ratio of 32:4:3:1 to form a 4.88 mg/mL gel. To form 2.44 mg/mL gels, the collagen was diluted with water and the amount of NaOH was halved. 200 µL of the mixed solution was pipetted onto the glass and spread around the surface with the pipette tip. The collagen was incubated for 90 minutes at 37°C and 5% CO_2 in a humidified incubator. After 90 minutes, 37°C 1x DPBS was gently added to the collagen surfaces. Collagen was stained with 0.02 mg/mL Atto 465 NHS in DPBS for 30 minutes (stock solutions were suspended at 2 $mg \cdot ml^{-1}$ in DMSO), then washed several times in DPBS.

Cell Culture and Sample Preparation

MDA-MB-231 metastatic breast cancer cells (ATCC) were cultured at 37 °C and 5% CO_2 in 1× DMEM containing 4.5 $mg \cdot ml^{-1}$ D-glucose and L-glutamine supplemented with 10% FBS. During passaging, adherent cells were dislodged from the culture flasks using Cellstripper™. For cell samples with ROCK inhibition, the growth medium was supplemented with 10 µM Y-27632 at the time the cells were seeded on the surfaces (stock Y-27632 was solubilized in Millipore water at a concentration of 10 mM). Cells were seeded on top of fully polymerized collagen I gels or glass-bottom dishes measuring in complete growth medium and 6−96 hours before measuring. For experiments of cells in collagen, the cell membranes were stained immediately before measuring using 2.5 µg/ml CellMask™ Deep Red Plasma membrane stain in HBSS for 30 minutes (stock solutions were suspended at 1 mg/mL in DMSO), then washed several times with HBSS.

Cell measurements and staining were performed at 37°C in 1x HBSS containing $CaCl_2$ and $MgCl_2$. For experiments with ROCK inhibition, HBSS was supplemented with 10 µM Y-27632.

Atomic force microscopy and confocal fluorescence microscopy

The AFM and confocal fluorescence measurements were performed on a combined system consisting of an Asylum Research MFP-3D-BIO AFM and a Picoquant Microtime 200 confocal laser scanning microscope[88,147] as in §4. The objective used was an Olympus LUMFL60X microscope objective (water, 60x, 1.1 NA, 1.5mm WD), and two pulsed laser diodes (470nm, 640nm) were used for the excitation source with a dual-band dichroic (Chroma 467/638rpc). Confocal scans are taken in 60x60 µm areas at 256x256 pixels. Team Nanotec LRCH-750 AFM probes (k~0.15 N/m) were used as in Figure 5-1, and spring constants were determined using the thermal tuning method. The AFM tip was aligned in the confocal volume and confocal fluorescence images were scanned in lateral and axial planes. AFM data used for elasticity nanotomograms was recorded by collecting force-indentation curves along a 40 µm line with one curve every 2 µm in the plane perpendicular to the cantilever direction. The approach and retraction velocity was ~3 µm/s in open-loop mode and the trigger force ranged from 15−35 nN. For cells plated on glass, each cell is indented 4 times in force-volume mode over a 4 μm^2 area in the central nuclear region.

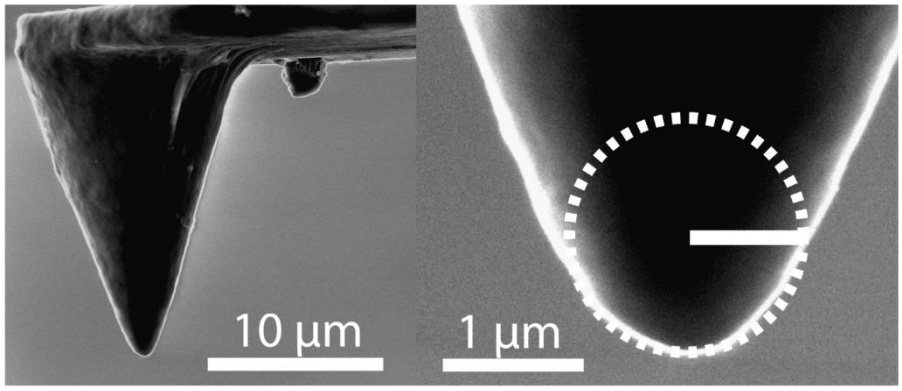

Figure 5-1: Scanning electron microscope image of an LRCH-750 tip after the indentation experiments. The pictured tip has a measured half-angle of 18.8°, apex radius of 695 nm, and tip height ~15 µm. Image was taken with an XL30 ESEM-FEG at the LeRoy Eying Center.

Finite element analysis

Finite element analysis was performed using ANSYS Workbench 14.0 as in §4 unless otherwise indicated. The cell was modeled as a spherical inclusion bonded to the collagen with a different Young's modulus but otherwise similar material properties. The tip had a triangular mesh size of 50 nm and the contact between the tip and sample was assumed to be frictionless. The cell and collagen mesh had an element length of 500 nm (unless otherwise noted) within 20 µm from the tip, which then tapered up to 1 µm. The Poisson ratios of the cell and the collagen were set to 0.45.

Data analysis

Data analysis was performed using MATLAB. Contact points are determined using an automated method unless otherwise noted (see rotation_minimum.m, Appendix D). Mann-Whitney U testing is performed with the built-in ranksum command in MATLAB (two-sided, approximate for large n). Boxplots are produced using MATLAB

built-in function with whisker lengths 1.5 times the interquartile range. ANOVA testing is performed using MATLAB function anovan. Images are exported from PicoQuant SymphoTime measuring software and merged using ImageJ. Plots are generated in MATLAB and annotations and color adjustments are made in Inkscape and Adobe Illustrator.

Cells and collagen were assumed to be incompressible at the length scale of AFM indentation (ν_{cell}=$\nu_{collagen}$=0.5)[148], however experiments performed on both bulk ECM demonstrate $\nu_{collagen}$>0.5 presumably due to water flux[21] thus some systematic errors may arise from this choice. AFM force-indentation curves are fit assuming a sphero-conical tip geometry (Eqs. (5-1)-(5-5), see Appendix A for derivation). The fitting procedure is the linearized method introduced in §3, and unless otherwise noted, the indentation depths used for fitting is fixed to 0.25-2.50 μm.

To determine the Young's modulus of partially embedded cells, the two-layer deconvolution technique is applied. The average pericellular collagen (bottom layer) Young's modulus (E_2) is determined using Eqs. (5-1)-(5-5) for each cell (from 3 curves and distance 4−12 μm from the cell on each side if available) and the cell (top layer) height h is estimated from the axial confocal fluorescence micrograph recorded before the indentations. The average apparent Young's modulus of the cell determined using Eqs. (5-1)-(5-5) from a set of 3-4 experimental force-indentation curves from the highest part of the cell's apical surface. The cell Young's modulus is then corrected by multiplying by the correction factor determined for the tip shape, indentation depth, and cell height (shown in Figure 5-3E). To determine the Young's modulus of cells on glass,

the force-indentation data is fit using Eqs. (5-1)-(5-5) and the result is averaged over 4 curves per cell.

To determine the Young's modulus of fully embedded cells, a single experimental force-indentation curve over the highest part of the cell's central region is used. The curve over the cell is fit using Eqs. (5-1)-(5-5) piecewise in 250 nm intervals to calculate the depth-dependent apparent Young's modulus. Finite element models are generated - the invasion depth and diameter of the cell is estimated from the axial confocal micrograph, and the Young's modulus of the collagen is determined from force-indentation curves of pericellular collagen in the same way as partially embedded cells. The cell's Young's modulus is initially guessed based on the experimental data, and an indentation by a rigid (~GPa) probe with geometry similar to that of the experimentally used AFM probe is then simulated using finite element analysis, producing a simulated force-indentation curve. The simulated curve is fitted in an identical manner to the experimental curve and the results are compared. Simulations are repeated using subsequent finite element models models in which the depth of the cell is adjusted by hand in 0.25 μm increments and the Young's modulus of the cell is adjusted by hand in 0.1 kPa increments until the experimental and simulated depth-dependent apparent Young's modulus differ minimally.

Results

Spatially correlated AFM indentation and confocal laser scanning fluorescence

To determine the Young's moduli of single cells embedded in hydrogels, we use a combined AFM and confocal fluorescence microscope setup (Figure 5-2A). The

alignment of the AFM tip with the laser focus allows precise determination of the location of the indentation in the confocal scans. MDA-MB-231 breast cancer cells were seeded on top of bovine collagen I matrices and subsequently measured after times ranging 6−96 hr, during which time a majority of cells invaded the collagen either partially or fully. 2D confocal scans are conducted in lateral (Figure 5-2B) and axial (Figure 5-2C) planes. AFM indentations with large sphero-conical tips were then conducted in the axial plane to generate spatially co-registered elasticity nanotomograms (Figure 5-2D) using force-indentation data and piecewise apparent Young's modulus on

the collagen (Figure 5-2E) and cellular (Figure 5-2F) regions. The tomogram shows a clear mechanical contrast between the cell and the gel.

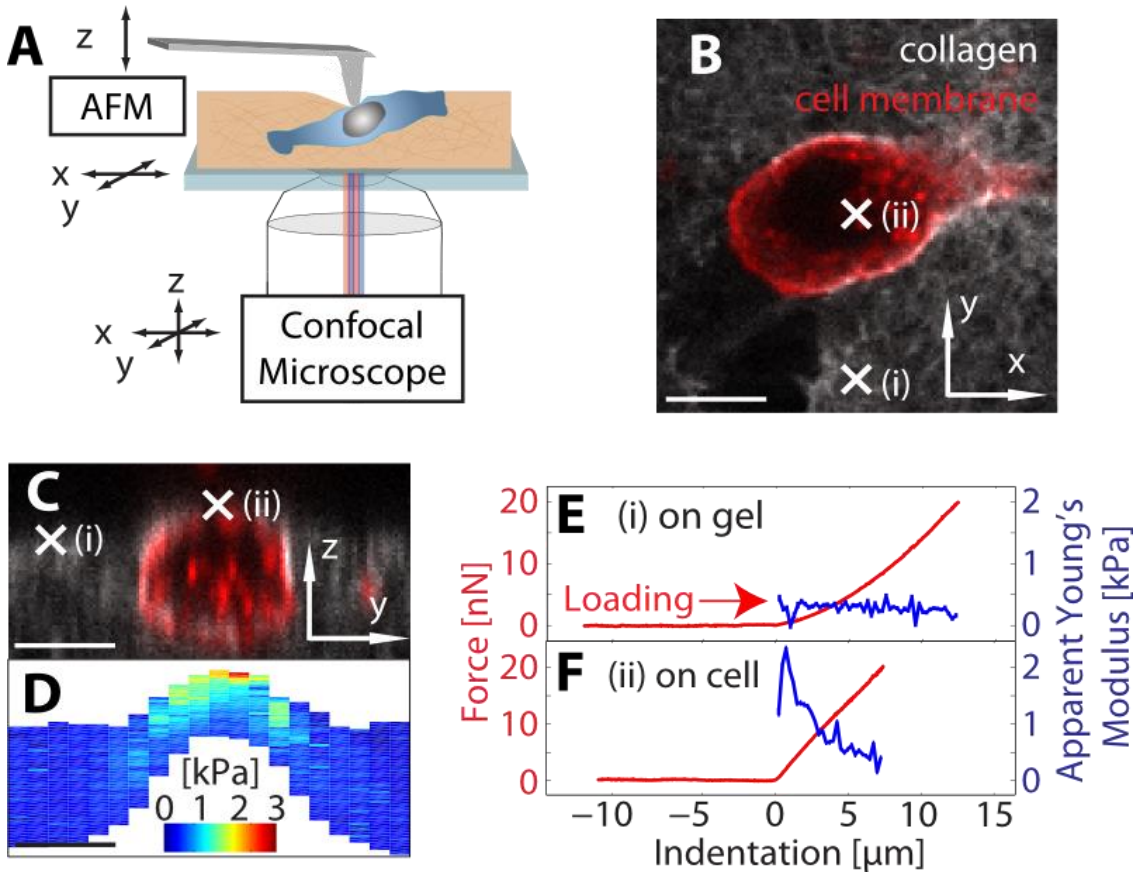

Figure 5-2: Overview image of the combined AFM indentation with confocal fluorescence microscopy for indenting cells partially embedded in collagen. (A) Schematic of the AFM and confocal microscopy setup. The microscopy objective scans in all three dimensions, the AFM sample stage scans in X and Y, and the cantilever moves in the Z direction. The AFM probe and laser from the confocal microscope are aligned. (B) Lateral and (C) axial confocal fluorescence images of an MDA-MB-231 cell in collagen I. The cell membrane and collagen are fluorescently labeled as described in Methods. (D) Elasticity nanotomogram from fitting data of all force-indentation curves along the lateral confocal image in (C). (E), (F) Force-indentation curves and respective depth-dependent apparent Young's modulus fits for data collected on collagen and the cell, respectively. Scale bars: 10 µm.

Elastic modulus determination of heterogeneous samples

To determine the Young's modulus from indentations using the AFM tips with large apex radius, we derived an elastic contact model for a sphero-conical tip using Sneddon's procedure[80] that contains a sphere of radius *R* which smoothly transitions into a cone with half angle θ (see Figure A-1, and Appendix A for full derivation) and also solve the two-layer equations in §4 (Figure 5-3A). The resulting equations are:

$$b = R\cos\theta \tag{5-1}$$

$$\delta(a \le b) = \frac{1}{2}a\ln\left(\frac{R+a}{R-a}\right) \tag{5-2}$$

$$\delta(a > b) = a\ln\left(\frac{R+a}{\sqrt{R^2-b^2}+\sqrt{a^2-b^2}}\right) + a\cos^{-1}\left(\frac{b}{a}\right)\cot\theta \tag{5-3}$$

$$F(a \le b) = \frac{E}{(1-\nu^2)}\left[\frac{1}{2}(a^2+R^2)\ln\left(\frac{R+a}{R-a}\right) - aR\right] \tag{5-4}$$

$$\begin{aligned} F(a > b) = \frac{E}{(1-\nu^2)}\Bigg[& a^2\cot\theta\cos^{-1}\left(\frac{b}{a}\right) \\ & + b\cot\theta\sqrt{a^2-b^2} - aR + \sqrt{(R^2-b^2)(a^2-b^2)} \\ & + a^2\ln\left(\frac{R+a}{\sqrt{R^2-b^2}+\sqrt{a^2-b^2}}\right) \\ & - \frac{R^2}{2}\ln\left(\frac{a^2R^2 - \left(b^2 - \sqrt{(R^2-b^2)(a^2-b^2)}\right)^2}{b^2(R+a)^2}\right)\Bigg] \end{aligned} \tag{5-5}$$

The sphero-conical model is similar to the blunted cone developed by Briscoe[85] shown in Eqs. (3-22)-(3-25). The sphere-conical tip geometry does not follow exact a power-law, but is approximated and fit using least-squares as one for a given indentation depth (for example in SI units, when R=695E-9, θ=18.8°, δ ranges from 0.25E-6 to 2.50E-6, then

A=1.289E-4, B=1.357 with r^2=0.9996). To test the validity of this model, we performed finite element simulations with a modeled sphero-conical tip to determine if using these equations to fit the force-indentation data will reproduce the imposed Young's modulus in the simulation. Figure 5-3B shows the sphero-conical model's accuracy in fitting finite element simulations compared to the Hertz and Sneddon models, where the sphero-conical model accurately computes the value of the imposed modulus for both deep and shallow indentations (with the exception of some numeric dips due to meshing). Accuracies of the sphero-conical model, along with r^2 values, are shown in Table 5-1. As in §4, the effects of the substrate in the force-indentation response are corrected for and demonstrated using finite element simulations in Figure 5-3C, D. For practical use of the two-layer model, a table of correction values are calculated for the tip used in the experiment to very quickly compute the substrate-corrected Young's modulus, as shown in Figure 5-3E. When knowledge of the substrate (collagen) elastic modulus and cell height are known, the apparent modulus from the curve on cell is simply multiplied by a small factor interpolated from the table. For all of the untreated cells analyzed in this work, only a fraction (<10%) have correction factors that are larger than 15% which is an often cited error in AFM cantilever calibration.

As noted in §4, this two-layer correction generally only holds for indentation depths which are smaller than the layer height, and is generally only valid for $\delta<h$. For indentations beyond the first layer, other techniques such as finite element analysis are required to study asymptotic behavior.

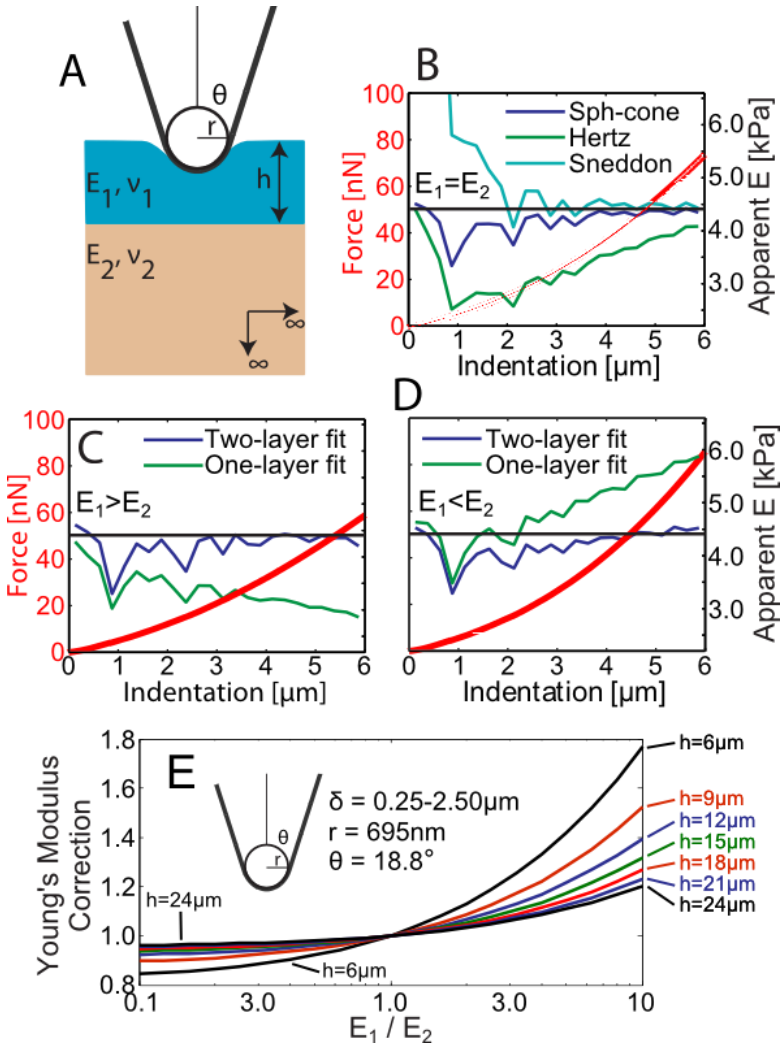

Figure 5-3: Schematic and demonstration of the fitting methods developed for this work. (A) Illustration depicting a sphero-conical tip indenting into a bonded two-layer elastic half-space. (B) Force-indentation curve of a sphero-conical tip (R=750nm, θ=22.5°) indenting into a homogeneous elastic half-space (E_1=E_2=4.4 kPa, ν_1= ν_2=0.47, displayed in black, right axis) generated with finite element analysis (red, left axis) and the corresponding piecewise depth-dependent fits using the sphero-conical model (blue, right axis), Hertz model (green), and Sneddon model (purple). (C) Force-indentation curve from finite element analysis (red) and piecewise depth-dependent fits for the Young's modulus using the sphero-conical model with (blue) and without (green) substrate correction and the imposed modulus of the top layer (black). For this simulation, h=10 μm, E_1=4.4 kPa, ν_1=0.47, E_2=1.5 kPa, ν_2=0.49. (D) Similar to (C) with h=10 μm, E_1=4.4 kPa, ν_1=0.47, E_2=14.4 kPa, ν_2=0.44. (E) Young's modulus correction values calculated for the cell experiments using a sphero-conical tip with radius 695nm, θ=18.8°, indentations 0.25-2.50 μm for various layer heights and apparent layer mismatches (in this case, E_1 is the apparent modulus from fitting the top layer without correction and E_2 and h are independently measured experimental values).

	Linearized Fit		Least Squares Fit	
	0.25-2.50 μm	**1.00-5.00 μm**	**0.25-2.50 μm**	**1.00-5.00 μm**
Hertz	-37.6%, 0.9964	-31.3%, 0.9992	-29.2%, 0.9941	-31.3%, 0.9994
Sneddon	+51.9%, 0.9145	+12.5%, 0.9408	+153.8%, 0.9381	+75.1%, 0.9612
Sphero-conical	-10.0%, 0.9986	+0.9%, 0.9988	-6.7%, 0.9994	-4.1%, 0.9997

Table 5-1: Errors in the apparent calculated Young's modulus from the imposed simulation Young's modulus and r^2 values from fitting the finite element simulated curve using linearized (used in this work) and least squares routines, along different indentation intervals, and with different tip geometry models. There are no contact point errors due as it is exactly known. The simulated tip is sphero-conical with R=695 nm, θ=18.8° and the mesh size of the sample is 500 nm. The sample is very large (height, width 100 μm) and is flat, homogeneous, elastic, and isotropic.

Cells display significant stiffening during initial invasion into collagen

MDA-MB-231 breast cancer cells were seeded on top of fully polymerized bovine collagen I matrices with Young's moduli ranging 0.1−6 kPa (Figure 5-4). While collagen I gels are very porous, the raw force-indentation data on collagen using a probe with radius 695nm is readily fit by the models derived for this work with high r^2 (Figure 5-5). In some gels, it is observed that there is a stiffer top layer and then a softer underlying collagen layer (Figure 5-5C, D), presumably due to humidity changes during polymerization. Finite element simulations of indentations of elastic materials with varying element mesh sizes show negligible artifacts when it is similar to or less than the probe radius (Figure 5-6).

To quantify a cell's embeddedness, we define the "Degree of Invasion" (DoI) as the height difference between the collagen and apical cell surfaces (determined from the contact points of the force-indentation curves) divided by the cell height (determined

from confocal microscopy) and subtracted from one (Figure 5-8). After some time, the cells began to invade into the collagen gels, however no differences were seen in the stiffness or partial embeddedness of cells as a function of time (Figure 5-7), however cells more readily invaded into softer collagen gels (Figure 5-8B). For partially embedded cells, force-indentation curves on pericellular collagen are fitted to approximate the Young's modulus of the collagen underneath the cell and the height of the cells from confocal microscopy are used to determine the correction of the Young's modulus from curves on cells (Figure 5-3E). Figure 5-8C shows the apparent Young's moduli of partially embedded cells as a function of the invasion depth, binned into three similarly populated groups. Cells 0−50% embedded (DoI<0.50) had Young's modulus of 0.74±0.29 kPa (median ± median absolute deviation for all unless otherwise noted), similar to the observed moduli of cells on glass (p=0.61, Mann-Whitney U test for all p values). Cells 50−75% embedded (0.50<DoI<0.75) had median Young's modulus of 0.99±0.38kPa, significantly stiffer (34%, p=0.018) than cells 0−50% embedded. Cells 75−100% embedded (DoI>0.75) had median Young's modulus of 1.34±0.49 kPa, significantly stiffer again (35%, p=0.039) than cells 50−75% embedded.

In some invading cells, we observed bright fluorescence from the collagen directly around the cell, indicating the cell has remodeling the collagen by displacement (Figure 5-9A). During the measurements and analysis, it is assumed the local collagen stiffness is uniform, however this is not necessarily true and is not detectable underneath the cell with AFM. To address the possibility that the stiffening is due merely to the support from the surrounds matrix, we used finite element analysis to simulate indentations into model systems of a round elastic cell embedded in an elastic gel with

some additional collagen "shell" (Figure 5-9B) and analyzed the simulation data using the same procedure as experimental data. As the simulated cell is displaced into the matrix and the collagen shell is assumed equal to collagen, a small amount apparent cell stiffening is observed (~6% for DoI=0.50 to 0.93, Figure 5-9C). If the collagen shell is assumed to be much more rigid than the surrounding collagen (up to 8 times), additional slight stiffening is also observed (~3% for E_{shell}=0.75 kPa to 6.00 kPa, Figure 5-9D). The amount of stiffening due to varying geometric constraints is much less than observed experimentally and well within cantilever calibration errors[79]. Because the artifacts quantified with finite element analysis are much smaller than the amount of stiffening observed experimentally, the cell stiffening is a change in phenotype in response to activity in the 3D environment.

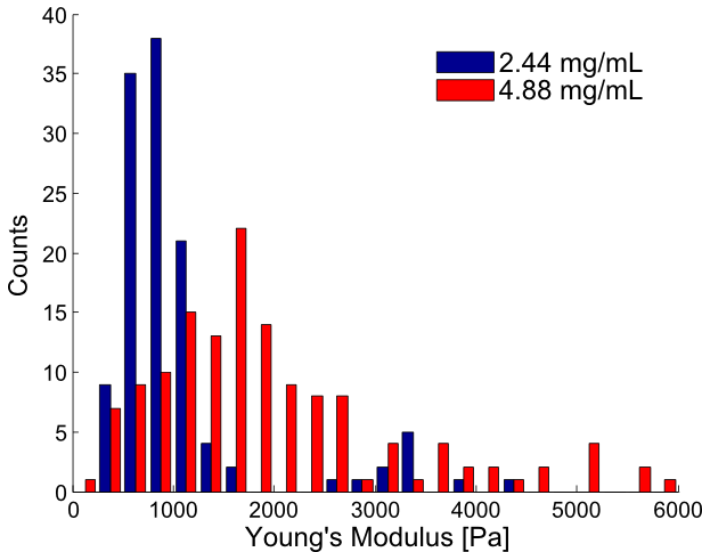

Figure 5-4: Histograms of Young's moduli of pericellular bovine collagen I from hydrogels formed at different initial collagen concentrations.

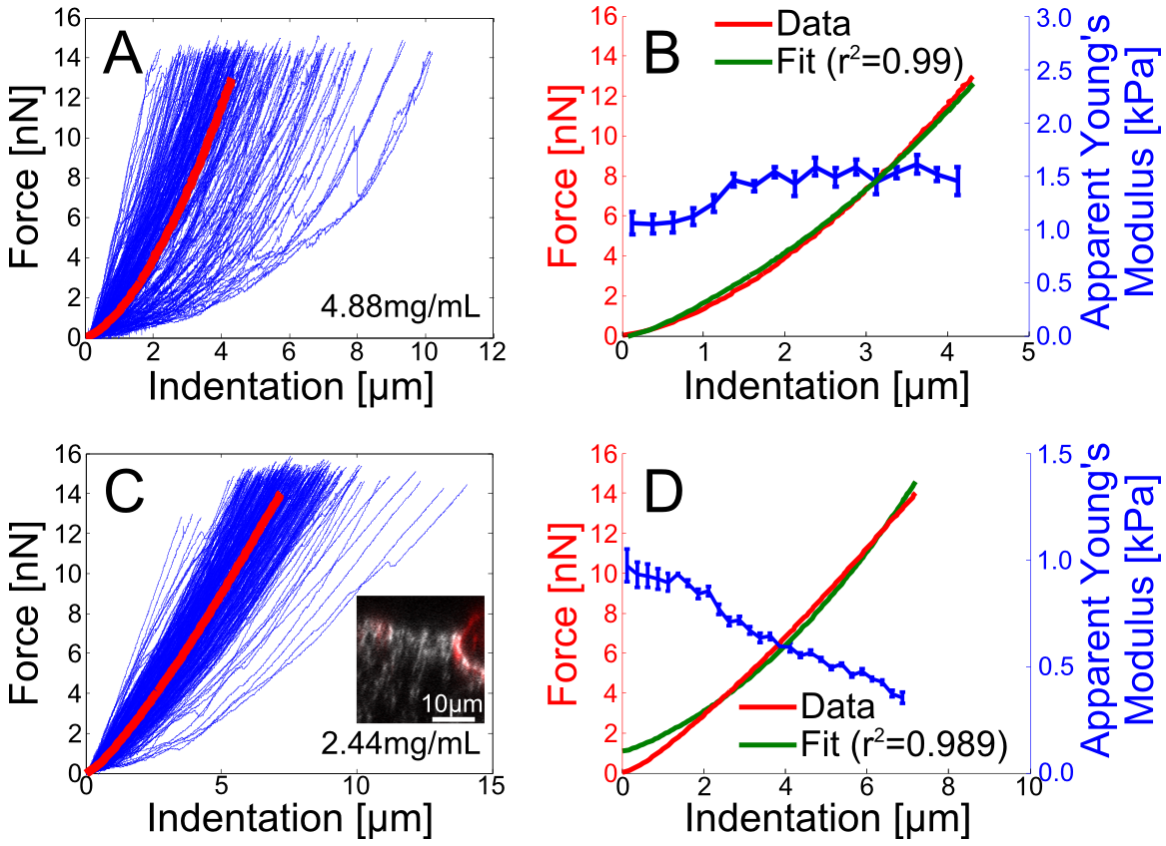

Figure 5-5: Force-indentation values and fits of bovine collagen I. (A) (blue) Force-indentation curves on collagen (4.88 mg/mL) from an experiment aligned at the contact point, and (red) the average force-indentation curve using the mean indentation at 0.1 nN force intervals (method 2 from[149]). (B) The average force-indentation curve (red, right axis) from (A) fit using the methods in this paper along the entire curve (green, right axis) and the resulting Young's modulus shown from fitting along 250 nm indentation intervals (blue, right axis, error bars show error in regression method from the single average curve). (C, D) same as (A, B) but for 2.44 mg/mL collagen. Inset in (C) shows a YZ confocal image from 2.44 mg/mL collagen, showing some mechanical heterogeneity in the collagen gel where it appears brighter and stiffer in (D) at the top boundary of the gel and softer inside of the gel.

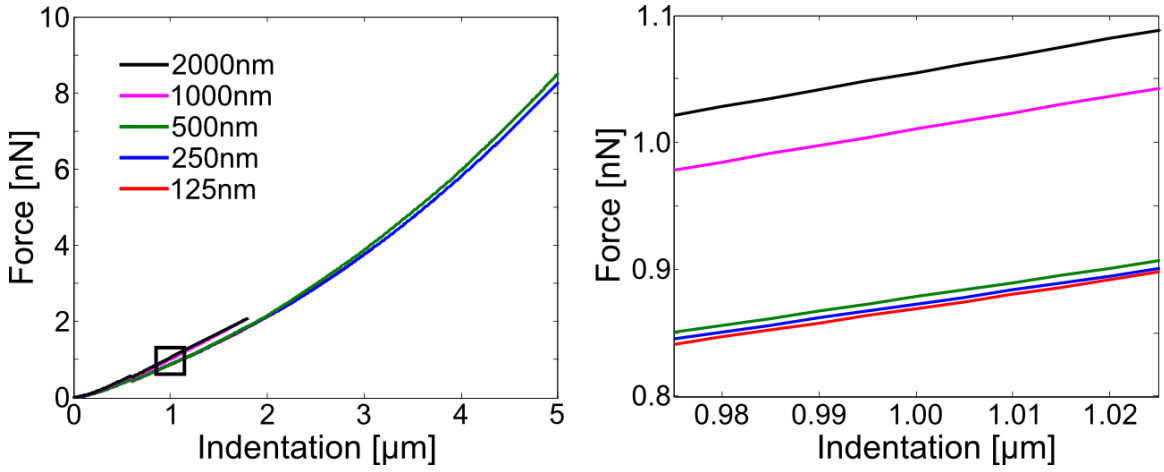

Figure 5-6: Effect of the mesh size on finite element simulations. The indenting probe is sphero-conical with R=695 nm and θ=18.8° and the sample is flat. The right image shows a zoom-in on the black square in the left image. For mesh sizes less than the probe radius, neglible errors are seen.

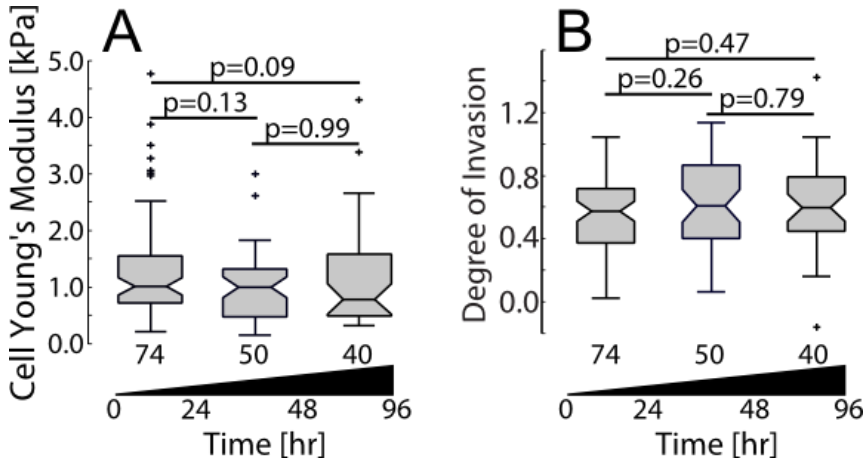

Figure 5-7: Effect of time in stiffness and degree of invasion of MDA-MB-231 cells in collagen I. (A) Stiffness and (B) degree of invasion of partially invaded MDA-MB-231 seeded on collagen I matrixes at various time points. From left to right, $t \leq 24$ hr (n=74), 24 hr$<t \leq$ 48 hr (n=50), and t>48 hr (n=40).

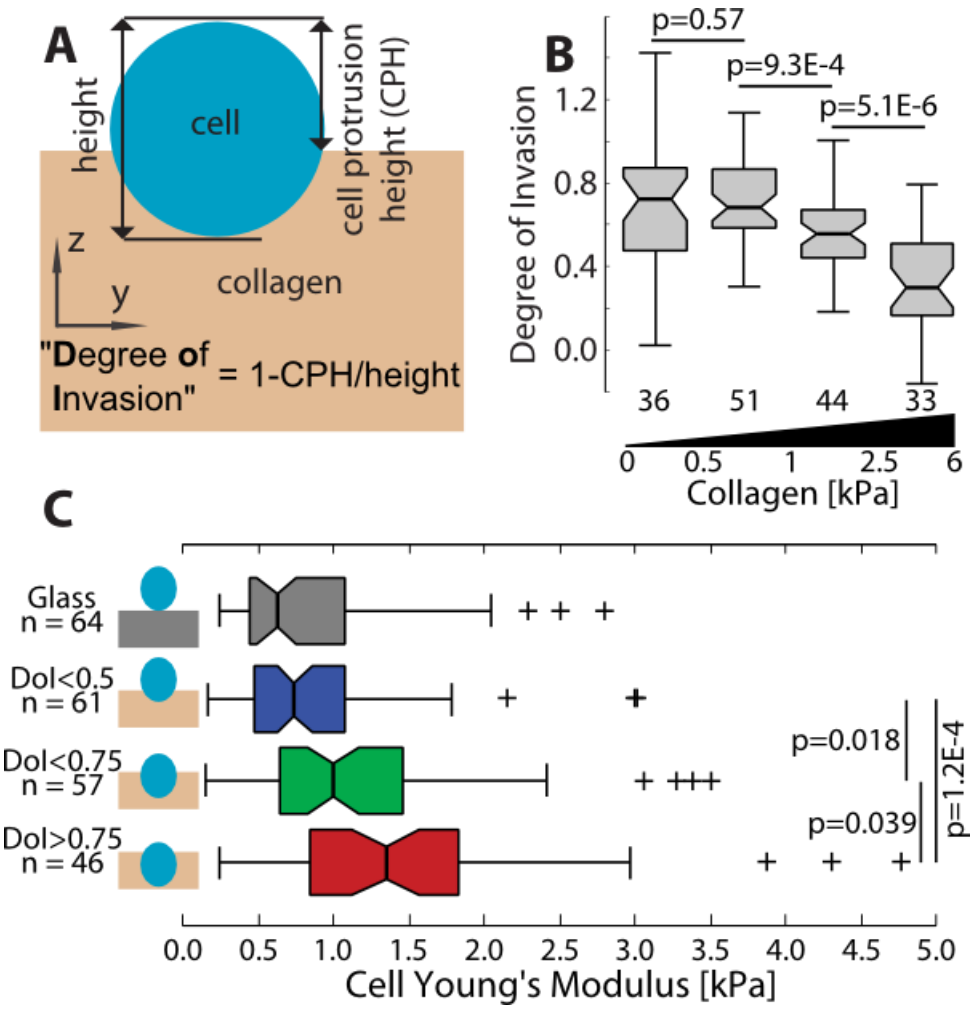

Figure 5-8: Young's moduli of MDA-MB-231 cells on glass and partially embedded in collagen I hydrogels. (A) Schematic defining the degree of invasion (DoI) quantifying the amount of cell embedding. (B) Box plot showing the DoI for different stiffness bins of collagen I gels, number of replicates are shown underneath. (C) Box plot showing the corrected cell Young's modulus at various stages of partial invasion. P-values are calculated using the Mann-Whitney U test.

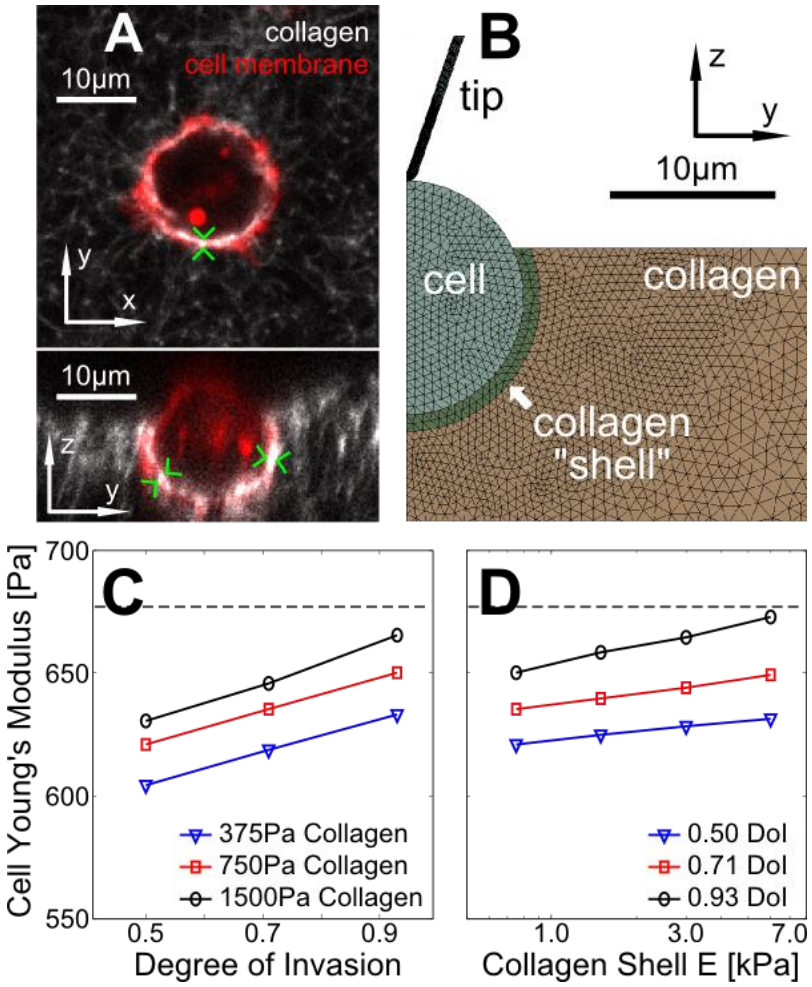

Figure 5-9: Finite element modeling of AFM force-indentation curves on cells partially embedded in ECM. (A) XY and YZ confocal fluorescence images of a partially embedded cell. Green arrows indicate some observed collagen remodeling and high intensity around the cell. (B) Finite element model of a partially embedded cell with a collagen "shell" for collagen displaced by the cell (here, R=695 nm, θ=18.8°, DoI=0.93, cell diameter=14 μm, E_{cell}=0.75 kPa, $E_{collagen}$=E_{shell} for the colored lines). (C) Corrected cell Young's modulus versus degree of invasion for different collagen Young's moduli; at most, 6% stiffening is observed between DoI=0.5 and DoI=0.93 for these parameters. Dashed line represents apparent Young's modulus from flat substrate with E=0.75 kPa, which is lower due to meshing artifacts. (D) Cell Young's modulus versus collagen shell stiffness (collagen shell thickness=1μm, E_{cell}=$E_{collagen}$=0.75 kPa, no correction is used); stiffening is slightly more pronounced in more deeply embedded cells, but is 3% at most.

ANOVA testing revealed the two strongest predictors for cell stiffness were the degree of invasion and the local collagen stiffness, compared with the time after seeding, collagen concentration, and cell heights (however, time was shown to have some effect, but we could not directly find a correlation -- we believe this may be because more time allows cells to invade into stiffer collagen gels). We then binned the data by both the cells' invasion depth and local collagen stiffness (Figure 5-10C). On soft collagen ($E_{col.}$<1 kPa), cells 50−100% embedded (DoI>0.5) were significantly stiffer (58% increase in median, p=1.1E-3, all values are shown in Table 1) than cells 0−50% embedded (DoI<0.5). On stiff collagen ($E_{col.}$>1 kPa), cells 50−100% embedded were 60% stiffer (p=3.9E-3) than cells 0−50% embedded. For both DoI ranges, the cell and gel stiffness correlate.

Rho/ROCK is responsible for some observed stiffening

As discussed in §2, the Rho GTPase is heavily implicated in cell motility in 3D, and is responsible for actomyosin contraction. Several studies of MDA-MB-231 cells in 3D demonstrate that invasion may be inhibited by blocking Rho/ROCK activity[140,144,145]. We hypothesized the stiffening may be due to increased actomyosin contractility resulting in a more rigid cytoskeleton.

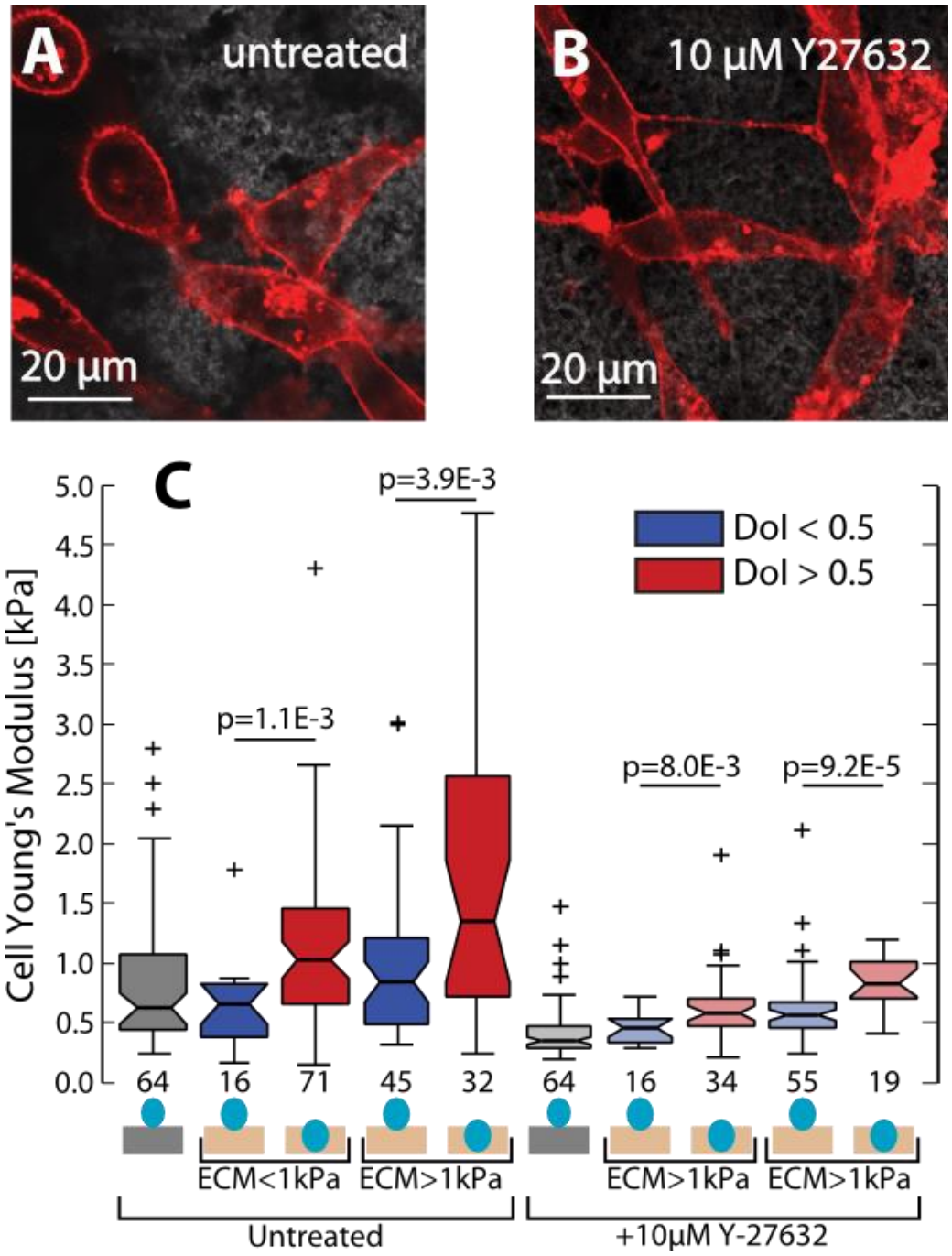

Figure 5-10: Young's moduli of partially embedded cells is ROCK dependent. (A, B) Lateral confocal fluorescence image of cells (A) untreated and (B) treated with 10 µM Y-27632. (C) Box plots of Young's moduli of cells (number of replicates are shown underneath) of untreated and treated with 10 µM Y-27632 on glass and partially embedded in collagen, binned by both DoI and pericellular collagen stiffness. All Young's moduli are determined by fitting the indentation from 0.25−2.5 µm and corrected to account for the influence of the collagen substrate. P-values are calculated using the Mann-Whitney U test.

We repeated the measurements on cells treated with Y-27632, a ROCK inhibitor. ROCK inhibited cells obtained an elongated morphology, indicating the inability to contract actomyosin filaments (Figure 5-10B, compared to Figure 5-10A). ROCK inhibition significantly reduced the Young's moduli of cells on glass (51%, p=2.39 E-7); cells embedded 0-50% on soft collagen (31%, p=0.10) and stiff collagen (33%, p=3.6E-3); and cells embedded 50-100% on soft collagen (43%, p=2.6E-5) and stiff collagen (39%, p=0.02) (Figure 5-10C). On soft collagen, 50−100% embedded cells were 30% stiffer (compared to 58%) than 0−50% embedded cells (p=8.0E-3), and on stiff collagen, 50−100% embedded cells were only 47% (compared to 60%) stiffer than 0−50% embedded cells. (p=9.2E-5). This demonstrates that ROCK-mediated contractility may be vital for the cell stiffening during invasion which we observed.

Cells fully embedded in collagen display similar stiffening

To determine the Young's modulus of cells fully embedded in collagen (Figure 5-12A), simulations of indentations were performed using finite element models (Figure 5-12,C-E) with geometry determined from the axial confocal micrographs. Each cell's position and imposed Young's modulus were iteratively adjusted until the simulated force-indentation curve resulted in a depth-dependent apparent Young's modulus that differed minimally from the depth-dependent apparent Young's modulus fit from the experimental force-indentation curve, as illustrated in Figure 5-12,D-G. Only cells at invasion depths ≤3.5μm could be analyzed using this method due to the decreased mechanical contrast observed (Figure 5-11). 13 cells were analyzed with this approach

(despite 64 total cells being measured, only 13 could be quantified); with 3 stiff (>10kPa) outliers omitted, the median Young's modulus was 1.5±0.4 kPa (Figure 5-13). This is much stiffer than cells which have not begun to invade and is similar to those that have nearly fully embedded into the collagen gels.

However, we note that the finite element models are very simplified versions of the physical system, which will contain remodeled or spatially heterogeneous collagen, non-spherical cells, and general experimental noise, thus small deviations between the experimental and simulated data is not unexpected, however good agreement between the two are seen.

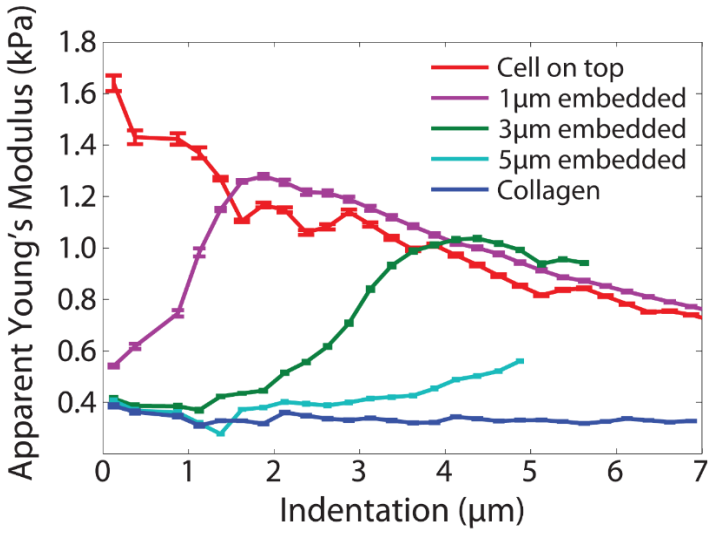

Figure 5-11: Demonstration of mechanical contrast from finite element simulations of embedded cells. The tip is modeled as sphero-conical with apex radius 745 nm and half-angle 18.81°, the cell Young's modulus is 2.0 kPa, the collagen Young's modulus is 0.3 kPa (Poisson ratio for both is 0.45), and the radius of the cell is 6.5 μm. As the cell is moved from on top of the collagen gel with 1 μm protrusion (red) to 5 μm embedded (teal), both the maximum value of the depth-dependent apparent Young's modulus and the slope of the transition decreases with increased invasion depth. This effect is referred to as mechanical contrast, and this contrast is lost as the cell becomes too deeply embedded or the Young's modulus of the cell and collagen become too similar.

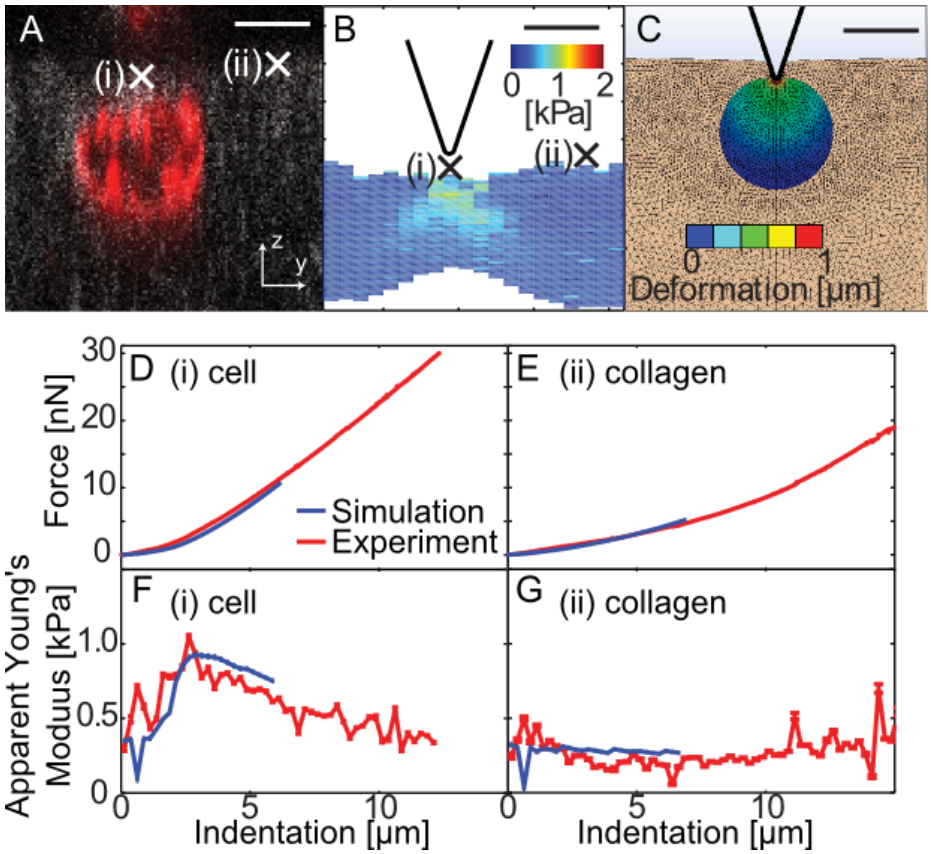

Figure 5-12: Determination of the Young's modulus of MDA-MB-231 cells fully embedded in collagen. (A) Axial confocal fluorescence micrograph of a cell that has fully invaded into collagen. (B) Elasticity nanotomogram of the cell, also showing the AFM probe size to scale. (C) Axisymmetric finite element simulation of an indentation on a fully embedded cell. Color scale represents the total deformation from a 3 μm indentation. Scale bars are 10 μm for all. (D, E) Experimental (red) and simulated (blue) force-indentation curves from points (I, on the cell) and (ii, on the collagen). (F, G) Apparent Young's modulus calculated from the experimental (red) and simulated (blue) force-indentation curves shown above.

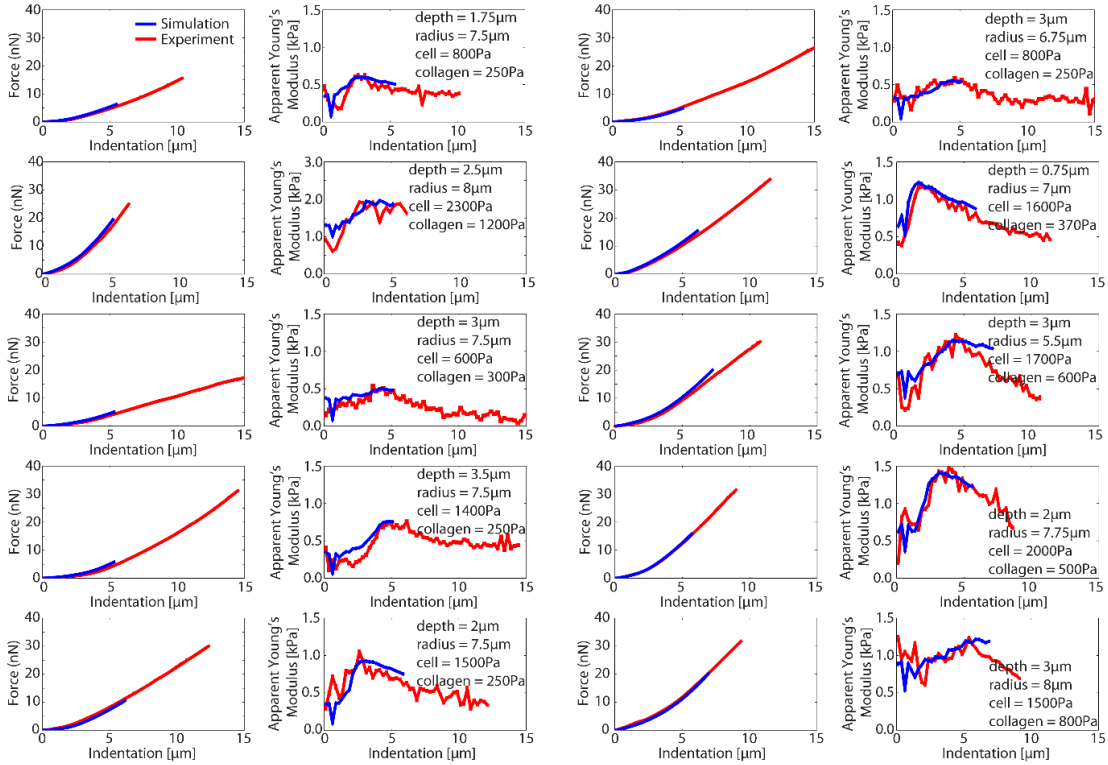

Figure 5-13: Ten fully embedded cells with the experimental force-indentation curves and depth-dependent fits (red) overlayed with the finite element simulation (blue) from ANSYS. For each cell, the physical dimensions and elasticity parameters of the sample are given. The tip is sphero-conical with the same geometry as in the experiment. The depth-dependent bin size is 250 nm and contact points are chosen manually.

	Substrate	Degree of Invasion (DoI)	Number of cells	Young's Modulus of the Cell [kPa]	
				(mean ± s.e.m.)	(median ± m.a.d.)
Untreated	Glass	0	64	0.86 ± 0.8	0.63 ± 0.27
	Col E<1 kPa	< 0.5	16	0.64 ± 0.10	0.65 ± 0.29
	Col E>1 kPa	< 0.5	45	0.97 ± 0.09	0.84 ± 0.37
	Col E<1 kPa	> 0.5	71	1.13 ± 0.08	1.03 ± 0.42
	Col E>1 kPa	> 0.5	32	1.70 ± 0.21	1.35 ± 0.68
	All	Fully Embedded	10	1.4 ± 0.2	1.5 ± 0.4
+ 10 µM Y-27632	Glass	0	64	0.43 ± 0.02	0.36 ± 0.08
	Col E<1 kPa	< 0.5	16	0.45 ± 0.03	0.45 ± 0.10
	Col E>1 kPa	< 0.5	55	0.62 ± 0.04	0.56 ± 0.11
	Col E<1 kPa	> 0.5	34	0.64 ± 0.05	0.58 ± 0.12
	Col E>1 kPa	> 0.5	19	0.84 ± 0.05	0.83 ± 0.17

Table 5-2: Young's moduli of MDA-MB-231 cells for different invasion depth, collagen stiffnesses, and treatments.

Discussion

The Young's moduli for all cells depending on collagen stiffness, degree of invasion, and presence of Y-27632 have been tabulated in Table 5-2 with the results for cells on glass and cells that have been fully embedded.

The behavior of single cells has been shown to be drastically different in 3D environments than on 2D surfaces (see §2 for more details), and it is also established that cancer cells may switch between different modes of motility. Recent work by Chavrier *et. al.* demonstrate that MDA-MB-231 cells invading into Matrigel do so in a rounded cell

mode by employing actomyosin contractility, and in order to generate force for forward propulsion there is observed contractility in the rear of the cell in actomyosin rich uropods[140]. Here, as our cells are invading vertically downward into collagen gels and cells use rear contraction, and AFM is probing the top (rear) of the invading cells, it is possible that this contributes to the observed stiffening thereby corroborating the rounded cell invasion model. Another related previous study by Petrie *et. al.* demonstrated that MDA-MB-231 cells have large intracellular pressure increases during lobopodial migration, and that the pressure is larger in the leading edge than trailing edge and both are larger than the case of cells on 2D substrates[37]. Our AFM experiments demonstrate a similar effect as the cells are stiffening during the initial stages of invasion, although it is assumed the trailing edge is being indented with AFM.

While AFM studies on cells grown on rigid 2D substrates has provided many novel and useful insights, extending the same types of measurements to cells in 3D systems is critical and little is known. The techniques presented here show the ability to deconvolute the mechanical response from heterogeneous elastic materials, despite large mismatches in elastic moduli and degrees of invasion of the cells the collagen. It was observed that cells significantly stiffen during invasion into collagen matrices, and this stiffening is enhanced on stiffer collagen gels and may be reduced by pharmacological inhibition of ROCK. As conventional wisdom gained from cells on 2D surfaces suggests that the highly deformable properties of cancer cells more readily allow invasion, our observed result demonstrates that this is not necessarily the case in 3D as the cells dramatically stiffen. The experimental and theoretical framework presented here may also be more generally applied to a wide range of soft matter elasticity problems with

some inclusion, including (but not limited to) studies of other cell types on or embedded in various types of ECM.

6 MECHANICAL PROPERTIES OF CANCER CELL NUCLEI *IN SITU*

This chapter details experiments regarding the mechanical properties of cancer cell nuclei *in situ*. This project was performed in close collaboration with Stuart Lindsay's (SL) lab (Subhadip Senapati, Brendan Sullivan) at Arizona State University. Nuclei are extracted from the cells by the Lindsay lab, and the cell lines were all acquired from the Lindsay lab. Experiments were performed by Bryant L. Doss (BLD) with assistance from Nethmi Ariyasinghe in the Robert Ros (RR) lab. Data was analyzed by BLD. This work was supported by a grant from the National Cancer Institute (U54CA143862) awarded to SL and RR.

Introduction

The study of nuclear mechanics has many applications, from stem cell differentiation and reprogramming[52,53,57] to limits in single cell motility in 3D environments (for a more detailed discussion, see §2).

The cell nucleus is central to understanding the transformation of healthy cells into cancerous cells. The nuclei of cancer cells have dramatic morphological changes from normal cell nuclei, such as changes in the size, geometry, and amount of heterochromatin aggregation[150]. Many of these shape alterations may contribute to abnormal gene expression as the access to certain genes by the transcriptional machinery is different.

Recently, direct measurements of nuclear mechanics have been performed using a variety of conditions and techniques. The role of chromatin compaction on nuclear

stiffness has been studied on isolated nuclei using micropipette aspiration and showed that nuclear swelling, chromatin decondensation, and increased deformability all occur under low concentrations of divalent cations[55]. Micropipette aspiration has also been used to study nuclear stiffness in differentiating stem cells and lamin-A deficient cells (here both condensed chromatin and lamin-A correlate positively with nuclear stiffness)[52]. Optical stretching has demonstrated nuclei with condensed chromatin are more rigid compared to less condensed chromatin and drug treatment with the histone deacetylase (HDAC) inhibitor trichostatin-A may decondense chromatin and soften nuclei[53].

AFM has recently been used to probe nuclear mechanics *in situ* by milling "nanoneedles" from AFM tips using a focused ion beam and correlating the force-indentation with 3D confocal fluorescence microscopy[151], where it was shown that metastatic T24 bladder cells have softer nuclei than healthy RT4 cells. Similar experiments on HT1080 fibrosarcoma cells have been performed by Wolf *et. al.* where different probe geometries and cantilever spring constants were used[152], where it was determined that there is an incompressible region of chromatin that may be probed by cantilevers with high spring constants and this region is compromised by treatment with HDAC inhibition. AFM has also been used to demonstrate negative Poisson's ratio in the nuclei of differentiating stem cells[57].

Much like whole cells, the mechanical properties and function of cell nuclei are heavily dependent on the environment of the nucleus. As nuclear mechanics is governed by an interplay of lamins and chromatin (and also perhaps the cell microenvironment[43]), both need to be intact for a physiologically relevant picture. In this study, our goal is to develop methods using AFM to extract quantitative mechanical information of cell nuclei

in situ. We applied these methods, as well as fluorescence imaging, to cancer and healthy cell nuclei of two organs: esophageal lines EPC2 (healthy) and CP-D (cancer), and colon lines FHC (healthy) and RKO (cancer). EPC2 (normal) and CP-D (high grade dysplasia) nuclei have distinct differences in nuclear volume (CP-D is larger) and smoothness of chromatin[153]. AFM measurements using soft cantilevers and shallow indentations reveal that EPC2 cells are stiffer than the CP-D cells, demonstrating cell softening during cancer progression[88], however nuclear stiffness was not determined.

Materials and Methods

Cell Culture and Sample Preparation

Isolated nuclei were provided on ice by Stuart Lindsay's lab in TE buffer (10 mM Tris, ~0.1 mM EDTA) and were obtained using detergent extraction with NP-40. Isolated nuclei were attached to glass bottom petri dishes. A small volume of poly-L-lysine (0.1% w/v, Sigma-Aldrich) was added to a glass bottom petri dish and allowed to incubate for at least several hours at room temperature, then was washed extensively with DPBS (no $CaCl_2$, no $MgCl_2$). Nuclei were diluted in the same DPBS buffer and added to the functionalized petri dish for measurements.

EPC2 and CP-D esophageal cells were cultured in Keratinocyte-SFM (Life Technologies) with the provided supplements. RKO cells were cultured in EMEM supplemented with 10% FBS. FHC cells are cultured in DMEM:F12 supplemented with 10mM HEPES, 10ng/mL cholera toxin, 0.005mg/mL insulin, 0.005mg/mL transferrin, 100ng/mL hydrocortisone, and 10% FBS. All growth media contains 1x penicillin-streptomycin (all culture materials from Life Technologies). Trichostatin-A (TS-A,

Sigma-Aldrich) was solubilized in DMSO and cells were treated for 24 hours at 1μM concentration unless noted otherwise. All whole cell experiments were performed in HBSS buffer containing 25mM HEPES and divalent cations $CaCl_2$ and $MgCl_2$ unless otherwise noted. Fluorescence experiments with EDTA were performed in HBSS with 5 mM EDTA, 25 mM HEPES, no $CaCl_2$, and no and $MgCl_2$. For AFM measurements, cells were seeded onto glass bottom petri dishes (World Precision Instruments) in full growth media until and allowed to adhere for two days before exchanging into buffer and measuring.

Fibronectin-coated PA gels were produced by a standard published protocol[154]. Acrylamide and bis-acrylamide gels were mixed at ratios described in the text using DPBS in place of water and were stamped on an APTES and glutaraldehyde functionalized glass petri dish using an untreated glass coverslip. Following polymerization, 0.2 mg/mL sulfo-SANPAH was conjugated with the PA gel for 20 minutes in UV light. The gels were washed in 50 mM HEPES at pH 8.5 buffer several times, and 0.1mg/mL fibronectin was added to the buffer and allowed to incubate overnight. After washing several times with full growth media, RKO cells were seeded and allowed to adhere for 36 hours before measuring.

Nucleic acids were fluorescently labeled with SYTO-9 (Life Technologies). Cells are incubated immediately before measuring at a concentration of 200 nM in measuring buffer for 20 min, then washed extensively with the measuring buffer.

Atomic force microscopy and fluorescence microscopy

The combined atomic force microscope and confocal laser scanning microscope system is described elsewhere[88,147] (also §4, §5). The AFM probes used were either Team Nanotec LRCH-750 sphero-conical probes (R~795 nm, k~0.13 N/m), Aspire CCS conical silicon probes (k~0.7 N/m), or AppNano SHOCON-200 (k~0.3 N/m). A constant loading rate of ~3 μm/s was used, and the trigger point was variable (~15 nN for LRCH-750 probes, 75-150 nN (EPC2, CP-D) or ~10 nN (RKO, FHC) for sharp probes for deep indentations).

AFM measurements and confocal microscopy on live cells were performed at 37°C. Widefield fluorescence measurements were performed on an Olympus IX71 at room temperature. AFM measurements of isolated nuclei were performed at 25°C in DPBS (no $CaCl_2$, no $MgCl_2$).

Data Analysis

AFM data was analyzed using the methods described in §3 with indentation depths defined in the main text. Data was analyzed using MATLAB. Nuclear areas from widefield fluorescence are determined using ImageJ. Statistical testing was performed by Mann-Whitney U test. Plots were generated in MATLAB and annotations and color adjustments are made in Inkscape.

Nuclear sizes distributions were produced by fitting the nucleus to an ellipse in ImageJ, the effective diameter d is calculated $d = \sqrt{4A/\pi}$, where A is the area. Heights (diameters) of isolated nuclei were determined by comparing the contact point of the nucleus and the contact point of glass in the AFM force-indentation data.

Fitting of AFM data on cells with the double-contact model is described in the results and discussion section.

Results and Discussion

Mechanics Extracted Nuclei and *In Situ* Nuclei Differ Drastically

Directly probing the mechanics of cell nuclei is difficult because of the presence of the surrounding cell which may distort the force-response from the nucleus. Therefore, it is beneficial to first extract and isolate the nucleus before performing AFM indentation experiments to remove any effects from the cell.

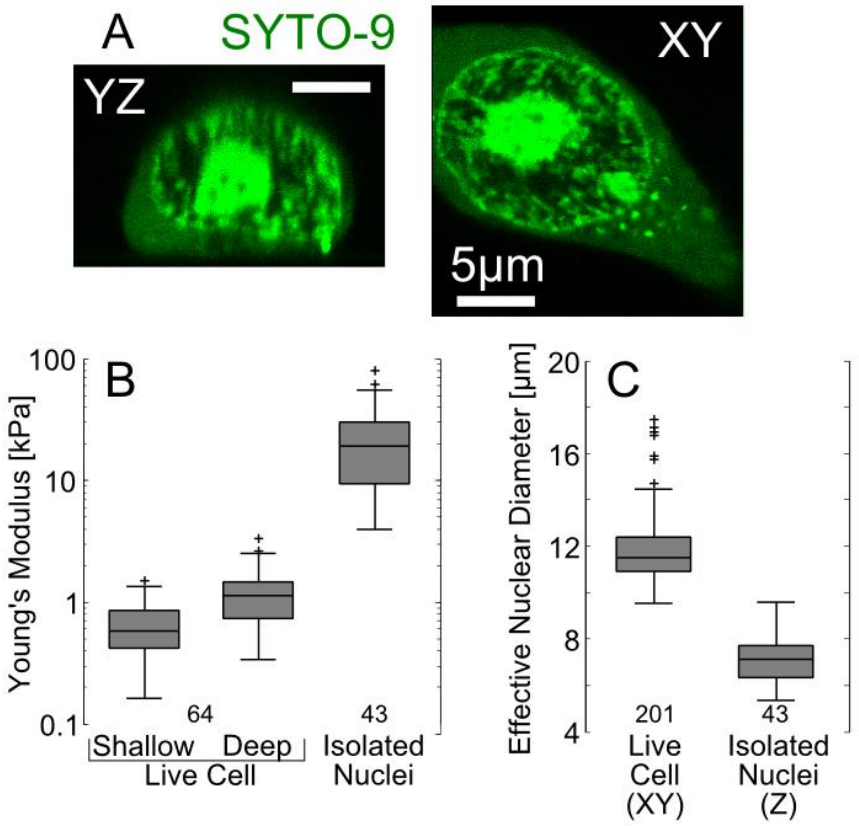

Figure 6-1: Young's modulus of RKO cells and isolated nuclei. (A) Confocal fluorescence (YZ on left, XY on right) images of RKO cells stained with SYTO-9 for nucleic acids. (B) Young's modulus of RKO cells and isolated nuclei. For shallow indentations, the indentation bin is 0.25-2.50 μm, and for deep indentations the bin is 2.00-4.00 μm, and for isolated nuclei the bin is from 100nm to the trigger. (C) Effective diameters of nuclei inside live cells and isolated nuclei. The live cell diameters are determined by widefield fluorescence, and the isolated nuclei diameters are determined from the sample topography from AFM contact points.

We performed AFM indentation using LRCH sphero-conical probes with large radii (~795 nm) experiments on live RKO cells and isolated nuclei which were adhered to a glass petri dish functionalized with poly-L-lysine. Confocal fluorescence imaging (Figure 6-1A) demonstrates that the volume of the RKO nuclei in live cells is very large compared to the overall volume of the cell, and that the nucleus is very near the apical surface of the cell. Thus, AFM indentations on live RKO cells directly above the nucleus

should be primarily probing the mechanical properties of the nucleus. Additionally, as the fluorescence signal comes from a nucleic acid stain, the localization of dye in the nucleus is very heterogeneous indicating dense regions of heterochromatin. The results of the AFM indentation experiments and resulting Young's moduli are shown in Figure 6-1B. As the indentation depth increases, the average stiffness of the nuclei increases from 0.58±0.18 kPa (median ± median absolute deviation unless otherwise noted) to 1.14±0.38 kPa, presumably because the nuclear mechanics are probed more than the cytoplasmic mechanics. However, AFM indentations on isolated nuclei result in a dramatically higher Young's modulus of 19.10±10.08 kPa.

Additionally, the diameters of the nuclei inside live cells and isolated nuclei differed drastically, as shown in Figure 6-1C. The nuclei diameters of live cells (measured with widefield fluorescence) was 11.5±0.7 μm, while the diameters of the isolated nuclei (measured from the AFM topography) was 7.1±0.7 μm. Additionally, the stiffness of isolated nuclei was determined be the negatively correlated with nuclear diameter.

There are several explanations for these dramatic differences in stiffness and morphology observed between live cell nuclei and extracted nuclei. If volume from water was lost from the nucleus during extraction, then this would explain the correlation between the diameter and Young's modulus as the intranuclear pressure is much higher. The nuclei are "glued" to the petri dishes using poly-L-lysine, thus it is possible that this procedure introduces a large amount of prestress in the nucleus which would be observed with AFM. The buffer for measuring the stiffness of the RKO isolated nuclei is stripped of divalent cations $MgCl_2$ and $CaCl_2$, and the buffer for live cells contains these divalent

cations, and the addition of divalent cations is shown to increase nuclear stiffness[55], however despite this the nuclei still have over and order of magnitude larger elastic modulus than the nuclei *in situ*.

Recent studies have shown that the mechanics cell nucleus is governed by the properties of the whole cell, including actomyosin contracility[56] and even the extracellular matrix through distant mechanotransduction pathways[43]. Because of this, any study of nuclear mechanics should include the entire cell as it is necessary for a physiologically relevant picture.

RKO cells have a very accessible nucleus due to its large volume compared to the whole cell volume, however EPC2 and CP-D cells do not have this benefit, and the nucleus may be buried under a thick layer of cytoskeleton and cytoplasm. Thus, additional tools must be developed to extract nuclear mechanical properties and deconvolute from the cytoplasm.

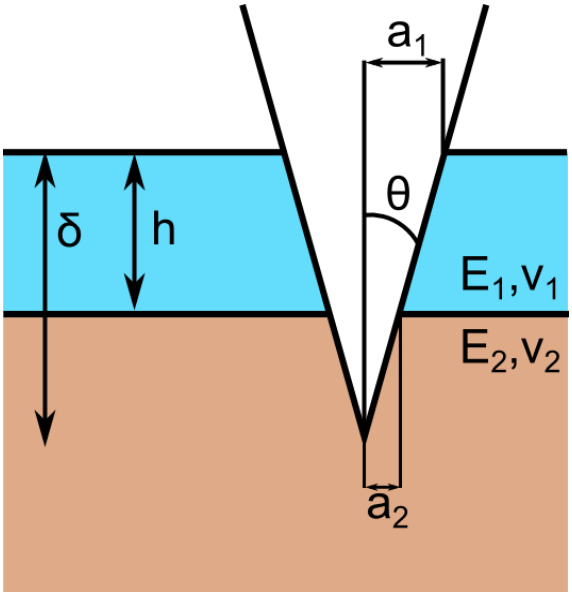

Figure 6-2: Schematic of the double contact model assumed in this work. Here, the tip shape is conical resulting in a small contact radius *a*. The bottom layer is not detectable in the force response until the probe makes contact.

AFM Indentation Rheology of *In Situ* Nuclei

In order to determine the elasticity of nuclei which are deeply embedded in the cells, the effects of the surrounding cytoplasm and cytoskeleton must be subtracted from the overall force response. The two-layer model derived in §4 cannot work in this case, as the previously derived model can only be used to determine the effects of the substrate on the indentation into the top layer and is not asymptotic to indentations on the bottom layer. However, several key concepts were introduced in the development of the two-layer model: in the case of the bottom layer being stiffer than the top layer, and in the case of indenter geometries with low contact radii, the force response from indentation does not differ too dramatically from the homogeneous case. Therefore, in these cases there is very little strain on the bottom layer unless the probe forms contact with the bottom layer (or the top layer is at an incompressible limit). It was also demonstrated that there is very poor mechanical contrast regarding the stiffness of the bottom layer when it is stiffer than the top layer (unless the contact radius is unusually high, about 10x stiffer is the saturation point). These insights suggest the feasibility of a "biopsy" type measurement for subsurface elasticity shown in Figure 6-2, where the probe is pushed through the top layer into the bottom layer and a simple double contact model is assumed:

$$F(\delta < h) = \frac{E_1 {a_1}^2 \pi \cot\theta}{2(1 - {v_1}^2)} \tag{6-1}$$

$$a_1 = \frac{2\delta}{\pi \cot\theta} \tag{6-2}$$

Which is Sneddon's model and identical to Eqs. (3-15), (3-17). However, when the probe is indented through to the bottom layer, the force response may be approximated as

$$F(\delta > h) = \frac{E_1({a_1}^2 - {a_2}^2)\pi \cot\theta}{2(1-{\upsilon_1}^2)} + \frac{E_2{a_2}^2\pi \cot\theta}{2(1-{\upsilon_2}^2)} \tag{6-3}$$

$$a_2 = \frac{2(\delta - h)}{\pi \cot\theta} \tag{6-4}$$

This naïve double contact model is continuous and twice differentiable at $\delta=h$ and $E_1=E_2$, satisfying the necessary boundary conditions. The key assumptions to this model are that the low contact radius results in little change from Sneddon's model and the stiffer bottom layer results in little to no strain in the bottom layer until the probe comes into contact, so if these conditions are not met then the model is not viable and may be inaccurate. These assumptions also make the model poor for predicting the behavior of the force-indentation response at the transition region ($\delta \approx h$) as some deviations are expected.

Practically, this model may be fit on the force-indentation data using least-squares method. However, due to consideration in contact point errors (discussed in §3), we apply this method by performing a least-squares fit on the results from a depth-dependent fit of the data applying a conical contact model with 500 nm indentation bins (identical to performing a least-squares regression on the slope of $F^{1/2}$ data along indentation bins). The first 500 nm and last 250 nm of the force-indentation curve are omitted from the least-squares fit to remove small indentation artifacts of sharp probes and potential glass effects.

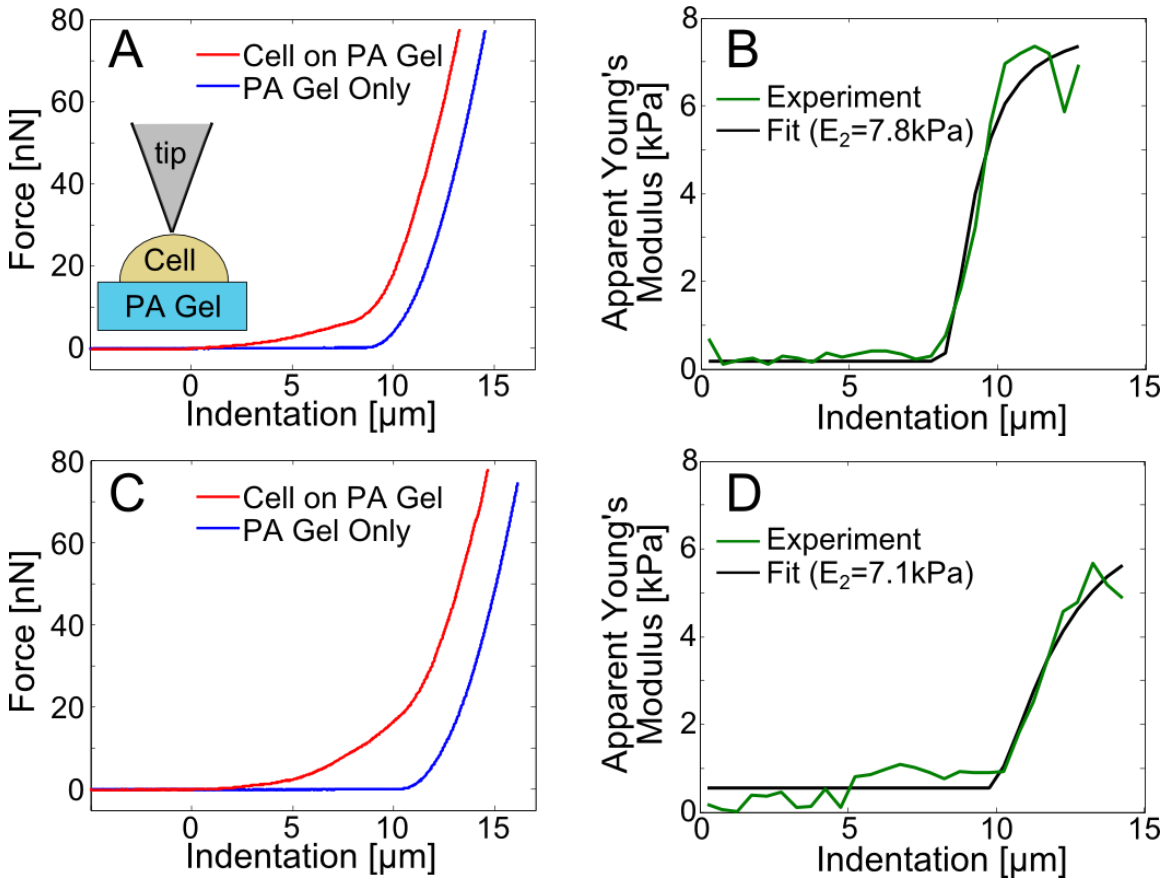

Figure 6-3: Demonstration of using a sharp probe to probe subsurface elasticity. Schematic of the experiment is shown in (A), a cell is grown on a fibronectin conjugated PA gel (5% acrylamide, 0.3% bis-acrylamide, E=7.6±0.2 kPa, mean±s.t.d.) and indented with a sharp AFM probe (SHOCON-200, θ~20°). (A) shows the force-indentation curves on only the PA gel and on the cell, both are aligned to the contact point of the cell. (B) shows the depth-dependent fit of the data in green and the theory fit using Eq. (6-1)-(6-4) and the resulting PA gel stiffness from the fit. (C) and (D) are similar to (A) and (B) with another cell. The resulting Young's modulus of the PA gel underneath the cells was found to be 7.3±0.4 kPa (n=7).

We next tested the feasibility of this model using a model system of RKO cells cultured on an ideally elastic PA gel conjugated with fibronectin to allow cell adhesion. While the cell is very mechanically heterogeneous, the PA gel is not and serves as a good platform for determining whether the elastic modulus of the bottom layer may be properly deconvoluted.

Figure 6-3 shows the results of the AFM force-indentation experiments on the system along with the fits using the above theory. The elastic modulus of the PA gel (5% acrylamide, 0.3% bis-acrylamide) is 7.6±0.2 kPa (mean±std) determined from force-indentation curves over gel regions with no cells. The deep force-indentation curves on the cells are deconvoluted and the resulting modulus is 7.3±0.4 kPa (n=7), showing strong agreement between the experimental data and the naïve theory. However, the heights that are determined from fitting the experimental data show deviations in the height of the sample compared to determining the sample height from the contact points – fits from the model predicts that the samples are 470 nm shorter on average than the results from the contact points. This may due to several factors, including the bin size used in the regression for the depth-dependent fits (500 nm in this case), general errors in contact point determination for sharp AFM probes, or non-linearities in the force-response that were assumed negligible.

It should also be noted that contact point determination is particularly critical and difficult under the conditions of these experiments. Because the indentation depths must be extremely deep, and it is assumed $E_1 << E_2$, the spring constant of the AFM probe must be relatively high and is typically not ideal for determining sample properties of the soft top layer. The elastic response of the top layer may be on the same order of the noise level of stiff cantilevers, thus serious contact point errors may occur.

Figure 6-3 B, D also demonstrate transition regions in the fits from the soft elastic layer to the stiff substrate. When the layer height is shorter and the elastic mismatch is larger, the slope of the transition is much higher (Figure 6-3B). However, for taller first layers and lower elastic mismatches, the slope is much more gradual (Figure 6-3D).

Because both parameters are fit in the model, it is important that the apparent Young's modulus begins to plateau at sufficient depths into the second layer, otherwise large errors in the regression may occur.

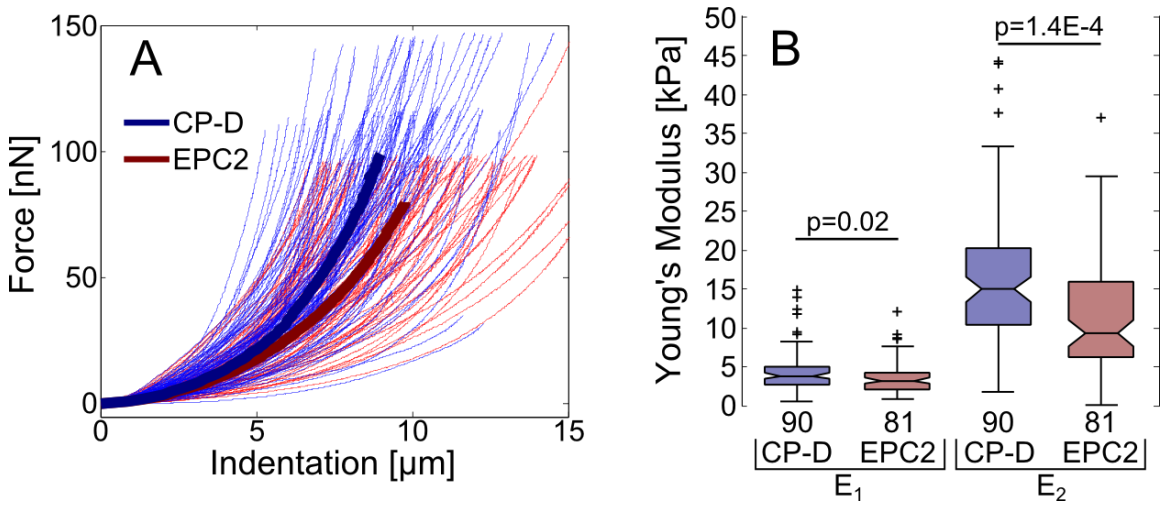

Figure 6-4: Deep indentations on CP-D and EPC2 cells showing nuclear stiffness. (A) Average force-indentation curves computed using method 2 from [149] with CP-D in blue and EPC2 in red. (B) Boxplot showing the Young's modulus for the top (E_1) and bottom (E_2) layers fit using the theory described here with number of replicates at the bottom. P-values are calculated from the Mann-Whitney U test.

We applied this method to EPC2 (healthy) and CP-D (high grade dysplasia) esophageal cells. A CCS conical probe (θ~15°) with high spring constant (k~0.7 N/m) was used to indent the cells extremely deep. The force-indentation curves, along with the average force-indentation curve, is shown in Figure 6-4A, showing the CP-D cells are stiffer at deep indentations. The resulting force-indentation curves were fit with the above theory to determine the Young's modulus of the nuclei underneath the cytoplasm. CP-D cells were found to have a top layer Young's modulus 3.82±1.17 kPa and bottom layer 14.93±5.23 kPa. EPC2 cells were found to have a top layer Young's modulus

3.19±1.06 kPa and bottom layer 9.27±4.78 kPa. The Young's modulus of the bottom layer (presumably the nucleus in this system) were significantly different (p=1.4E-4), with the cancerous CP-D nuclei being stiffer than EPC2 nuclei. This result, however, is in contrast with previous AFM studies of esophageal cells where the CP-D cells were found to be much softer than EPC2 cells[88], however this study featured a much softer AFM cantilever, shallow indentations, and were fit using the Hertz model. CP-D cells are known to have a more heterogeneous chromatin structure with more dense regions of heterochromatin compared to EPC2 cells[153], thus our result corroborates theories correlating nuclear stiffness with chromatin condensation[52,53].

HDAC Inhibition Effects Cancerous but not Normal Cells

As previously discussed, chromatin structure has been shown to play a large role in nuclear stiffness. The HDAC inhibitor TS-A has been used previously in nuclear mechanics measurements to reduce the stiffness of the nucleus by decondensing the chromatin structure[53,152]. Treatment of TS-A has also been demonstrated by Chalut *et. al.* to reduce the nuclei "fractal dimension", which is an order parameter describing how heterogeneous the chromatin distribution in the nucleus is (when the chromatin structure is decondensed, the distribution becomes much more homogeneous)[53]. Because the amount of condensed heterochromatin is associated with cancer cells, we wanted to see if there are differences in the mechanical properties of the nucleus *in situ* between the healthy and cancerous cell lines after treatment with TS-A.

Figure 6-5 shows widefield fluorescence images of the four cell lines when treated with TS-A and the empty vehicle controls. The two cancerous cell lines, CP-D

and RKO, show drastic morphological changes, whereas the normal cell lines EPC2 and FHC display minimal changes.

Figure 6-6 shows AFM force-indentation data on the nuclei using a SHOCON-200 pyramidical tip with intermediate spring constant (k~0.3 N/m), as well as the resulting fits for E_1 and E_2 using the theory described above. Table 6-1 shows the results of the fits on all of the curves for all three parameters E_1, E_2, and h. With the softer cantilever, the EPC2 and CP-D were found to have similar nuclear stiffness, and EPC2 cells are shown to have a stiffer E_1, which is consistent with literature. The cancer cell lines RKO and CP-D display drastic differences in the force response and resulting E_2 compared to the normal cell lines, indicating the cancer lines respond to the HDAC treatment whereas the healthy cells show much less response. The cancer cells are shown to have much lower E_2, indicating that the nuclear stiffness has drastically decreased, which is consistent with other work in literature where chromatin decondensation will result in less rigid nuclei[53,55]. However, as demonstrated in Figure 6-5 and the fits for h in Table 6-1, the morphology of the whole cells was altered drastically by the presence of TS-A, therefore the change in force response at deep indentations may not be truly indicative of nuclear mechanical changes but rather deviations from the strong assumptions made in the model derivation. In the case of CP-D cells, when fitting to the double-contact model reveals a similar h value, the values for E_2 are similar as well, indicating that the cell morphology is the driving change in the change in Young's modulus as opposed to the decondensation of chromatin. This may indicate that the value of E_2 obtained from these fits is not indicative of the cell nucleus, but rather the cytoplasmic stiffness that is typically assumed to be E_1.

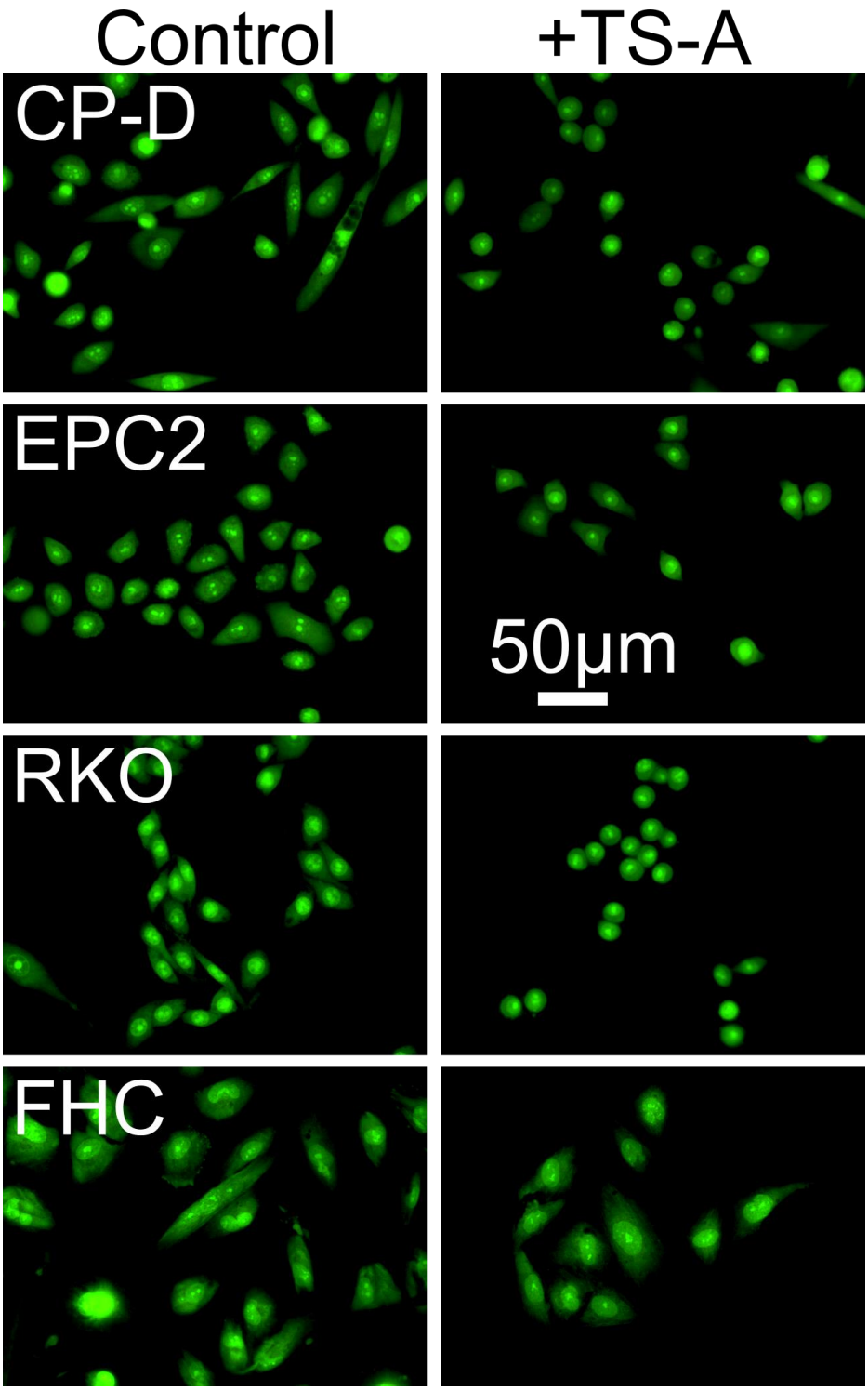

Figure 6-5: Fluorescence images of cells treated with Trichostatin-A. Left column shows control (DMSO empty vehicle) and right column are cells after 24 hours in 1 µM TS-A. Scale bar is the same (50 µm) for all images.

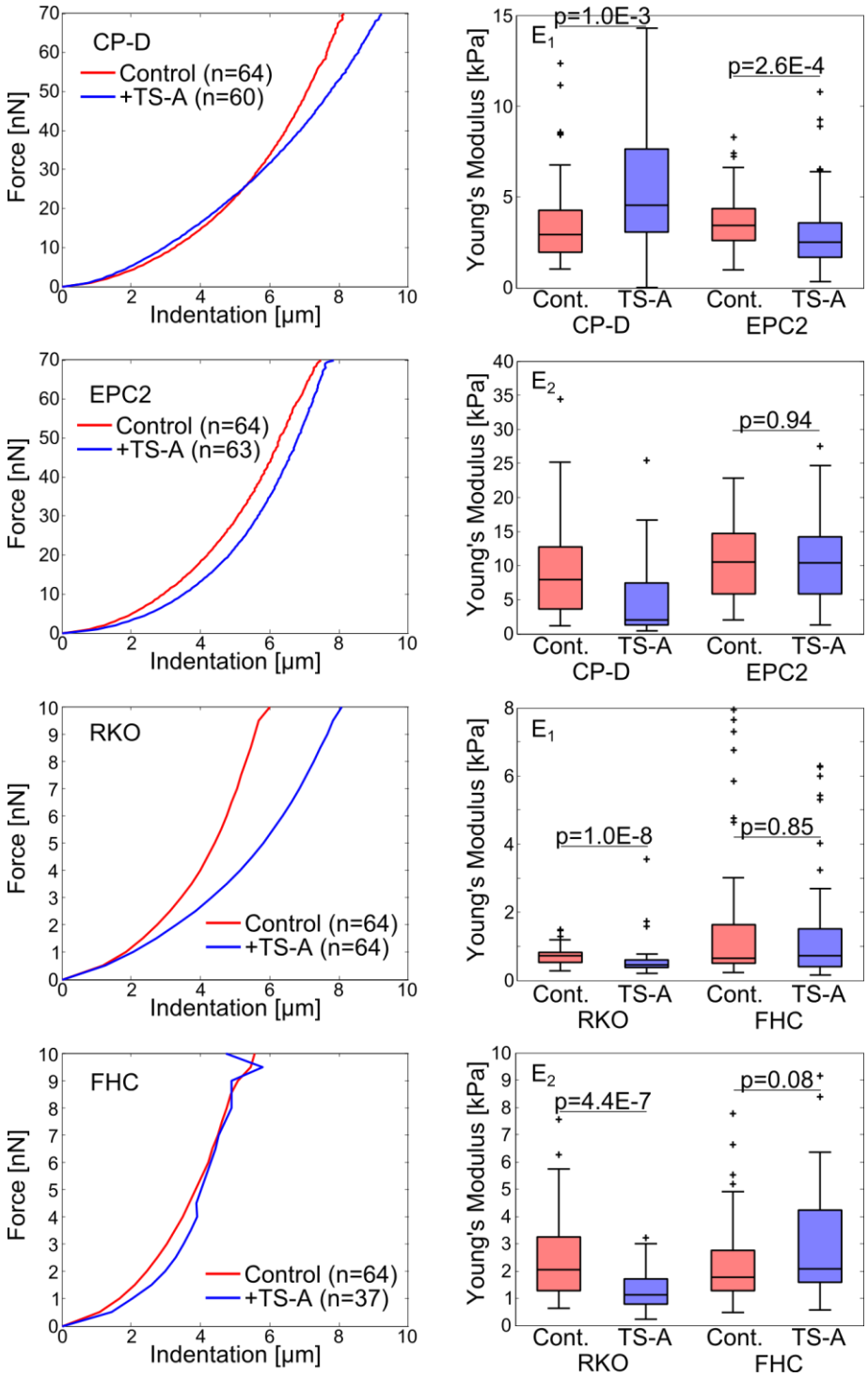

Figure 6-6: Force data on nuclei in situ on cells treated with TS-A. The left column shows average force-indentation curves from each of the cell lines with and without TS-A. The right column shows box plots of the resulting fits of E_1 and E_2 using the theory derived in this chapter. For all cases, red is control (DMSO empty vehicle) and blue is treated with TS-A (24 hr, 1 μM).

Cell Line	Time [hr]	TS-A [nM]	Number of Cells n	Young's Modulus [kPa] (median ± m.a.d.)		E_2 Depth [μm] (median ± m.a.d.) h
				E_1	E_2	
CP-D	2	0	64	2.35 ± 0.58	11.00 ± 3.51	5.1 ± 1.4
		300	63	2.09 ± 0.58	9.58 ± 3.23	5.0 ± 1.3
	24	0	64	2.95 ± 1.09	7.98 ± 4.71	4.3 ± 1.8
		1000	60	4.53 ± 2.38	1.99 ± 1.15	1.2 ± 0.6
EPC2	2	0	64	3.34 ± 0.96	10.32 ± 4.32	3.1 ± 1.0
		300	63	2.81 ± 0.72	9.79 ± 3.32	4.2 ± 1.4
	24	0	64	3.46 ± 0.91	10.55 ± 4.39	3.7 ± 1.4
		1000	63	2.53 ± 0.96	10.46 ± 4.59	3.9 ± 1.3
RKO	24	0	64	0.73 ± 0.16	2.03 ± 0.98	3.2 ± 0.8
		1000	64	0.46 ± 0.09	1.12 ± 0.34	6.3 ± 3.0
FHC	24	0	64	0.66 ± 0.32	1.76 ± 0.58	2.7 ± 0.8
		1000	37	0.73 ± 0.38	2.09 ± 0.78	2.5 ± 0.6

Table 6-1: Results from fitting the AFM force-indentation curves to the double-contact model. The force-indentation data was collected using a SHOCON-200 probe.

Conclusions

The cell nucleus is the most critical organelle of the cell as it is the location where genetic information is stored and the center for transcription, thus abnormal deformations or mechanics may contribute to human disease such as cancer. Other studies have shown that nuclear mechanics is regulated by the cell's cytoskeleton and the cell's microenvironment[43]. Thus, studying the nucleus *in situ* provides the best understanding of the cellular and nuclear response to external forces and deformations. We demonstrate that the properties of isolated nuclei differ drastically from *in situ*, showing that the

applications of nuclear mechanics may be hindered by various steps in the preparation of the samples.

In this work, we have developed a theoretical framework for determining the elastic modulus of an embedded material by performing a deep indentation on the sample with a probe with small contact radius and performing a naïve deconvolution. We demonstrated on a model experimental system of cells cultured on PA that the method provides an accurate description of the subsurface elastic modulus. The method was applied to determine the nuclear elastic modulus for several cell lines. When these cell lines are treated with HDAC inhibition, the chromatin structure relaxes and decondenses, and the nuclear properties of the cancerous cell lines are affected dramatically compared to the normal cells. Additional experiments must be conducted to ensure that the assumptions made in the double-contact model are representative of the experimental reality, as highlighted by the AFM results of the CP-D cells when treated with TS-A, as well as other strategies to affect the elasticity of the nucleus (for example EDTA treatment, disruption of the lamin or actomyosin network, or adjusting the microenvironment of the cell). Dynamic rheology may also be used to determine the viscous response of the nuclear components compared with the elastic response.

7 CONCLUSIONS AND OUTLOOK

This dissertation has presented novel methods and applications of AFM on heterogeneous biological systems. §4 introduced the analysis of force-indentation data on heterogeneous samples and demonstrated the accuracy with FEA and experiments. §5 and §6 demonstrate applications of the theoretical framework on two mechanically heterogeneous biological systems: cells embedded in ECM and cell nuclei *in situ*.

While this dissertation was primary focused on the elastic response of soft matter, there is still many properties extracted from direct indentations that contribute to the final force-response, for example temporal effects, plasticity, or non-incompressible Poisson's ratios. Fortunately, the combined AFM/CLSM microscope is capable of addressing all of these, either by standalone dynamic rheology or indentations with some embedded fluorescent nanoparticles to observe deformation fields and how they deviate from the elastic case. While these properties are not known, the possibility of directly addressing them is an exciting outlook.

§4 is a novel contribution to the field of indentation-based rheometry. Several groups have studied the effects of a stiff substrate on the elastic response of a thin layer during an indentation[83,92,93], however the framework presented here is much more general and works for any tip geometry and elastic mismatch. The two-layer effects are most pronounced when the bottom layer is softer than the top layer and this effect must be taken into account when designing AFM indentation experiments. Combing this fact, along with the double-contact model demonstrate in §6 to determine the elasticity of deeply embedded objects and maximizing mechanical contrast using the knowledge

gained from §4, this dissertation provides a key advancement regarding indentation rheometry.

The biological results presented offer new concepts for studying cell phenotype in complex environments. It was determined in §5 that MDA-MB-231 cells become stiffer as they invade in collagen I matrices, and in §6 it was demonstrated that cell nuclei *in situ* have drastically different elastic properties compared with isolated nuclei. However, most current AFM-based research on these are on cells adhered to petri dishes or nuclei extracted from cells. These experiments and analysis are much easier, however we have demonstrated that they are missing key elements which drastically alter the properties of the system, thus the applicability is limited. While measurements in 3D is gaining traction in recent years and the need for studies of cells in 3D environments is becoming very apparent, the research presented in this dissertation is a large step forward in extending the capabilities of AFM to work for cells embedded in complex microenvironments.

The cell mechanics presented here raise the possibility for future studies. For example from §5, while ROCK is implicated in the pathways involved in cell stiffening, exact causes and contributions not exactly known -- other GTPase pathways, collagen realignment or MMP digestion of the collagen, nuclear or stress fiber positioning, or the dynamics of collective cell invasion may also play a large role. In addition, only one (highly metastatic) cell line was investigated, however cells from different organs or containing different mutations are likely to behave differently, thus the result is not yet general. The “next generation” of experiments related to this have recently begun in the Ros lab and are already delivering promising new results.

In §6 (and in literature), nuclear stiffness is shown to be correlated with chromatin condensation. However, the nuclear lamin structure is anchored to the cell cytoskeleton, and gene expression has been shown in literature to be correlated with extracellular stiffness, thus there is a complex mechanotransduction network that regulates nuclear properties. Using AFM to directly probe nuclear mechanics as the environment changes is an exciting prospect and may lead to new concepts for mechanobiology.

Albert Einstein is attributed with, "everything should be made as simple as possible, but no simpler." Complexity and heterogeneity are hallmarks of biological systems, attempting to simultaneously address all aspects at once is a monumentally challenging task, however reducing the problem to simpler components leads to results which may be generalized an applied. Here, classical elasticity theory has also been extended to biphasic heterogeneous materials at the cost of simplicity, although it is necessary for understanding these systems.

REFERENCES

1. Engler, A. J., Sen, S., Sweeney, H. L. & Discher, D. E. Matrix Elasticity Directs Stem Cell Lineage Specification. *Cell* **126,** 677–689 (2006).

2. Paszek, M. J. *et al.* Tensional homeostasis and the malignant phenotype. *Cancer Cell* **8,** 241–254 (2005).

3. *OpenStax College, Biology*. (OpenStax College, 2013). at <http://cnx.org/content/col11448/latest/>

4. Alberts, B. *et al. Molecular Biology of the Cell*. (Garland Science, 2008).

5. Ridley, A. J. *et al.* Cell migration: integrating signals from front to back. *Science (80-.).* **302,** 1704–9 (2003).

6. Le Clainche, C. & Carlier, M.-F. Regulation of actin assembly associated with protrusion and adhesion in cell migration. *Physiol. Rev.* **88,** 489–513 (2008).

7. Kabsch, W., Mannherz, H. G., Suck, D., Pai, E. F. & Holmes, K. C. Atomic structure of the actin: DNase I complex. *Nature* **347,** 37–44 (1990).

8. Holmes, K. C., Popp, D., Gebhard, W. & Kabsch, W. Atomic model of the actin filament. *Nature* **347,** 44–49 (1990).

9. Suresh, S. Biomechanics and biophysics of cancer cells. *Acta Biomater.* **3,** 413–438 (2007).

10. Korn, E. D., Carlier, M.-F. & Pantaloni, D. Actin polymerization and ATP hydrolysis. *Science (80-.).* **238,** 638–644 (1987).

11. Vargas-Pinto, R., Gong, H., Vahabikashi, A. & Johnson, M. The effect of the endothelial cell cortex on atomic force microscopy measurements. *Biophys. J.* **105,** 300–309 (2013).

12. Wakatsuki, T., Schwab, B., Thompson, N. C. & Elson, E. L. Effects of cytochalasin D and latrunculin B on mechanical properties of cells. *J. Cell Sci.* **114,** 1025–1036 (2001).

13. Geiger, B., Bershadsky, A., Pankov, R., Yamada, K. M. & Correspondence, B. G. Transmembrane extracellular matrix– cytoskeleton crosstalk. *Nat. Rev. Mol. Cell Biol.* **2,** 793–805 (2001).

14. Le Duc, Q. *et al.* Vinculin potentiates E-cadherin mechanosensing and is recruited to actin-anchored sites within adherens junctions in a myosin II-dependent manner. *J. Cell Biol.* **189,** 1107–1115 (2010).

15. Fletcher, D. A. & Mullins, R. D. Cell mechanics and the cytoskeleton. *Nature* **463,** 485–492 (2010).

16. Pelling, A. E. *et al.* Distinct contributions of microtubule subtypes to cell membrane shape and stability. *Nanomedicine Nanotechnology, Biol. Med.* **3,** 43–52 (2007).

17. Storm, C., Pastore, J. J., MacKintosh, F. C., Lubensky, T. C. & Janmey, P. A. Nonlinear elasticity in biological gels. *Nature* **435,** 191–194 (2005).

18. Onck, P. R., Koeman, T., Van Dillen, T. & Van Der Giessen, E. Alternative explanation of stiffening in cross-linked semiflexible networks. *Phys. Rev. Lett.* **95,** 178102 (2005).

19. Van Dillen, T., Onck, P. R. & Van der Giessen, E. Models for stiffening in cross-linked biopolymer networks: A comparative study. *J. Mech. Phys. Solids* **56,** 2240–2264 (2008).

20. Janmey, P. A. *et al.* Negative normal stress in semiflexible biopolymer gels. *Nat. Mater.* **6,** 48–51 (2007).

21. Brown, A. E. X., Litvinov, R. I., Discher, D. E., Purohit, P. K. & Weisel, J. W. Multiscale mechanics of fibrin polymer: gel stretching with protein unfolding and loss of water. *Science (80-.).* **325,** 741–744 (2009).

22. Münster, S. *et al.* Strain history dependence of the nonlinear stress response of fi brin and collagen networks. *Proc. Natl. Acad. Sci.* **110,** 12197–12202 (2013).

23. Levental, I., Georges, P. C. & Janmey, P. A. Soft biological materials and their impact on cell function. *Soft Matter* **3,** 299 (2007).

24. Wolf, K. *et al.* Physical limits of cell migration: Control by ECM space and nuclear deformation and tuning by proteolysis and traction force. *J. Cell Biol.* **201,** 1069–1084 (2013).

25. Kleinman, H. K. & Martin, G. R. Matrigel: Basement membrane matrix with biological activity. *Semin. Cancer Biol.* **15,** 378–386 (2005).

26. Soofi, S. S., Last, J. A., Liliensiek, S. J., Nealey, P. F. & Murphy, C. J. The elastic modulus of Matrigel™ as determined by atomic force microscopy. *J. Struct. Biol.* **167,** 216–219 (2009).

27. Alcaraz, J. *et al.* Laminin and biomimetic extracellular elasticity enhance functional differentiation in mammary epithelia. *EMBO J.* **27,** 2829–2838 (2008).

28. Pelham, R. J. J. & Wang, Y.-L. Cell locomotion and focal adhesions are regulated by substrate flexibility. *Proc. Natl. Acad. Sci.* **94,** 13661–13665 (1997).

29. Lee, Y., Huang, J., Wang, Y. & Lin, K. Three-dimensional fibroblast morphology on compliant substrates of controlled negative curvature. *Integr. Biol.* **5,** 1447–55 (2013).

30. Lin, J. *et al.* Morphology and organization of tissue cells in 3D microenvironment of monodisperse foam scaffolds. *Soft Matter* **7,** 10010 (2011).

31. Nikkhah, M., Edalat, F., Manoucheri, S. & Khademhosseini, A. Engineering microscale topographies to control the cell-substrate interface. *Biomaterials* **33,** 5230–5246 (2012).

32. Ingber, D. E. Tensegrity: the architectural basis of cellular mechanotransduction. *Annu. Rev. Physiol.* **59,** 575–599 (1997).

33. Amano, M., Nakayama, M. & Kaibuchi, K. Rho-kinase/ROCK: A key regulator of the cytoskeleton and cell polarity. *Cytoskeleton* **67,** 545–554 (2010).

34. Etienne-Manneville, S. & Hall, A. Rho GTPases in cell biology. *Nature* **420,** 629–635 (2002).

35. Friedl, P. & Wolf, K. Tumour-cell invasion and migration: diversity and escape mechanisms. *Nat. Rev. Cancer* **3,** 362–374 (2003).

36. Friedl, P. & Wolf, K. Plasticity of cell migration: A multiscale tuning model. *J. Cell Biol.* **188,** 11–19 (2010).

37. Petrie, R. J., Koo, H. & Yamada, K. M. Generation of compartmentalized pressure by a nuclear piston governs cell motility in a 3D matrix. *Science (80-.).* **345,** 1062–1065 (2014).

38. Yamazaki, D., Kurisu, S. & Takenawa, T. Involvement of Rac and Rho signaling in cancer cell motility in 3D substrates. *Oncogene* **28,** 1570–1583 (2009).

39. Petrie, R. J., Gavara, N., Chadwick, R. S. & Yamada, K. M. Nonpolarized signaling reveals two distinct modes of 3D cell migration. *J. Cell Biol.* **197,** 439–455 (2012).

40. Solon, J., Levental, I., Sengupta, K., Georges, P. C. & Janmey, P. A. Fibroblast adaptation and stiffness matching to soft elastic substrates. *Biophys. J.* **93,** 4453–4461 (2007).

41. Ghibaudo, M. *et al.* Traction forces and rigidity sensing regulate cell functions. *Soft Matter* **4,** 1836–1843 (2008).

42. Saez, A., Ghibaudo, M., Buguin, A., Silberzan, P. & Ladoux, B. Rigidity-driven growth and migration of epithelial cells on microstructured anisotropic substrates. *Proc. Natl. Acad. Sci. U. S. A.* **104,** 8281–8286 (2007).

43. Swift, J. *et al.* Nuclear lamin-A scales with tissue stiffness and enhances matrix-directed differentiation. *Science (80-.).* **341,** 1240104 (2013).

44. Holle, A. W. *et al.* In situ mechanotransduction via vinculin regulates stem cell differentiation. *Stem Cells* **31,** 2467–2477 (2013).

45. Trappmann, B. *et al.* Extracellular-matrix tethering regulates stem-cell fate. *Nat. Mater.* **11,** 742–742 (2012).

46. Wen, J. H. *et al.* Interplay of matrix stiffness and protein tethering in stem cell differentiation. *Nat. Mater.* **13,** 979–987 (2014).

47. Kilian, K. A., Bugarija, B., Lahn, B. T. & Mrksich, M. Geometric cues for directing the differentiation of mesenchymal stem cells. *Proc. Natl. Acad. Sci. U. S. A.* **107,** 4872–4877 (2010).

48. Dahl, K. N., Ribeiro, A. J. S. & Lammerding, J. Nuclear shape, mechanics, and mechanotransduction. *Circ. Res.* **102,** 1307–1318 (2008).

49. Dahl, K. N., Kahn, S. M., Wilson, K. L. & Discher, D. E. The nuclear envelope lamina network has elasticity and a compressibility limit suggestive of a molecular shock absorber. *J. Cell Sci.* **117,** 4779–4786 (2004).

50. Lammerding, J. *et al.* Lamin A/C deficiency causes defective nuclear mechanics and mechanotransduction. *J. Clin. Invest.* **113,** 370–378 (2004).

51. Isermann, P. & Lammerding, J. Nuclear mechanics and mechanotransduction in health and disease. *Curr. Biol.* **23,** R1113–R1121 (2013).

52. Pajerowski, J. D., Dahl, K. N., Zhong, F. L., Sammak, P. J. & Discher, D. E. Physical plasticity of the nucleus in stem cell differentiation. *Proc. Natl. Acad. Sci. U. S. A.* **104,** 15619–15624 (2007).

53. Chalut, K. J. *et al.* Chromatin decondensation and nuclear softening accompany Nanog downregulation in embryonic stem cells. *Biophys. J.* **103,** 2060–2070 (2012).

54. Mazumder, A., Roopa, T., Basu, A., Mahadevan, L. & Shivashankar, G. V. Dynamics of chromatin decondensation reveals the structural integrity of a mechanically prestressed nucleus. *Biophys. J.* **95,** 3028–3035 (2008).

55. Dahl, K. N., Engler, A. J., Pajerowski, J. D. & Discher, D. E. Power-law rheology of isolated nuclei with deformation mapping of nuclear substructures. *Biophys. J.* **89,** 2855–2864 (2005).

56. Li, Q., Kumar, A., Makhija, E. & Shivashankar, G. V. The regulation of dynamic mechanical coupling between actin cytoskeleton and nucleus by matrix geometry. *Biomaterials* **35,** 961–969 (2014).

57. Pagliara, S. *et al.* Auxetic nuclei in embryonic stem cells exiting pluripotency. *Nat. Mater.* **13,** 638–44 (2014).

58. Caille, N., Thoumine, O., Tardy, Y. & Meister, J. J. Contribution of the nucleus to the mechanical properties of endothelial cells. *J. Biomech.* **35,** 177–187 (2002).

59. Hanahan, D. & Weinberg, R. A. The Hallmarks of Cancer. *Cell* **100,** 57–70 (2000).

60. Hanahan, D. & Weinberg, R. A. Hallmarks of cancer: The next generation. *Cell* **144,** 646–674 (2011).

61. Wirtz, D., Konstantopoulos, K. & Searson, P. C. The physics of cancer: the role of physical interactions and mechanical forces in metastasis. *Nat. Rev. Cancer* **11,** 512–522 (2011).

62. Kumar, S. & Weaver, V. M. Mechanics, malignancy, and metastasis: The force journey of a tumor cell. *Cancer Metastasis Rev.* **28,** 113–127 (2009).

63. Levental, K. R. *et al.* Matrix Crosslinking Forces Tumor Progression by Enhancing Integrin Signaling. *Cell* **139,** 891–906 (2009).

64. Weaver, V. M. *et al.* Reversion of the malignant phenotype of human breast cells in three- dimensional culture and in vivo by integrin blocking antibodies. *J. Cell Biol.* **137,** 231–245 (1997).

65. Wang, F. *et al.* Reciprocal interactions between beta1-integrin and epidermal growth factor receptor in three-dimensional basement membrane breast cultures: a

different perspective in epithelial biology. *Proc. Natl. Acad. Sci. U. S. A.* **95,** 14821–14826 (1998).

66. Tanner, K., Mori, H., Mroue, R., Bruni-Cardoso, A. & Bissell, M. J. Coherent angular motion in the establishment of multicellular architecture of glandular tissues. *Proc. Natl. Acad. Sci.* **109,** 1973–1978 (2012).

67. Binnig, G., Rohrer, H., Gerber, C. & Weibel, E. Surface Studies by Scanning Tunneling Microscopy. *Phys. Rev. Lett.* **49,** 57–61 (1982).

68. Binnig, G., Quate, C. & Gerber, C. Atomic Force Microscope. *Phys. Rev. Lett.* **56,** 930–933 (1986).

69. Alexander, S. *et al.* An atomic-resolution atomic-force microscope implemented using an optical lever. *J. Appl. Phys.* **65,** 164–167 (1989).

70. Tao, N. J., Lindsay, S. M. & Lees, S. Measuring the microelastic properties of biological material. *Biophys. J.* **63,** 1165–9 (1992).

71. Hutter, J. L. & Bechhoefer, J. Calibration of atomic-force microscope tips. *Rev. Sci. Instrum.* **64,** 1868–1873 (1993).

72. Cook, S. M. *et al.* Practical implementation of dynamic methods for measuring atomic force microscope cantilever spring constants. *Nanotechnology* **17,** 2135–2145 (2006).

73. Butt, H.-J. & Jaschke, M. Calculation of thermal noise in atomic force microscopy. *Nanotechnology* **6,** 1–7 (1995).

74. Walters, D. a. *et al.* Short cantilevers for atomic force microscopy. *Rev. Sci. Instrum.* **67,** 3583 (1996).

75. Proksch, R., Schäffer, T. E., Cleveland, J. P., Callahan, R. C. & Viani, M. B. Finite optical spot size and position corrections in thermal spring constant calibration. *Nanotechnology* **15,** 1344–1350 (2004).

76. Sader, J. E., Chon, J. W. M. & Mulvaney, P. Calibration of rectangular atomic force microscope cantilevers. *Rev. Sci. Instrum.* **70,** 3967 (1999).

77. Cleveland, J. P., Manne, S., Bocek, D. & Hansma, P. K. A nondestructive method for determining the spring constant of cantilevers for scanning force microscopy. *Rev. Sci. Instrum.* **64,** 403 (1993).

78. Stark, R. W., Drobek, T. & Heckl, W. M. Thermomechanical noise of a free v-shaped cantilever for atomic-force microscopy. *Ultramicroscopy* **86,** 207–215 (2001).

79. Te Riet, J. *et al.* Interlaboratory round robin on cantilever calibration for AFM force spectroscopy. *Ultramicroscopy* **111,** 1659–69 (2011).

80. Sneddon, I. N. The Relation Between Load and Penetration in the Axisymmetric Boussinesq Problem for a Punch of Arbitrary Profile. *Int. J. Eng. Sci.* **3,** 47–57 (1965).

81. Lin, D. C. & Horkay, F. Nanomechanics of polymer gels and biological tissues: A critical review of analytical approaches in the Hertzian regime and beyond. *Soft Matter* **4,** 669 (2008).

82. Hertz, H. Über die Berührung fester elastischer Körper. *J. für die reine und Angew. Math.* **171,** 156–171 (1882).

83. Akhremitchev, B. B. & Walker, G. C. Finite Sample Thickness Effects on Elasticity Determination Using Atomic Force Microscopy. *Langmuir* **15,** 5630–5634 (1999).

84. Sun, Y., Akhremitchev, B. & Walker, G. C. Using the Adhesive Interaction between Atomic Force Microscopy Tips and Polymer Surfaces to Measure the Elastic Modulus of Compliant Samples. *Langmuir* **20,** 5837–5845 (2004).

85. Briscoe, B. J., Sebastian, K. S. & Adams, M. J. The effect of indenter geometry on the elastic response to indentation. *J. Phys. D. Appl. Phys.* **27,** 1156–1162 (1994).

86. Crick, S. L. & Yin, F. C. P. Assessing micromechanical properties of cells with atomic force microscopy: Importance of the contact point. *Biomech. Model. Mechanobiol.* **6,** 199–210 (2007).

87. Guo, S. & Akhremitchev, B. B. Packing density and structural heterogeneity of insulin amyloid fibrils measured by AFM nanoindentation. *Biomacromolecules* **7,** 1630–1636 (2006).

88. Fuhrmann, A. *et al.* AFM stiffness nanotomography of normal, metaplastic and dysplastic human esophageal cells. *Phys. Biol.* **8,** 015007 (2011).

89. Kaushik, G., Fuhrmann, A., Cammarato, A. & Engler, A. J. In situ mechanical analysis of myofibrillar perturbation and aging on soft, bilayered Drosophila myocardium. *Biophys. J.* **101,** 2629–2637 (2011).

90. Roduit, C. *et al.* Stiffness tomography by atomic force microscopy. *Biophys. J.* **97,** 674–677 (2009).

91. Iyer, S., Gaikwad, R. M., Subba-Rao, V., Woodworth, C. D. & Sokolov, I. Atomic force microscopy detects differences in the surface brush of normal and cancerous cells. *Nat. Nanotechnol.* **4,** 389–393 (2009).

92. Dimitriadis, E. K., Horkay, F., Maresca, J., Kachar, B. & Chadwick, R. S. Determination of elastic moduli of thin layers of soft material using the atomic force microscope. *Biophys. J.* **82,** 2798–810 (2002).

93. Gavara, N. & Chadwick, R. S. Determination of the elastic moduli of thin samples and adherent cells using conical atomic force microscope tips. *Nat. Nanotechnol.* **7,** 733–6 (2012).

94. Li, Q. S., Lee, G. Y. H., Ong, C. N. & Lim, C. T. AFM indentation study of breast cancer cells. *Biochem. Biophys. Res. Commun.* **374,** 609–613 (2008).

95. Nikkhah, M., Strobl, J. S., Schmelz, E. M. & Agah, M. Evaluation of the influence of growth medium composition on cell elasticity. *J. Biomech.* **44,** 762–766 (2011).

96. Plodinec, M. *et al.* The nanomechanical signature of breast cancer. *Nat. Nanotechnol.* (2012). doi:10.1038/nnano.2012.167

97. Stewart, M. P. *et al.* Hydrostatic pressure and the actomyosin cortex drive mitotic cell rounding. *Nature* **469,** 226–230 (2011).

98. Webster, K. D., Crow, A. & Fletcher, D. A. An AFM-based stiffness clamp for dynamic control of rigidity. *PLoS One* **6,** (2011).

99. Webster, K. D., Ng, W. P. & Fletcher, D. A. Tensional homeostasis in single fibroblasts. *Biophys. J.* **107,** 146–155 (2014).

100. Mahaffy, R. E., Shih, C. K., MacKintosh, F. C. & Käs, J. Scanning probe-based frequency-dependent microrheology of polymer gels and biological cells. *Phys. Rev. Lett.* **85,** 880–883 (2000).

101. Alcaraz, J. *et al.* Microrheology of human lung epithelial cells measured by atomic force microscopy. *Biophys. J.* **84,** 2071–2079 (2003).

102. Smith, B. A., Tolloczko, B., Martin, J. G. & Grütter, P. Probing the viscoelastic behavior of cultured airway smooth muscle cells with atomic force microscopy: stiffening induced by contractile agonist. *Biophys. J.* **88,** 2994–3007 (2005).

103. Rother, J., Nöding, H., Mey, I. & Janshoff, A. Atomic force microscopy-based microrheology reveals significant differences in the viscoelastic response between malign and benign cell lines. *Open Biol.* **4,** 140046 (2014).

104. Bao, G. & Suresh, S. Cell and molecular mechanics of biological materials. *Nat. Mater.* **2,** 715–725 (2003).

105. Lim, C. T., Zhou, E. H. & Quek, S. T. Mechanical models for living cells--a review. *J. Biomech.* **39,** 195–216 (2006).

106. Lim, C. T., Zhou, E. H., Li, A., Vedula, S. R. K. & Fu, H. X. Experimental techniques for single cell and single molecule biomechanics. *Mater. Sci. Eng. C* **26,** 1278–1288 (2006).

107. Wang, N., Butler, J. P. & Ingber, D. E. Mechanotransduction across the cell surface and through the cytoskeleton. *Science* **260,** 1124–1127 (1993).

108. Bausch, A. R., Ziemann, F., Boulbitch, A. A., Jacobson, K. & Sackmann, E. Local measurements of viscoelastic parameters of adherent cell surfaces by magnetic bead microrheometry. *Biophys. J.* **75,** 2038–2049 (1998).

109. Wang, N. *et al.* Cell prestress. I. Stiffness and prestress are closely associated in adherent contractile cells. *Am. J. Physiol. Physiol.* **282,** C606–C616 (2002).

110. Hochmuth, R. M. Micropipette aspiration of living cells. *J. Biomech.* **33,** 15–22 (2000).

111. Mason, T., Ganesan, K., van Zanten, J., Wirtz, D. & Kuo, S. Particle Tracking Microrheology of Complex Fluids. *Phys. Rev. Lett.* **79,** 3282–3285 (1997).

112. Yamada, S., Wirtz, D. & Kuo, S. C. Mechanics of living cells measured by laser tracking microrheology. *Biophys. J.* **78,** 1736–1747 (2000).

113. Tseng, Y., Kole, T. P. & Wirtz, D. Micromechanical mapping of live cells by multiple-particle-tracking microrheology. *Biophys. J.* **83,** 3162–3176 (2002).

114. Wirtz, D. Particle-tracking microrheology of living cells: principles and applications. *Annu. Rev. Biophys.* **38,** 301–326 (2009).

115. Hale, C. M., Sun, S. X. & Wirtz, D. Resolving the role of actoymyosin contractility in cell microrheology. *PLoS One* **4,** (2009).

116. Mak, M., Kamm, R. D. & Zaman, M. H. Impact of Dimensionality and Network Disruption on Microrheology of Cancer Cells in 3D Environments. *PLoS Comput. Biol.* **10,** e1003959 (2014).

117. Neuman, K. C. & Block, S. M. Optical trapping. *Rev. Sci. Instrum.* **75,** 2787–2809 (2004).

118. Ashkin, A. Acceleration and Trapping of Particles by Radiation Pressure. *Phys. Rev. Lett.* **24,** 156–159 (1970).

119. Ashkin, A., Dziedzic, J. M., Bjorkholm, J. E. & Chu, S. Observation of a single-beam gradient force optical trap for dielectric particles. *Opt. Lett.* **11,** 288 (1986).

120. Ashkin, A. & Dziedzic, J. M. Optical trapping and manipulation of viruses and bacteria. *Science* **235,** 1517–1520 (1987).

121. Ashkin, A., Dziedzic, J. M. & Yamane, T. Optical trapping and manipulation of single cells using infrared laser beams. *Nature* **330,** 769–771 (1987).

122. Meiners, J. C. & Quake, S. R. Femtonewton force spectroscopy of single extended DNA molecules. *Phys. Rev. Lett.* **84,** 5014–5017 (2000).

123. Dao, M., Lim, C. T. & Suresh, S. Mechanics of the human red blood cell deformed by optical tweezers. *J. Mech. Phys. Solids* **51,** 2259–2280 (2003).

124. Lim, C. T., Dao, M., Suresh, S., Sow, C. H. & Chew, K. T. Large deformation of living cells using laser traps. *Acta Mater.* **52,** 1837–1845 (2004).

125. Guck, J., Ananthakrishnan, R., Moon, T. J., Cunningham, C. C. & Käs, J. Optical deformability of soft biological dielectrics. *Phys. Rev. Lett.* **84,** 5451–5454 (2000).

126. Guck, J. *et al.* The optical stretcher: a novel laser tool to micromanipulate cells. *Biophys. J.* **81,** 767–784 (2001).

127. Guck, J. *et al.* Optical deformability as an inherent cell marker for testing malignant transformation and metastatic competence. *Biophys. J.* **88,** 3689–3698 (2005).

128. Otto, O. *et al.* Real-time deformability cytometry: on-the-fly cell mechanical phenotyping. *Nat. Methods* **12,** 199–202 (2015).

129. Gossett, D. R. *et al.* Hydrodynamic stretching of single cells for large population mechanical phenotyping. *Proc. Natl. Acad. Sci.* **109,** 7630–7635 (2012).

130. Tan, J. L. *et al.* Cells lying on a bed of microneedles: an approach to isolate mechanical force. *Proc. Natl. Acad. Sci. U. S. A.* **100,** 1484–1489 (2003).

131. Du Roure, O. *et al.* Force mapping in epithelial cell migration. *Proc. Natl. Acad. Sci. U. S. A.* **102,** 2390–2395 (2005).

132. Dhaliwal, R. S. & Rau, I. S. The Axisymmetric Boussinesq Problem for a Thick Elastic Layer Under a Punch of Arbitrary Profile. *Int. J. Eng. Sci.* **8,** 843–856 (1970).

133. Sandersius, S. A. & Newman, T. J. Modeling cell rheology with the Subcellular Element Model. *Phys. Biol.* **5,** 015002 (2008).

134. Sandersius, S. A., Weijer, C. J. & Newman, T. J. Emergent cell and tissue dynamics from subcellular modeling of active biomechanical processes. *Phys. Biol.* **8,** 045007 (2011).

135. Newman, T. J. Modeling multicellular systems using subcellular elements. *Math. Biosci. Eng.* **2,** 613–624 (2005).

136. Zhao, G. F., Fang, J. & Zhao, J. A 3D distinct lattice spring model for elasticity and dynamic failure. *Int. J. Numer. Anal. Methods Geomech.* **35,** 859–885 (2011).

137. Costa, K. D. Single-cell elastography: Probing for disease with the atomic force microscope. *Dis. Markers* **19,** 139–154 (2003).

138. Azeloglu, E. U., Kaushik, G. & Costa, K. D. Developing a hybrid computational model of AFM indentation for analysis of mechanically heterogeneous samples. in *Proc. 31st Annu. Int. Conf. IEEE Eng. Med. Biol. Soc.* 4273–4276 (2009). doi:10.1109/IEMBS.2009.5334043

139. Atkinson, K. E. & Shampine, L. F. Algorithm 876 : Solving Fredholm Integral Equations of the Second Kind in MATLAB. *ACM Trans. Math. Softw.* **34,** 21 (2008).

140. Poincloux, R. *et al.* Contractility of the cell rear drives invasion of breast tumor cells in 3D Matrigel. *Proc. Natl. Acad. Sci. U. S. A.* **108,** 1943–1948 (2011).

141. Koch, T. M., Münster, S., Bonakdar, N., Butler, J. P. & Fabry, B. 3D traction forces in cancer cell invasion. *PLoS One* **7,** (2012).

142. Carey, S. P., Starchenko, A., McGregor, A. L. & Reinhart-King, C. A. Leading malignant cells initiate collective epithelial cell invasion in a three-dimensional heterotypic tumor spheroid model. *Clin. Exp. Metastasis* **30,** 615–630 (2013).

143. Riching, K. M. *et al.* 3D Collagen Alignment Limits Protrusions to Enhance Breast Cancer Cell Persistence. *Biophys. J.* **107,** 2546–2558 (2014).

144. Provenzano, P. P., Inman, D. R., Eliceiri, K. W., Trier, S. M. & Keely, P. J. Contact guidance mediated three-dimensional cell migration is regulated by Rho/ROCK-dependent matrix reorganization. *Biophys. J.* **95,** 5374–5384 (2008).

145. Pillé, J. Y. *et al.* Anti-RhoA and Anti-RhoC siRNAs inhibit the proliferation and invasiveness of MDA-MB-231 breast cancer cells in vitro and in vivo. *Mol. Ther.* **11,** 267–274 (2005).

146. Wang, Y.-L. & Pelham, R. J. J. Preparation of a Flexible, Porous Polyacrylamide Substrate for Mechanical Studies of Cultured Cells. *Methods Enzymol.* **298,** 489–496 (1998).

147. Schulz, O. *et al.* Tip induced fluorescence quenching for nanometer optical and topographical resolution. *Opt. Nanoscopy* **2,** 1 (2013).

148. Andriotis, O. G. *et al.* Nanomechanical assessment of human and murine collagen fibrils via atomic force microscopy cantilever-based nanoindentation. *J. Mech. Behav. Biomed. Mater.* **39,** 9–26 (2014).

149. Sokolov, I., Kalaparthi, V., Kreshchuk, M. & Dokukin, M. E. On averaging force curves over heterogeneous surfaces in atomic force microscopy. *Ultramicroscopy* **121,** 16–24 (2012).

150. Zink, D., Fischer, A. H. & Nickerson, J. A. Nuclear structure in cancer cells. *Nat. Rev. Cancer* **4,** 677–687 (2004).

151. Liu, H. *et al.* In situ mechanical characterization of the cell nucleus by atomic force microscopy. *ACS Nano* **8,** 3821–8 (2014).

152. Krause, M., Te Riet, J. & Wolf, K. Probing the compressibility of tumor cell nuclei by combined atomic force-confocal microscopy. *Phys. Biol.* **10,** 065002 (2013).

153. Nandakumar, V., Kelbauskas, L., Johnson, R. & Meldrum, D. Quantitative characterization of preneoplastic progression using single-cell computed tomography and three-dimensional karyometry. *Cytom. Part A* **79 A,** 25–34 (2011).

154. Tse, J. R. & Engler, A. J. Preparation of hydrogel substrates with tunable mechanical properties. *Curr. Protoc. Cell Biol.* (2010). doi:10.1002/0471143030.cb1016s47

APPENDIX A

SNEDDON'S PROCEDURE AND DERIVATION OF SPHERO-CONICAL PROBES FOR ELASTIC INDENTENTATION

For an axisymmetric indentation on an elastic, homogeneous, isotropic half-space, the stress-strain relationships are[80]

$$\sigma_{zz} = (2\mu + \lambda)\frac{\partial u_z}{\partial z} + \lambda\left(\frac{\partial u_r}{\partial r} + \frac{u_r}{r}\right) \tag{A1}$$

$$\sigma_{rz} = \mu\left(\frac{\partial u_r}{\partial z} + \frac{\partial u_z}{\partial r}\right) \tag{A2}$$

Where **σ** is the stress, **u** is the strain, and μ and λ are Lamé constants, and the boundary conditions are

$$u_z(r,0) = \delta - f\left(\frac{r}{a}\right), 0 \le r \le a \tag{A3}$$

$$\sigma_{zz}(r,0) = 0, r > a \tag{A4}$$

$$\sigma_{rz}(r,0) = 0, r \ge 0 \tag{A5}$$

Eq. (A3) states that the displacement is equal to the difference in the indentation depth δ and shape function of the indenter *f(r)*, while Eqs. (A4-A5) describe the surface forces of the elastic medium inside and outside of the contact radius *a* of the indenter. For a bonded two-layer problem, additional boundary conditions are employed stating there is no difference in stress or displacement for any component on either side of the boundary[132]. Sneddon demonstrated the solution to Eqs. (A1-A5) demonstrated that the force and indentation depths may be analytically calculated by solving the following equations[80]:

$$\beta(t) = t\int_0^t \frac{f'(r)}{\sqrt{t^2 - r^2}}dr \tag{A6}$$

$$\delta = \beta(1) \tag{A7}$$

$$F = \frac{2Ea}{(1-\nu^2)}\left(\delta - \int_0^1 \beta(t)dt\right) \tag{A8}$$

using

$$\frac{d}{dt}\int_0^t \frac{x}{\sqrt{t^2 - x^2}}dx = 1 \tag{A9}$$

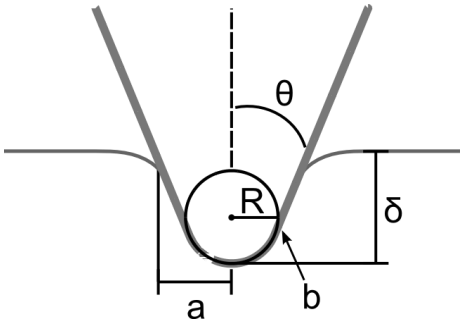

Figure A-1: Geometry of the sphero-conical indenter.

For this derivation, all integrals are solved using Wolfram Mathematica. Using Eqs. (A6-A8), the Hertz model may be computed by using a parabolic tip shape function. For a sphero-conical tip, we define *f(r)* as follows:

$$b_{SC} = R\cos\theta \tag{A10}$$

$$f_{SC}(r \le b_{SC}) = R - \sqrt{R^2 - r^2}$$

$$f_{SC}(r \ge b_{SC}) = (r - b_{SC})\cot\theta + R - \sqrt{R^2 - {b_{SC}}^2} \tag{A11}$$

We need to make transform *r* to the radius normalized to the contact radius such that 0<*r*<1. Next, we solve for β in two separate regimes:

$$\beta(t; t \le b_{SC}/a) = t\int_0^t \frac{f'_{SC}(ra)}{\sqrt{t^2 - r^2}}dr = \frac{1}{2}at\ln\left(\frac{R+at}{R-at}\right) \tag{A12}$$

$$\beta(t; t > b_{SC}/a) = t\int_0^{b_{SC}/a} \frac{f'_{SC}(ra)}{\sqrt{t^2 - r^2}}dr + t\int_{b_{SC}/a}^t \frac{f'_{SC}(ra)}{\sqrt{t^2 - r^2}}dr$$

$$= at\ln\left(\frac{R+at}{\sqrt{R^2 - {b_{SC}}^2} + \sqrt{a^2t^2 - {b_{SC}}^2}}\right) \tag{A13}$$

$$+ at\cos^{-1}\left(\frac{b_{SC}}{at}\right)\cot\theta$$

Once β is known, we can solve for the indentation depth:

$$\delta(a \le b_{SC}) = \beta(1) = \frac{1}{2}a\ln\left(\frac{R+a}{R-a}\right) \tag{A14}$$

$$\delta(a > b_{SC}) = \beta(1)$$

$$= a\ln\left(\frac{R+a}{\sqrt{R^2 - {b_{SC}}^2} + \sqrt{a^2 - {b_{SC}}^2}}\right) \tag{A15}$$

$$+ a\cos^{-1}\left(\frac{b_{SC}}{a}\right)\cot\theta$$

Next, we solve for the force:

$$F(a \le b_{SC}) = \frac{2Ea}{(1-\nu^2)}\left(\delta - \int_0^1 \beta(t; t \le b/a)dt\right)$$

$$= \frac{E}{(1-\nu^2)}\left[\frac{1}{2}(a^2 + R^2)\ln\left(\frac{R+a}{R-a}\right) - aR\right] \tag{A16}$$

$$F(a > b_{SC}) = \frac{2Ea}{(1-\nu^2)}\left(\delta - \int_0^1 \beta(t)dt\right)$$

$$= \frac{2Ea}{(1-\nu^2)}\left(\delta - \int_0^{b_{SC}/a} \beta\left(t; t \le \frac{b_{SC}}{a}\right)dt \right.$$

$$\left. - \int_{b_{SC}/a}^1 \beta\left(t; t > \frac{b_{SC}}{a}\right)dt\right)$$

$$= \frac{E}{(1-\nu^2)}\left[a^2 \cot\theta \cos^{-1}\left(\frac{b_{SC}}{a}\right) + b_{SC}\cot\theta\sqrt{a^2 - {b_{SC}}^2} - aR + \right. \tag{A17}$$

$$\sqrt{\left(R^2 - {b_{SC}}^2\right)\left(a^2 - {b_{SC}}^2\right)} + a^2 \ln\left(\frac{R+a}{\sqrt{R^2-{b_{SC}}^2}+\sqrt{a^2-{b_{SC}}^2}}\right) -$$

$$\left.\frac{R^2}{2}\ln\left(\frac{a^2R^2 - \left({b_{SC}}^2 - \sqrt{\left(R^2-{b_{SC}}^2\right)\left(a^2-{b_{SC}}^2\right)}\right)^2}{{b_{SC}}^2(R+a)^2}\right)\right]$$

Thus, λ_{SC} is the terms in square brackets in Eqs. (A16-17).

APPENDIX B

DERIVATION OF TWO-LAYER EMPIRICAL SERIES APPROXIMATION FOR PARABOLIC AND CONICAL INDENTERS

The force of an indentation on a two-layer material is approximated as

$$F \approx F_0 e^{\xi(\alpha,\gamma)} \tag{B1}$$

$$\xi = \left(\xi_{\alpha\beta}\alpha\gamma + \frac{1}{2}\xi_{\alpha\alpha\beta}\alpha^2\gamma + \frac{1}{2}\xi_{\alpha\beta\beta}\alpha\gamma^2 + \frac{1}{6}\xi_{\alpha\alpha\alpha\beta}\alpha^3\gamma + \frac{1}{4}\xi_{\alpha\alpha\beta\beta}\alpha^2\gamma^2 + \frac{1}{6}\xi_{\alpha\beta\beta\beta}\alpha\gamma^3 + \cdots\right) \tag{B2}$$

where F_0 is the force of the homogeneous case. The exponential function was chosen for two reasons: the corrected force does not become negative, and it provides a better fit for the series expansion, as ξ takes a sigmoidal shape. The subscripts in ξ indicate partial derivatives. Only the cross-terms matter as both an elastic mismatch and layer height are required for the two-layer theory to be applicable. γ was chosen as a base-10 logarithm so that the magnitude of γ would be less than 1 for two orders of magnitude in the substrate. The values for ξ are shown in Figure B-1. The partial derivatives are calculated from this using the finite difference method with accuracy order 4 and meshes of 0.05 in α and 0.20 in γ.

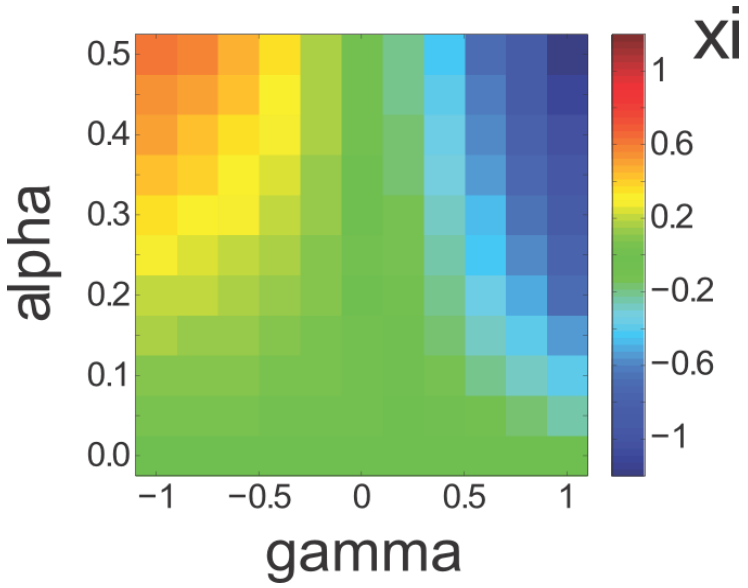

Figure B-1: Solution to the integral transform equations for ξ used in the series approximation. α and γ are adjusted and the series expansion is centered around (0,0). The coefficients in the series approximation are computed using the finite difference method.

APPENDIX C

PROTOCOL FOR TWO-LAYER CORRECTION USING MATLAB

Two-layer analysis protocol

Last update: 2015-04-20 BLD

Requirements

MATLAB (R2012a and R2013b confirmed works)
The AFM analysis package in the Ros lab
The Fie software package for solving Fredholm Integral Equations of the Second Kind [http://dl.acm.org/citation.cfm?id=1377601, Atkinson, K.E. & Shampine, L.F. Algrorithm 876: Solving Fredholm Integral Equations of the Second Kind in MATLAB. *ACM Trans. Math. Softw.* 34, **21** (2008)]

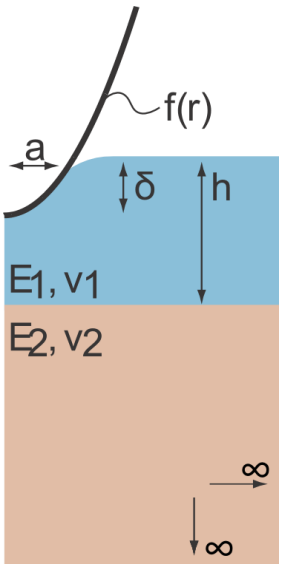

Theory, Introduction

Standard analysis of AFM data (e.g. the Hertz model) assumes elastic homogeneity in the sample, however this is rarely true with biological samples.

Sneddon [Sneddon, *Int. J. Eng. Sci.* **3**, 47-57 (1965)] originally solved the axisymmetric elastic indentation problem for a homogeneous sample for an indenter shape that simply follows some function f(r). These are derived from elastic equilibrium conditions, and assume an infinite, homogeneous, elastic, isotropic half-space and frictionless tip-sample interaction.

Dhaliwal and Rau [Dhaliwal and Rau, *Int. J. Engng. Sci.* **8**, 854-856 (1970)] extended this solution using the same assumptions, however now it is a bonded (no-slip) two-layer material, as shown in the cartoon.

The equations are:

$$\phi(t) + \frac{a}{h\pi}\int_0^1 K(x,t)\,\phi(x)dx = -\frac{E_1 a}{2(1-{\nu_1}^2)}[\delta - \beta(t)] \quad (1)$$

$$F = -4\int_0^1 \phi(t)dt \quad (2)$$

$$\phi(1) = 0 \quad (3)$$

$$\beta(t) = t\int_0^t \frac{f'(r)}{\sqrt{t^2 - r^2}}dr \quad (4)$$

$$K(x,t) = 2\int_0^\infty H(2u)\cos\left(\frac{a}{h}tu\right)\cos\left(\frac{a}{h}xu\right)du \quad (5)$$

$$H(u) = -\frac{d + g(1+u)^2 + 2dge^{-u}}{e^u + d + g(1+u^2) + dge^{-u}} \quad (6)$$

$$d = \frac{(3-4\nu_1) - \mu(3-4\nu_2)}{1 + \mu(3-4\nu_2)} \quad (7)$$

$$g = \frac{1-\mu}{\mu + 3 - 4\nu_1} \tag{8}$$

$$\mu = \frac{E_1(1+\nu_2)}{E_2(1+\nu_1)} \tag{9}$$

It's a bit of an equation dump, but the strategy for solving is to numerically solve (1) and (3) to determine the contact radius, then when that is known solve (1) and (2). When the integral term in (1) is zero (e.g. if h=inf or μ=1), then it is identically reduced to the homogeneous case derived by Sneddon.

The strategy for correcting for the substrate will be this: build up a table of "scaling values" from solving the above equations for a force-curve and fitting for the Young's modulus.

So in the experiment, if we know the height of the top layer and Young's modulus of the bottom layer, we can interpolate from the scaling values to correct the Young's modulus we normally get from fitting the curve on the two-layer sample.

The program `dhaliwal_rau` generates a force-indentation curve on a two-layer material. Instructions to run it are in `dhaliwal_rau.m`. It is nice to make some curves and fit them to see how the force response changes when the parameters are adjusted.

Procedure

1. Build a table of correction values

You will need to know the indenter geometry (type, radius, half-angle), need to use a fixed indentation depth for the fitting (e.g. 0-1μm), and need some guess at the Poisson ratio for both layers (0.5, 0.5?).

For example, to make a correction table for a bead indenter with radius 5μm, the sample heights range from 4μm to 30μm, the mismatches span an order of magnitude in each direction, the Poisson's ratios are both 0.5, and the indentation bin is 0-1μm, then run the following:

```
[V,X,Y]=twolayer_correction_table('parabolic',2.7e-
6,1,logspace(-1,1,21),4e-6:1e-6:20e-6,0,1e-6,0.5,0.5);
```

This will make the table. More instructions for the parameters are in the file `twolayer_correction_table.m`.

2. Apply the table of correction values

The scaling value may be computed with (mu is the mismatch, h is the sample height):

```
scale=interp2(X,Y,V,mu,h);
```

Multiply the E value you get from normal fitting by this, and you have corrected for the substrate.

MATLAB function headers

dhaliwal_rau.m

```
function [fc, as]=dhaliwal_rau(E1,nu1,E2,nu2,h,r,theta,type,mesh)
% Input parameters -- SI units [Pa,m,radians]:
%  E1: the Young's modulus of the top layer
%  nu1: the Poisson's ratio of the top layer
%  E2: the Young's modulus of the bottom layer
%  nu2: the Poisson's ratio of the bottom layer
%  h: the height of the top layer
%  r: the radius of the indenter probe (does not matter for conical)
%  theta: the half-angle of the indenter probe, units are radians
%  type: the indenter probe geometry type, supported types:
%       parabolic: Hertz model
%       conical: Sneddon model
%       hyperbolic: a hyperbola
%       briscoe: Briscoe's blunted cone model
%       spherocone: sphrical tip, transitions to cone continuosly
%       cylindrical: a cylinder
%       sphere: a sphere
%  mesh: indentation points at which the forces will be calcualated
% Output parameters -- SI units [m,Pa]:
%  fc: force-indentation curve, fc.ext is a n-by-2 array
[indentation,F]
%  as: contact radius, n-by-2 arrray [indentation,a]
```

twolayer_correction.m

```
function [V, X, Y]=twolayer_correction_table (type, r, theta, mus, hs,
d_min, d_max, nu1, nu2)
% Input parameters -- SI units [Pa,m,radians]:
%  type: the indenter probe geometry type, supported types:
%       parabolic: Hertz model
%       conical: Sneddon model
%       hyperbolic: a hyperbola
%       briscoe: Briscoe's blunted cone model
%       spherocone: sphrical tip, transitions to cone continuosly
%       cylindrical: a cylinder
%       sphere: a sphere
%  r: the radius of the indenter
%  theta: the half-angle of the indenter
%  mus: array of elastic mismatches to build the table from
%  hs: array of heights to build the tables from
%  d_min: minimum indentation depth
%  d_max: maximum indentation depth
%  nu1: top layer Poisson's ratio
%  nu2: bottom layer Poisson's ratio
% Output parameters -- SI units [m,Pa]:
%  V: table of correction values, size is length(hs)-by-length(mus)
%  X: mus
%  Y: hs'
```

dd_fit.m

```
function [E, X, r2]=dd_fit(curve, contact, r, theta, nu, binning, type,
min_ind, max_ind)
% Input parameters:
%  curve: the force curve
%  contact: the contact point
%  r: the tip radius
%  theta: axisymmetric semi-vertical tip angle
%  nu: Poisson ratio
%  binning: bins for depth-dependent analysis
%  type: the indenter probe geometry type, supported types:
%       parabolic: Hertz model
%       conical: Sneddon model
%       hyperbolic: a hyperbola
%       briscoe: Briscoe's blunted cone model
%       spherocone: sphrical tip, transitions to cone continuosly
%       cylindrical: a cylinder
%       sphere: a sphere
%  min_ind: Minimum indentation depth
%  max_ind: Maxiumum indentation depth
% Output parameters
%  E: the depth-dependent Young's modulus
%  X: the indentation value so plot(X,E) works
%  r2: the r^2 value from the fit
```

Examples

Example 1: Generate a simulated force-indentation curve of a Hertz model indenter on two-layer material with E_1=1kPa, E_2=3kPa, h=10µm, R=5µm, $\nu_1=\nu_2$=0.5, indentation depth up to 2µm with 10nm mesh, then perform a depth-dependent fit:

```
fc=dhaliwal_rau(1e3,0.5,3e3,0.5,10e-6,5e-
6,0,'parabolic',0:1e-8:2e-6); % first simulate the curve
E=dd_fit(fc,0,5e-6,0,0.5,250e-9,'parabolic') % then fit it
```

Example 2: Two-layer correction for an experiment with a constant probe with radius 2.7µm, constant indentation depths from 0-500nm, and the heights and E_2 values are measured independently. Mismatches are an order of magnitude at most, heights range from 4-20µm. Poisson's ratio is always assumed to be 0.5.

Step 1: Build up a table of correction values

```
[V,X,Y]=twolayer_correction_table('parabolic',2.7e-
6,1,logspace(-1,1,21),4e-6:1e-6:20e-6,0,500e-9,0.5,0.5);
```

Step 2: Fit the force-indentation curve for the top layer, and bottom layer, set the height

```
E1=dd_fit(fc1,contact1,2.7e-6,1,0.5,500e-
9,'parabolic',0,500e-9);
E2=dd_fit(fc2,contact2,2.7e-6,1,0.5,500e-
9,'parabolic',0,500e-9);
h=15e-6;
```

Step 3: Apply the correction

```
E1_adjusted=E1*interp2(X,Y,V,E1/E2,h);
```

`E1_adjusted` is the substrate-corrected Young's modulus for the top layer.

APPENDIX D

SELECT MATLAB PROGRAMS FOR FORCE-INDENTATION CURVE ANALYSIS

dd_fit.m

```
% dd_fit.m
%
% Depth-dependent force curve fitting
% Input parameters:
%  curve: the force curve
%  contact: the contact point
%  r: the tip radius
%  theta: axisymmetric semi-vertical tip angle
%  nu: Poisson ratio
%  binning: bins for depth-dependent analysis
%  type: the indenter probe geometry type, supported types:
%       parabolic: Hertz model
%       conical: Sneddon model
%       hyperbolic: a hyperbola
%       briscoe: Briscoe's blunted cone model
%       spherocone: sphrical tip, transitions to cone continuosly
%       cylindrical: a cylinder
%       sphere: a sphere
%  min_ind: Minimum indentation depth
%  max_ind: Maxiumum indentation depth
% Output parameters
%  E: the depth-dependent Young's modulus
%  X: the indentation value so plot(X,E) works
%  r2: the r^2 value from the fit

function [E, X, r2] = dd_fit(curve, contact, r, theta, nu, binning, type,
min_ind, max_ind)

if nargin < 9
    min_ind = 0;
    max_ind = 1000;
end

% Pre-process the force curve, truncate the baseline and shift
% everything to zero
index = get_index(curve.ext(:,1),contact);
index2 = get_index(curve.ext(:,1),contact + max_ind);
ext = curve.ext(index:index2, :);
ext(:,1) = ext(:,1) - min(ext(:,1)) + eps;
ext(:,2) = ext(:,2) - min(ext(:,2)) + eps;
% ext(:,2) = ext(:,2) - ext(1,2) + eps;
fc = curve;
fc.ext = ext;
index3 = get_index(fc.ext(:,1), min_ind);
ext2(:,1) = ext(index3:end,1);
ext2(:,2) = ext(index3:end,2);
fc.ext = ext2;
ext = ext2;

% Initialize storage for contact radii and lambda terms
as = [];
lams = [];

if length(ext) < 3
    E = NaN;
    r2 = NaN;
    return
end
```

```
% Iterate over indentation depths
for i=1:length(ext)
    d = ext(i,1);
    if strcmp(type,'parabolic')
        a = sqrt(r*d);
        lam = (4/3) * sqrt(r) * d^(3/2);
    elseif strcmp(type,'conical')
        a = 2*d/(pi*cot(theta));
        lam = (1/2) * a^2 * pi * cot(theta);
    elseif strcmp(type,'hyperbolic')
        f = @(a) real(d - (a*cot(theta)/2) * (pi/2 + atan(a/(2*r*cot(theta)) -
r*cot(theta)/(2*a))));
        a = sqrt(r*d);
        a = fzero(f,a);
        z = r*cot(theta)/a;
        lam = (a^3/r)*(z^2 + (z/2)*(1-z^2)*(pi/2 + atan(1/(2*z)-(z/2))));
    elseif strcmp(type,'briscoe')
        b = r * cos(theta);
        m = 1/2;
        n = 1;
        f = @(a) real((ext(i,1) + (a/r)*((a^2-b^2)^(1/2)-a) - ...
                 (n*a/tan(theta))*((pi/2)-asin(b/a))));
        a = sqrt(r*ext(i,1));
        a = fzero(f,a);
        lam = 2 * (a*d - (m*a^2/tan(theta))*(pi/2 - asin(b/a)) ...
            - a^3/(3*r) + ((a^2-b^2)^(1/2))*(m*b/tan(theta)+(a^2-b^2)/(3*r)));
    elseif strcmp(type,'rico')
        b = r * cos(theta);
        m = sqrt(2)/pi;
        n = 2^(3/2)/pi;
        f = @(a) real((ext(i,1) + (a/r)*((a^2-b^2)^(1/2)-a) - ...
                 (n*a/tan(theta))*((pi/2)-asin(b/a))));
        a = sqrt(r*ext(i,1));
        a = fzero(f,a);
        lam = 2 * (a*d - (m*a^2/tan(theta))*(pi/2 - asin(b/a)) ...
            - a^3/(3*r) + ((a^2-b^2)^(1/2))*(m*b/tan(theta)+(a^2-b^2)/(3*r)));
    elseif strcmp(type,'spherocone')
        b = r*cot(theta) / sqrt(1+cot(theta)^2);
        f = @(a) real(ext(i,1) - ((1 <= b/a) * (1/2)*a*log((r+a)/(r-a)) ...
            + (1 > b/a) * (a*log((r+a)/(sqrt(r^2-b^2)+a*sqrt(1-(b/a)^2))) +
a*acos(b/a)*cot(theta))));
        a = sqrt(r*ext(i,1)+1e-9);
        a = fzero(f,a);
        lam = (1<=b/a) * ((1/2)*(a^2+r^2)*log((r+a)/(r-a))-r*a) + ...
              (1> b/a) * (2*a)*(ext(i,1)-(b*r/(2*a)+(b^2-
r^2)/(4*a)*log((r+b)/(r-b))+(1/2)*a*cot(theta)*acos(b/a)-
(1/2)*b*cot(theta)*sqrt(1-b^2/a^2)+1/(4*a)*(-2*a*sqrt((1-b^2/a^2)*(r^2-
b^2))+2*a*r-2*b*r-b^2*log((r+b)/(r-b))+2*a^2*log((r+a)/(sqrt(r^2-b^2)+a*sqrt(1-
b^2/a^2)))+r^2*log((a^2/b^2*(b+r)^2*(r+b^2/a-sqrt((r^2-b^2)*(1-b^2/a^2)))*(r-
b^2/a+sqrt((r^2-b^2)*(1-b^2/a^2))))/((a+r)^2*(r^2-b^2))))));
    elseif strcmp(type,'lin-nh')
        a = sqrt(r*d);
        lam = 20/(9*pi) * pi * (a^5-15*r*a^4+75*r^2*a^3) / (5*r*a^2-
50*r^2*a+125*r^3);
    elseif strcmp(type,'cylindrical')
        a = r;
        lam = 2 * a * d;
    elseif strcmp(type, 'parabocone')
        b = r * cot(theta);
        f = @(a) real(ext(i,1) - ((1 < b/a) * (a^2/r) ...
            + (1 > b/a) * (a^2/r * (1-sqrt(1-b^2/a^2)) +
a*acos(b/a)*cot(theta))));
```

```
        a = sqrt(r*ext(i,1));
        a = fzero(f,a);
        lam = (1<=b/a) * (2 * a * (d - a^2/(3*r))) ...
            + (1> b/a) * (2 * a * (d - a^2/(3*r)*(1-sqrt(1-
b^2/a^2)+b^2/a^2*sqrt(1-b^2/a^2)) + 1/2*a*(b/a*sqrt(1-b^2/a^2)-
acos(b/a))*cot(theta)));
    elseif strcmp(type, 'dimitriadis-bonded')
        height = 5.1e-3;
        a = sqrt(r*d);
        a0 = -(1.2876 - 1.4678*nu + 1.3442*nu^2)/(1-nu);
        b0 =  (0.6387 - 1.0277*nu + 1.5164*nu^2)/(1-nu);
        c = sqrt(r*d)/height;
        lam = (4/3) * sqrt(r) * d^(3/2) * (1 - 2*a0*c/pi + 4*a0^2*c^2/(pi^2) -
8/(pi^3)*(a0^3+4*pi^2*b0/15)*c^3 + 16*a0/(pi^4)*(a0^3+3*pi^2*b0/5)*c^4);
    elseif strcmp(type, 'dimitriadis-nonbonded')
        height = -contact;
        a = sqrt(r*d);
        a0 = -0.347 * (3-2*nu)/(1-nu);
        b0 =  0.056 * (5-2*nu)/(1-nu);
        c = sqrt(r*d)/height;
        if c > 1
            disp('warning: chi > 1')
        end
        lam = (4/3) * sqrt(r) * d^(3/2) * (1 - 2*a0*c/pi + 4*a0^2*c^2/(pi^2) -
8/(pi^3)*(a0^3+4*pi^2*b0/15)*c^3 + 16*a0/(pi^4)*(a0^3+3*pi^2*b0/5)*c^4);
    end
    as = [as real(a)];
    lams = [lams real(lam)];

end
max_ind = ext(end,1);
nbins = max(floor(max_ind/binning - min_ind/binning),1);

for i=1:nbins
    % Find first point, last point
    first = get_index(fc.ext(:,1), binning*(i-1)+min_ind);
    last = get_index(fc.ext(:,1), binning*i+min_ind);
    % Fit the model data to a power-law
    [fitobj,gof] = fit_power1(fc.ext(first:last,1), lams(first:last)');
    A = fitobj.a;
    B = fitobj.b;
    % Linearize the experimental data
    ext_lin = ext(first:last,:);
    ext_lin(:,2) = ext_lin(:,2).^(1/B);
    % Fit linearized curve to a y=mx+b
    [fitobj2,gof2] = fit_poly1(ext_lin(:,1), ext_lin(:,2));
    C = fitobj2.p1;
    % Calculate the Young's modulus
    E(i) = C^(B) * (1-nu^2) / A;

    % Optional: plot the linear fit versus the linearized curve
%     plot(ext_lin(:,1), ext_lin(:,2), 'Color', 'red')
%     hold on
%     plot(ext_lin(:,1), ext_lin(:,1).*fitobj2.p1 + fitobj2.p2, 'Color',
'blue');

    % Calculate the error from fitting
    sa = gof.a_se;
    sb = gof.b_se;
    sc = gof2.p1_se;
    dF = abs(fc.ext(first,2) - fc.ext(last,2));
    s1(i)=E(i)^2*sa^2/A^2;
```

```
    s2(i)=E(i)^2 * log(C)^2*sb^2;
    s3(i) = 0;
    %s3(i)=E(i)^2*log(dF)^2*sb^2/B^2;
    s4(i)=B^2*E(i)^2*sc^2/C^2;
    s(i) = sqrt(s1(i) + s2(i) + s3(i) + s4(i));

    % Optional: Adjust the E until residual (RMSE) is minimized
%     Ei = E(i);
%     points = 10000;
%     for j=-points:points
%         Et = Ei + Ei*j*.0004;
%         ext_predicted = [ext(first:last,1) (Et/(1-nu^2)).*lams(first:last)'];
%         residual = sqrt(sum((ext_predicted(:,2)-ext(first:last,2)).^2));
%         resids(j+points+1,:) = [Et residual];
%     end
%     [~,j] = min(resids(:,2));
%     Et = resids(j,1);
%     E(i) = Et;

    % Calculate r2
    Favg = mean(fc.ext(first:last,2));
    Fpred = E(i)./(1-nu.^2).*lams(first:last)';
    Fpred = Fpred - (mean(Fpred)-mean(fc.ext(first:last,2)));
    sstot = sum((fc.ext(first:last,2) - Favg).^2);
    ssres = sum((fc.ext(first:last,2) - Fpred).^2);
    r2(i)=(1-ssres/sstot);
%     plot(fc.ext(first:last,1), fc.ext(first:last,2));
%     hold on
%     plot(fc.ext(first:last,1).*1e6, Fpred.*1e9);
end

X = min_ind+binning/2:binning:max_ind-binning/2;

% Optional: plot the results
% x = min_ind+binning/2:binning:max_ind-binning/2;
% E = E(1:end) .* 1e-3;
% x = x(1:end) .* 1e6;
% s = s(1:end) .* 1e-3;
% errorbar(x,E,s,'LineWidth',1);
% set(gca, 'FontSize', 12)
% xlabel('Indentation (\mum)')
% ylabel('Apparent Youngs Modulus (kPa)')
% %hold all
% E = E * 1e3;
% fc.ext(:,1) = fc.ext(:,1) * 1e-6;
% fc.ext(:,2) = fc.ext(:,2) * 1e-9;

% Optional: plot results with force curve in plotyy style
% x = min_ind+binning/2:binning:max_ind-binning/2;
% E = real(E);
% for i=length(x):-1:1
%     if E(i) < 0
%         E(i) = [];
%         x(i) = [];
%         s(i) = [];
%     end
% end
% E = E(1:end) .* 1e-3;
% x = x(1:end) .* 1e6;
% s = s(1:end) .* 1e-3;
% fc.ext(:,1) = fc.ext(:,1) * 1e6;
% fc.ext(:,2) = fc.ext(:,2) * 1e9;
```

```
% [ax,h1,h2] = plotyy(fc.ext(:,1),fc.ext(:,2),x,E, ...
%             @(x,y)plot(x,y,'LineWidth',3,'Color','red'), ...
%             @(x,E)errorbar(x,E,s,'LineWidth',3,'Color','blue'));
% axis(ax(1),[eps max(fc.ext(end,1)) eps max(fc.ext(:,2))])
% %axis(ax(1),[eps max(fc.ext(end,1)) eps 100])
% % axis(ax(1),[0 10 0 16])
% axis(ax(2),[eps max(fc.ext(end,1)) min(E)-max(s) max(E)+max(s)])
% % axis(ax(2),[eps max(fc.ext(end,1)) 0 20])
% % axis(ax(2),[0 10 0 1.5])
% set(get(ax(1),'XLabel'), 'String', 'Indentation (\mum)', 'FontSize', 14)
% set(get(ax(1),'YLabel'), 'String', 'Force (nN)', 'FontSize', 14)
% set(get(ax(2),'YLabel'), 'String', 'Apparent Youngs Modulus (kPa)',
'FontSize', 14)
% set(ax(1), 'YTickMode', 'auto', 'FontSize', 12, 'box','off')
% set(ax(2), 'YTickMode', 'auto', 'FontSize', 12)
% hold all
% E = E * 1e3;
% fc.ext(:,1) = fc.ext(:,1) * 1e-6;
% fc.ext(:,2) = fc.ext(:,2) * 1e-9;

% Optional: reconstruct the piecewise force curve and plot it and get sse
% ext_predicted = [];
% for i=1:nbins
%     first = get_index(fc.ext(:,1), min_ind+binning*(i-1));
%     last = get_index(fc.ext(:,1), min_ind+binning*i);
%     ext = fc.ext(first:last,:);
%     ext_pred = [ext(:,1) (E(i)/(1-nu^2)).*lams(first:last)'];
%     ext_pred(:,2) = ext_pred(:,2) - (mean(ext_pred(:,2))-mean(ext(:,2)));
%     ext_predicted = [ext_predicted; ext_pred];
%     sse(i) = sum(abs(ext_pred(:,2)-ext(:,2)))/length(ext(:,1));
% end
% fc2 = zero_contact(curve,contact);
% plot(fc2.ext(:,1)*1e6, fc2.ext(:,2)*1e9, 'LineWidth', 3, 'color', 'red')
% hold on
% plot(ext_predicted(:,1)*1e6, ext_predicted(:,2)*1e9, 'LineWidth', 3, 'color',
[0 .5 0]);
% set(gca, 'FontSize', 12)
% xlabel('Indentation [\mum]')
% ylabel('Force [nN]')

% Optional: plot the a's to see contact radius as a function of
% indentation depth
% plot(fc.ext(:,1)*1e6, as'*1e6, 'LineWidth', 4);
% xlabel('Indentation [\mum]', 'FontSize', 14);
% ylabel('Contact Radius [\mum]', 'FontSize', 14);
% set(gca, 'FontSize', 12)


end
```

dhaliwal_rau.m

```
% dhaliwal_rau.m
% Bryant L. Doss, Robert Ros
%
% Designed in MATLAB R2012a, also works in MATLAB R2014a.
% PREREQUISITE: Fie package by Atkinson, Shampine for solving
% Fredholm Integral Equations of the Second Kind in MATLAB, to obtain
% see the references
%
% Generates a force curve for a two-layer system (top layer defined by E1,
% nu1, height h; bottom layer defined by E2,nu2, height extends to -Inf).
% Relavent literature for the procedure:
% I.N. Sneddon, Int. J. Eng. Sci. 3 47-57 (1965)
% R.S. Dhaliwal and I.S. Rau, Int. J. Engng. Sci. 8, 854-856 (1970)
% B.B. Akhremitchev and G.C. Walker, Langmuir 15, 5630-5634 (1999)
% K.E. Atkinson and L.F. Shampine, ACM Trans. Math. Softw. 34, 21 (2008)
%
% The tip shape has several options -- 'parabolic' for standard Hertzian
% indenter, 'conical', 'hyperbolic', 'briscoe', and 'spherocone'. r is the
% tip apex radius and theta is the axisymmetric cone angle
%
% Input parameters -- SI units [Pa,m,radians]:
%  E1: the Young's modulus of the top layer
%  nu1: the Poisson's ratio of the top layer
%  E2: the Young's modulus of the bottom layer
%  nu2: the Poisson's ratio of the bottom layer
%  h: the height of the top layer
%  r: the radius of the indenter probe (does not matter for conical)
%  theta: the half-angle of the indenter probe, units are radians
%  type: the indenter probe geometry type, supported types:
%       parabolic: Hertz model
%       conical: Sneddon model
%       hyperbolic: a hyperbola
%       briscoe: Briscoe's blunted cone model
%       spherocone: sphrical tip, transitions to cone continuosly
%       cylindrical: a cylinder
%       sphere: a sphere
%  mesh: indentation points at which the forces will be calcualated
% Output parameters -- SI units [m,Pa]:
%  fc: force-indentation curve, fc.ext is a n-by-2 array [indentation,F]
%  as: contact radius, n-by-2 arrray [indentation,a]
%
% Example: Hertz model indentation, 1kPa+10um top layer, 10kPa bottom,
%          both are incompressible, bead radius is 2.5um, every 10nm to 1um
% f=dhaliwal_rau(1e3,0.5,1e4,0.5,10e-6,2.5e-6,1,'parabolic',0:10e-9:1e-6);
% plot(f.ext(:,1),f.ext(:,2);


function [fc, as] = dhaliwal_rau(E1,nu1,E2,nu2,h,r,theta,type,mesh)

% Sanity checks
if E1 < 0
    E1 = 1.0;
end
if E2 < 0
    E2 = 1.0;
end

% The function H converges very fast, set the maximum
max = 1e15;
```

```
if mesh(1) == 0
    mesh = mesh(2:end); % get rid of 0 meshpoint
end

% Define parameters and functions
mu = (E1./(2.*(1+nu1))) ./ (E2./(2.*(1+nu2)));
b = ((3-4.*nu1)-mu.*(3-4.*nu2)) ./ (1+mu.*(3-4.*nu2));
c = (1-mu) ./ (mu+3-4.*nu1);
H = @(x) -(b+c.*(1+x).^2+2.*b.*c.*exp(-x)) ./ ...
          (exp(x)+b+c.*(1+x.^2)+c.*b.*exp(-x));

as(1,:) = [0 0]; % array for 2-layer contact radii
a0s(1,:) = [0 0]; % array for homogeneous contact radii
curve(1,:) = [0 0]; % array for force-indentation curve

for i=1:length(mesh) % iterate over the mesh
    % Optional: display progress
%     disp(['Indentation step: ' num2str(mesh(i))])

    % Find the supported type, get beta and a0 (initial guess at contact)
    if strcmp(type, 'parabolic')
        f = @(x,a) (a.^2./(2.*r)).*x.^2;
        beta = @(t,a) a.^2.*t.^2./r;
        a0 = sqrt(r.*mesh(i));

    elseif strcmp(type, 'conical')
        f = @(x,a) x .* cot(theta);
        beta = @(t,a) (1/2) * pi * t * a * cot(theta);
        a0 = 2 * mesh(i) * tan(theta) / pi;

    elseif strcmp(type, 'hyperbolic')
        f = @(x,a) r.*cot(theta).^2.*(sqrt(a.*x./(r.*cot(theta).^2) + 1) - 1);
        beta = @(t,a) t.*a.*cot(theta).*atan(a.*t.*tan(theta)./r);
        a0 = sqrt(r.*mesh(i));
        afn = @(a) real(mesh(i) - (a.*cot(theta)./2) * (pi/2 +
atan(a./(2.*r.*cot(theta)) - r.*cot(theta)./(2.*a))));
        a0 = fzero(afn,a0);

    elseif strcmp(type, 'spherocone')
        b = r*cot(theta) / sqrt(1+cot(theta)^2);
        beta = @(t,a) (t <= b./a) .* (1/2).*a.*t.*log((r+a.*t)./(r-a.*t)) ...
            + (t > b./a) .* (a.*t.*log((r+a.*t)./(sqrt(r^2-
b^2)+sqrt(a.^2.*t.^2-b^2))) + a.*t.*acos(b./(a.*t))*cot(theta));

        % Use a0 of hyperbolic function
        a0 = sqrt(r.*mesh(i));
        afn = @(a) real(mesh(i) - (a.*cot(theta)./2) * (pi/2 +
atan(a./(2.*r.*cot(theta)) - r.*cot(theta)./(2.*a))));
        a0 = fzero(afn,a0);
        afn = @(a) real(mesh(i) - ((1 <= b/a) * (1/2)*a*log((r+a)/(r-a)) ...
            + (1 > b/a) * (a*log((r+a)/(sqrt(r^2-b^2)+sqrt(a^2-b^2))) +
a*acos(b/a)*cot(theta))));
        a0 = fzero(afn,a0);

    elseif strcmp(type, 'briscoe')
        b = r * cos(theta);
        m = 1/2;
        n = 1;
        beta = @(t,a) (t <= b./a) .* (a^2.*t.^2./r) ...
            + (t > b./a) .* (a.^2.*t.*(-sqrt(t.^2-b^2./a.^2)+t)./r +
a.*t.*acos(b./(a.*t))*cot(theta));
```

```
        a0 = sqrt(r.*mesh(i));
        afn = @(a) real((mesh(i) + (a/r)*((a^2-b^2)^(1/2)-a) - ...
                 (n*a/tan(theta))*((pi/2)-asin(b/a))));
        a0 = fzero(afn,a0);

    elseif strcmp(type, 'cylindrical')
        beta = @(t,a) a*t*0;
        a0 = r;

    elseif strcmp(type, 'parabocone')
        b = r * cot(theta);
        beta = @(t,a) (t <= b ./ a) .* (a^2.*t.^2./r) ...
            + (t > b./a) .* ((a.^2.*t.*(t - sqrt(t.^2 - (b.^2/a.^2))) ./ r) +
a.*t.*acos(b./(a.*t))*cot(theta));
        a0 = sqrt(r.*mesh(i));

    elseif strcmp(type, 'sphere')
        beta = @(t,a) (1/2).*a.*t.*log((r+a.*t)./(r-a.*t));
        a0 = sqrt(r.*mesh(i));

    % These are more experimental, basically this has some information
    % regarding sample geometry as well...
    elseif strcmp(type, 'sphere-sphere')
        q = 8e-6;
        beta = @(t,a) (1/2).*a.*t.*log((r+a.*t)./(r-a.*t)) +
(1/2).*a.*t.*log((q+a.*t)./(q-a.*t));
        a0 = sqrt(r.*mesh(i));
    elseif strcmp(type, 'spherocone-sphere')
        b = r*cot(theta) / sqrt(1+cot(theta)^2);
        q = 7e-6;
        beta = @(t,a) (t <= b./a) .* ((1/2).*a.*t.*log((r+a.*t)./(r-a.*t)) +
(1/2).*a.*t.*log((q+a.*t)./(q-a.*t))) ...
                    + (t  > b./a) .*
(a.*t.*log(((q+a.*t).*(r+a.*t))./((sqrt(r.^2-b.^2)+sqrt(a.^2.*t.^2-
b.^2)).*(sqrt(q.^2-b.^2)+sqrt(a.^2.*t.^2-b.^2)))) +
a.*t.*(acos(b./(a.*t)).*cot(theta)-(1/2).*log(q.^2-a.^2*t.^2)+log(sqrt(q.^2-
b.^2)+sqrt(a.^2.*t.^2-b.^2))));
        afn = @(a) real(mesh(i))-real(beta(1,a));
        a0 = fzero(afn,eps+sqrt(r.*mesh(i)));


    else
        disp('Type not supported')
        return
    end
    % End probe selection

    % Populate a0 array, scale a0 based on previous meshpoint
    % This is just handy for speeding up the computation quite a bit
    a0s(i+1,:) = [mesh(i) a0];
    if i > 2
        a0 = a0 * as(i,2)/a0s(i,2);
    end

    % Define some functions for the Fie call
    K = @(x,t,a) 2.*quadv(@(u)H(2.*u).*cos(a.*t.*u./h).*cos(a.*x.*u./h), 0,
max, 1e-9);
    lam = @(a) -h .* pi ./ a;
    rhs = @(t,a) lam(a) .* ((-E1 .* a) ./ (2 .* (1 - nu1^2))) .* (mesh(i) -
real(beta(t,a)));
```

```
    % Optional: add some adhesion, this is not really proven to be correct
%     G = 5e-4;
%     rhs = @(t,a) lam(a) .* ((-E1 .* a) ./ (2 .* (1 - nu1^2))) .* (mesh(i) -
real(beta(t,a)) + sqrt(2.*G.*pi.*a.*(1-nu1.^2)/E1));

    % Define some more functions for the Fie call
    phifn = @(a) Fie(lam(a), eps, 1, 1, @(x,t)K(x,t,a), @(x)rhs(x,a), 1e-13,
1e-10);
    getlast = @(t) t.x(end);

    if strcmp(type, 'cylindrical') % for cylindrical probe, a=a0 always
        a = a0;
    else
        % find the contact radius by finding root of the Fie call
        a = fzero(@(x) getlast(phifn(x)), a0, optimset('TolX', 1e-10));
    end

    % Now that a is known, solve for F
    phi = phifn(a); % use Fie with known a
    F = 4 * -trapz(phi.s, phi.x); % calculate F
    as(i+1,:) = [mesh(i) a]; % populate a
    curve(i+1,:) = [mesh(i) F]; % populate curve

end

fc.ext = curve; % return the force curve

end
```

rotation_minimum.m

```
% rotation_minimum.m
% Automatic contact point determination

% Basically introduce a virtual deflection then pick the "minimum point
% forcescale/lengthscale is the virtual deflection magnitude, this can be
% optimized somehow (for future work?)

% Input parameters -- SI units [Pa,m,radians]:
%  incurve: the force-curve structure
%  degree: amount of rotation
% Output parameters -- SI units [m,Pa]:
%  contact: the contact point

function contact = rotation_minimum (incurve, degree)
    if nargin < 2
        degree = 3;
    end

    forcescale = (incurve.ext(end,2) - incurve.ext(1,2)) / degree;
    lengthscale = incurve.ext(end,1) - incurve.ext(1,1);

    % Basically fabricate a virtual deflection for the enitre curve
    scale = forcescale / lengthscale;
    rotcurve = incurve;
    rotcurve.ext(:,2) = rotcurve.ext(:,2) - rotcurve.ext(:,1) * scale;

    % Find the minimum in the rotated curve, which is our contact
    % point
    [~, index] = min(rotcurve.ext(:,2));
    contact = rotcurve.ext(index,1);

    % Optional: plot
%     plot(incurve.ext(:,1),incurve.ext(:,2),
rotcurve.ext(:,1),rotcurve.ext(:,2));
%     hold on
%     plot(contact, incurve.ext(index,2), 'kx', 'LineWidth', 2);

end
```